ABSTRACT

Title of dissertation: Plasmonic and Ultrafast Optical Response of
2D and 3D Dirac Materials

Mohammad Mehdi Jadidi, Doctor of Philosophy, 2016

Dissertation directed by: Professor Thomas E. Murphy
Institute for Research in Electronics & Applied Physics

The fast-evolving field of condensed matter physics is witnessing a rapid development of a new class of materials, called Dirac materials. The low-energy electronic excitation in these materials behaves like massless Dirac particles. These materials exhibit unique optoelectronic properties, and understanding of Dirac quasi-particle dynamics in two and three dimensions is imperative to realizing the potential applications.

In this dissertation, we study two prominent Dirac materials that have unique optoelectronic properties: graphene (two-dimensional) and tantalum arsenide (three-dimensional). While the former can be regarded as the father of materials with a symmetry-protected Dirac spectrum, the latter is a more recent example of topology-protected Dirac materials, also known as 3D Weyl semimetals. We employ spectroscopy and ultrafast optical techniques to study plasmons, and the interaction/relaxation dynamics of photo-excited carriers in these materials.

More specifically, we study a new class of plasmon resonances in hybrid metal-graphene structures, which is an important step towards practical graphene plas-

monic optoelectronic devices. In addition, we investigate the giant nonlinear THz response of graphene plasmons using pump-probe techniques and discuss the physical origin of the plasmon-enhanced nonlinearity. Furthermore, we introduce a novel continuous-wave photomixing spectroscopy technique to investigate the frequency dependence and nonlinearity of hot-electron cooling in graphene. Finally, we explore the relaxation dynamics of photo-excited Weyl fermions in tantalum arsenide via ultrafast optical pump-probe techniques, which shed light on the electron-phonon relaxation processes in this material.

Plasmonic and Ultrafast Optical Response of
2D and 3D Dirac Materials

by

Mohammad Mehdi Jadidi

Dissertation submitted to the Faculty of the Graduate School of the
University of Maryland, College Park in partial fulfillment
of the requirements for the degree of
Doctor of Philosophy
2016

Advisory Committee:
Professor Thomas E. Murphy, Chair/Advisor
Professor Mohammad Hafezi
Professor Edo Waks
Professor Jeremy N. Munday
Professor H. Dennis Drew

Dedicated to my father, Manouchehr Jadidi, and my mother, Pouri

Kianpour.

Acknowledgments

In the course of my PhD studies at UMD, many people provided help and support to me, and I would like to acknowledge them here.

First, I would like to thank my adviser, Professor Thomas Murphy, for his infallible support and insightful guidance. Tom has always been flexible to discuss and consider new ideas and approaches. He offered me a great level of independence, which despite all difficulties, gave me the opportunity to acquire many new skills that I wouldn't have otherwise.

I am also thankful to Professor Dennis Drew for his help, support, and encouragement. He was always enthusiastic and supportive to discuss ideas and problems. I never left Dennis' office without extra motivation and several new physical insights. Dennis deepened my interest in physics research, particularly experimental condensed matter physics. This was his best gift, among many others that I will never forget.

It was certainly a privilege to discuss and collaborate with Professor Michael Fuhrer on different projects. During discussions with him, Michael's ideas and comments were incredibly efficient and helpful. I am grateful to Michael for this.

I would like to thank other members of my PhD committee, Professors Mohammad Hafezi, Edo Waks, and Jeremy Munday. I also benefited from having discussions with various people at UMD and elsewhere, including Dr. Kurt Gaskill, Professor Paola Barbara, Dr. Ashraf Ali, and Tejbir Phool, and I am thankful to all of them.

I had the opportunity of scientific interactions with many other bright people at UMD. I would like to thank Professor Dio Margetis for the enjoyable discussions on mathematics of graphene plasmonics I had with him, and his excellent MATH648M class. I am thankful to Dr. Mehdi Kargarian for stimulating discussions on topology and Weyl physics. I also thank Professor Mohammad Hafezi for discussions on topological photonics and nonlinear graphene plasmonics.

Many individuals assisted me in conducting my experiments during doctoral studies. I am indebted to Dr. Andrei Sushkov, for his helps in the lab and teaching me to carry out FTIR and cryogenic measurements. I am also thankful to Dr. Greg Jenkins for nice discussions and helping me locate tools in the lab anytime I needed. I would like to credit Dr. Kurt Gaskill and his team at NRL for providing epitaxial graphene samples. I acknowledge Dr. Martin Mittendorff for bridging us to the FEL facility in Dresden, and many thanks to Dr. Stephan Winnerl for his help with FEL measurements. I would like to thank all my other colleagues at UMD, especially Drs. Ryan Suess, Harold Cai, Gagan Kumar, JJ Wathen, Kyowon Kim, Shanshan Li, and Edward Leong.

At the end, I would like to thank my friends and family. There is no enough space here to mention names of all my friends, here in US and good old ones back in Iran, who helped ease the PhD life through many get-togethers, chats, laughs, etc. My brothers, Reza and Hoseein, and my sisters, Fatemeh and Zeinab, were always kind and supportive during these years. Thanks a million to my parents for their infinite care, support, and encouragement. And, finally, I don't know how to thank Soheila for love, and the peace of mind she gave me during my doctoral studies.

Table of Contents

Contributed Work

PATENTS

- **M.M. Jadidi**, A.B. Sushkov D.K. Gaskill, M.S. Fuhrer, H.D. Drew, T.E. Murphy, "Hybrid Metal-Graphene Plasmons for Tunable Terahertz Opto-electronics". US Patent Application Submitted, Number: PCT/US16/37393. Provisional Patent Application No. 62/175,695 (2016).

- D. Schmadel, A.B. Sushkov, **M.M. Jadidi**, T.E. Murphy, H.D. Drew, "Plasmonic Activated Graphene Terahertz Emitter and Mixer". Provisional Patent Application No.: 14/843,468 (2015).

JOURNAL PUBLICATIONS

- **M.M. Jadidi**, et al. "Ultrafast Optical Study of Carriers Dynamics in the Weyl Semimetal TaAs". in preparation.

- **M.M. Jadidi**, et al. "Giant Thermo-optical Nonlinearity of Graphene Plasmons". in preparation.

- **M.M. Jadidi**, R.J. Suess, C. Tan, X. Cai, K. Watanabe, T. Taniguchi, A.B. Sushkov, M. Mittendorff, J. Hone, M.S. Fuhrer, H.D. Drew, T.E. Murphy, "Tunable Ultrafast Thermal Relaxation in Graphene Measured by Continuous-Wave Photomixing". Physical Review Letters, accepted (2016). arXiv:1607.02181

- K.M. Daniels, **M.M. Jadidi**, A.B. Sushkov, A.K. Boyd, A. Nath, H.D. Drew, T. E. Murphy, R.L. Myers-Ward, D.K. Gaskill "Narrow Plasmon Resonances Enabled by Quasi-Freestanding Bilayer Epitaxial Graphene". under review (2016).

- **M.M. Jadidi**, J.C. König-Otto, S.Winnerl, A.B. Sushkov, H.D. Drew, T.E. Murphy and M. Mittendorff, "Nonlinear Terahertz Absorption of Graphene Plasmons". Nano Letters 16.4 (2016).

- **M.M. Jadidi**, A.B. Sushkov, R.L. Myers-Ward, A.K. Boyd, K.M. Daniels, D.K. Gaskill, H.D. Drew, T.E. Murphy, "Tunable Terahertz Hybrid Metal-Graphene Plasmons". Nano Letters 15.10 (2015).

- R.J. Suess, **M.M. Jadidi**, T.E. Murphy, and M. Mittendorff. "Carrier dynamics and transient photobleaching in thin layers of black phosphorus." Applied Physics Letters 107.8 (2015).

- X. Cai, A.B. Sushkov, **M.M. Jadidi**, L.O. Nyakiti, R.L. Myers-Ward, D.K. Gaskill,T.E. Murphy, M.S. Fuhrer, H.D. Drew, "Plasmon-enhanced Terahertz Photodetection in Graphene". Nano Letters 15.7 (2015).

- X. Cai, A.B. Sushkov, R.J. Suess, **M.M. Jadidi**, G.S. Jenkins, R.L. Myers-Ward, S. Li, J. Yan, D.K. Gaskill,T.E. Murphy, H.D. Drew, M.S. Fuhrer, "Sensitive Room-Temperature Terahertz Detection via the Photothermoelectric Effect in Graphene". Nature Nanotechnology 9.10 (2014).

- S. Li, **M.M. Jadidi**, T.E. Murphy, G. Kumar, "Plasmonic Terahertz Waveguide Based on Anisotropically Etched Silicon Substrate". IEEE Transactions on Terahertz Science and Technology 4.4 (2014).

- R.J. Suess, **M.M. Jadidi**, K. Kim, T.E. Murphy, G. Kumar, " Characterization of optical nonlinearities in nanoporous silicon waveguides via pump-probe heterodyning technique". Optics Express, 21.6 (2013).

- G. Kumar, S. Li, **M.M. Jadidi**, T.E. Murphy, "Terahertz Surface Plasmon Waveguide based on a One-Dimensional Array of Silicon Pillars". New Journal of Physics 15.8 (2013).

- S. Li, **M.M. Jadidi**, T.E. Murphy, G. Kumar, "Terahertz Surface Plasmon Polaritons on a Semiconductor Surface Structured with Periodic V-Grooves". Optics Express, 21.6 (2013).

- A. Vedadi, A. Ariaei, **M.M. Jadidi**, J.A. Salehi, "Theoretical Study of High Repetition Rate Short Pulse Generation with Fiber Optical Parametric Amplification", J. Lightwave Technol. 30.9 (2012).

Refereed Published Conference Proceedings

- **M.M. Jadidi**, A.B. Sushkov, R.L. Myers-Ward, A.K. Boyd, K.M. Daniels, D.K. Gaskill, H.D. Drew, T.E. Murphy, "Terahertz Plasmon Resonances in Graphene-Filled Subwavelength Metallic Apertures". CLEO: Fundamental Science, Optical Society of America (2016).

- M. Mittendorff, **M.M. Jadidi**, J.C. König-Otto, S.Winnerl, A.B. Sushkov, H.D. Drew, T.E. Murphy, "Nonlinear Plasmonic THz Absorption in Graphene Ribbons". CLEO: Fundamental Science, Optical Society of America (2016).

- R.J. Suess, **M.M. Jadidi**, T.E. Murphy, and M. Mittendorff, "Time Resolved Spectroscopy on Thin Layers of Black Phosphorus.". Frontiers in Optics FW3A-5, Optical Society of America (2015).

- **M.M. Jadidi**, R.J. Suess, X. Cai, A.B. Sushkov, M. Mittendorff, M.S. Fuhrer, H.D. Drew, T.E. Murphy, "Characterization of Graphene Photothermoelectric Detector via Two-wave Mixing Technique". CLEO: Fundamental Science, Optical Society of America (2015).

- R.J. Suess, X. Cai, **M.M. Jadidi**, A.B. Sushkov, G.S. Jenkins, L.O. Nyakiti, R.L. Myers-Ward, S. Li, J. Yan, D.K. Gaskill, T.E. Murphy, H.D. Drew, M.S.

Fuhrer, "Characterization of Fast Temporal Photoresponse in a Broadband Graphene Photodetector". CLEO: Fundamental Science, Optical Society of America (2014).

- G. Kumar, S. Li, **M.M. Jadidi**, T.E. Murphy, "Anisotropically Etched Silicon Surfaces for Planar Plasmonic Terahertz Guided Wave Devices" CLEO, Optical Society of America, (2014).

- **M.M. Jadidi**, G.Kumar, S.Li, T.E. Murphy, "Terahertz Plasmonic Waveguide Based on Periodically Structured Silicon Surface", CLEO: Science and Innovations. Optical Society of America (2013).

Chapter 1: Introduction

1.1 Graphene

Graphene, an allotrope of carbon with honeycomb lattice, is the first two-dimensional material, discovered in 2004 [1–3]. During the past decade, graphene has captured the attention of theoretical and experimental physicists alike who are interested in the remarkable electrical, optical and thermal properties of this unique atomically thin material [4, 5].

1.1.1 Graphene Plasmonics for Tunable Terahertz Optoelectronics

Among its many outstanding properties, graphene supports terahertz surface plasma waves – sub-wavelength charge density oscillations connected with electromagnetic fields that are tightly localized near the surface [6, 7]. When these waves are confined to finite-sized graphene, plasmon resonances emerge that are characterized by alternating charge accumulation at the opposing edges of the graphene. The resonant frequency of such a structure depends on both the size and the surface charge density, and can be electrically tuned throughout the terahertz range by applying a gate voltage [8, 9]. Graphene plasmonics has the potential to revolutionize

terahertz technology the last great underdeveloped frequency band of E&M waves. Tunable graphene plasmonic resonators have been suggested for use in terahertz filters, modulators, detectors, and emitters, and could find widespread applications in science, medicine, security, and communications [10–16].

1.1.2 Nonlinear Optical Response of Graphene

Graphene exhibits a broadband intrinsic nonlinear optical response [17, 18] that has been used in mode-locking [19] and harmonic generation [20]. In the optical and near-infrared regime, the nonlinear response of graphene is primarily attributed to transient Pauli blocking, which leads to an ultrafast saturable absorption and nonlinear refraction [21]. In the terahertz regime [22, 23], however, the nonlinear response is primarily caused by fast thermal heating and cooling of the electron population, which effects the intraband absorption [24–26].

1.1.3 Photothermoelectric Response and Hot-electron Cooling in Graphene

When graphene absorbs electromagnetic radiation, its electrons heat up and produce a measurable thermoelectric response, even at room temperature. Because of graphene's gapless dispersion relation, small electron heat capacity, and anomalously weak electron-phonon coupling, this photothermal detection mechanism is broadband (from DC to visible), highly sensitive, and fast [13, 27–30]. The speed, temperature-, and power-dependence of these detectors depend critically upon how fast and by what mechanisms the hot carriers relax [31–33]. Two

primary cooling mechanisms have been identified: supercollision cooling, in which disorder-assisted scattering allows for non-momentum-conserving transitions, and conventional momentum-conserving electron-phonon cooling [31, 32, 34–39].

1.2   3D Dirac and Weyl Semimetals

Various electronic systems exhibit properties that can be well described by the Dirac equation. In particular, three-dimensional (3D) Dirac semimetals have recently been discovered as the 3D analogue of graphene having linear energy dispersion around Fermi points [40, 41]. When either inversion or time reversal symmetry is broken in such systems, the Dirac states are decomposed into pairs of Weyl states in which the electronic states are chiral and singly degenerate [42–44]. Owing to the nontrivial topology of electronic wave functions, Weyl semimetals exhibit new physical properties related to the Berry curvature associated with the Weyl points, and novel quantum states such as Fermi arc surface states [42–47]. Since their discovery in 2015 [48–50], Weyl semimetals have attracted tremendous amount of attention as another rich direction to explore in topological condensed matter physics. While they have been verified through ARPES and other surface probe experiments, their other physical properties are just beginning to be examined.

1.3   Organization of Dissertation

We start chapter 2 with a brief introduction to graphene conductivity and its optical response. After, we discuss plasmon modes in graphene, and plasmon res-

onances of a simple structure of graphene ribbons. In particular, we present measurements of plasmon resonances in graphene ribbons and describe theory models to describe plasmonic response of such structures. Next, we study, through theory and experiments, a new type of plasmon resonance that occurs when a graphene channel is connected to conductive boundaries. This new plasmon mode resolves two outstanding problems that have to date hindered the development of graphene-based tunable plasmonic terahertz devices: (1) the incorporation of conducting metal contacts to a tunable graphene plasmonic channel, and (2) the matching of sub-wavelength graphene plasmonic resonators to free-space propagating waves, which previously limited absorption to a few percent. Furthermore, we present an equivalent circuit model for the fundamental mode of hybrid metal-graphene structure, and also discuss the higher order plasmon modes in such structures.

In chapter 3, first, we show nonlinear pump-probe measurement results on the plasmonic device of CVD graphene ribbons. In addition, we present a theory that explains the observed plasmon-enhanced nonlinear response of graphene ribbons. Second, we measure the nonlinear plasmonic response of quasi-free-standing bilayer graphene ribbons. Further, we discuss results of pump-probe measurements at frequencies around the plasmon resonance. Finally, we employ the presented theory to predict how the nonlinearity would be enhanced further using high mobility HBN-encapsulated graphene.

Chapter 4 starts by introducing a new photocurrent spectroscopy technique that uses mixing of two continuous-wave beams to study nonlinearity and frequency response of photovoltage. We describe the two graphene photo-thermo-electric de-

vices investigated by the proposed photomixing technique. Next, we discuss the measurements of carrier density dependence and difference-frequency dependence of the photomixing signal, and, we present a nonlinear photo-thermo-electric model to explain the observed data. At the end, we demonstrate how the difference frequency dependence of photomixing signal changes with temperature.

In Chapter 5, first, we present a brief introduction to optical conductivity of 3D Dirac semimetals. Second, we discuss the band structure and electronic properties of the 3D Weyl semimetal tantalum arsenide (TaAs). Third, we present our pump-probe measurement results on carriers dynamics and relaxation in TaAs. In addition, we provide a qualitative thermodynamic model to describe the observed pump-probe results. Based on the model, we extract the electron-phonon relaxation times in TaAs from pump-probe data. At the end of chapter, we show the result of temperature dependence pump-probe measurements.

Chapter 6 provides some potential future directions based on studies presented in the dissertation.

Chapter 2:   Plasmons in Hybrid Metal-Graphene Structures

2.1   Overview

When a conductor is illuminated with light, its electrons can oscillate in collective motion called a plasmon resonance. In metals, these plasmons occur at visible light frequencies, but in graphene the motion happens at much slower terahertz frequencies, and the resonant frequency can be tuned by applying a voltage [6–9].

The promise of tunable graphene THz plasmonics has yet to be fulfilled, however, because most proposed optoelectronic devices including detectors, filters, and modulators [11–16] desire near total modulation of the absorption or transmission, and require electrical contacts to the graphene – constraints that are difficult to meet using existing plasmonic structures. Until now, there was no experimental evidence that two-dimensional plasmons could be confined with conductive boundaries.

In this chapter, we demonstrate a new type of plasmon resonance in metal-contacted graphene, and we use analytic calculations, numerical simulations, and THz reflection and transmission measurements to confirm the principle of operation. These plasmon modes shows strong coupling to incident terahertz radiation, so that maximal absorption in graphene can be achieved at a resonance frequency that is gate-tunable. We also introduce an equivalent circuit model that predicts the res-

onant frequency, linewidth, and impedance matching condition of the fundamental plasmon mode, and can be used for designing graphene plasmonic metamaterials and antenna coupled devices. We present predicted results for high mobility graphene that show that a near 100% tunable resonant transmission can be achieved, giving an ideal platform for THz modulators and tunable bandpass filters [51].

2.2 Optical Conductivity of Graphene

The contribution of intraband scattering of free carriers in graphene to its optical conductivity is calculated as [52, 53]

$$\sigma_{intra}(\omega) = 2ie^2 k_b T \frac{\ln\left[2\cosh\left(|\mu_c|/2k_bT\right)\right]}{\pi\hbar^2(\omega + i\Gamma)} \tag{2.1}$$

where T is graphene electron temperature, μ_c is the chemical potential for graphene carriers (electrons or holes), and Γ is carriers scattering rate. k_b and $\hbar$ are Boltzmann and Planck constant respectively.

For most of studies in this thesis, graphene carriers are in the degenerate regime ($|\mu_c| \gg k_bT$), and thus $\sigma_{intra}(\omega)$ in (2.1) can be approximated by a Drude conductivity,

$$\sigma_{intra}(\omega) = \frac{ie^2|E_F|}{\pi\hbar^2(\omega + i\Gamma)} \tag{2.2}$$

where E_F is the Fermi level of carriers in graphene.

In the degenerate regime, and when $\hbar\omega \gg kT$, the interband conductivity can be approximated by [52–54]

$$\sigma_{inter}(\omega) = \frac{e^2}{4\hbar} \left[\mathrm{H}(\hbar\omega - 2\mu_c) - \frac{i}{\pi} \ln\left(\left| \frac{\hbar\omega + 2\mu_c}{\hbar\omega - 2\mu_c} \right| \right) \right] \tag{2.3}$$

where $\mathrm{H}(x)$ is the Heaviside step function. The frequency-dependent graphene conductivity $\sigma(\omega)$ is the summation of contributions from intraband (2.2) and interband (2.3) electronic transitions,

$$\sigma(\omega) = \sigma_{intra}(\omega) + \sigma_{inter}(\omega) \tag{2.4}$$

$$= \frac{ie^2 |E_F|}{\pi\hbar^2(\omega + i\Gamma)} + \frac{e^2}{4\hbar} \left[\mathrm{H}(\hbar\omega - 2\mu_c) - \frac{i}{\pi} \ln\left(\left| \frac{\hbar\omega + 2\mu_c}{\hbar\omega - 2\mu_c} \right| \right) \right] \tag{2.5}$$

Therefore, graphene conductivity can be specified by its carriers Fermi level and scattering rate, or equivalently by the carrier density $n \equiv E_F^2/(\pi\hbar^2 v_F^2)$ and mobility $\mu \equiv ev_F/\sqrt{\pi n}\Gamma\hbar$, where $v_F \approx 1.1 \times 10^6$ m/s is the Fermi velocity of electrons in graphene.

Fig. 2.1a plots the optical absorption of graphene A as a function of frequency f calculated from (2.5) for E_F=0.2 eV and $\Gamma/2\pi = 2.67$ THz. It is instructive to break the $A(f)$ plot into three different frequency regions: (i) Drude region: the intraband carriers scattering, illustrated as a green arrow in Fig. 2.1b, causes a strong Drude-like absorption of photons in DC and low THz frequencies, (ii) Pauli blocking region ($\Gamma/2\pi \ll f < E_F/\pi\hbar$): Drude absorption is negligible and also the interband transition is forbidden, due to the filled electronic states in the conduction band (red arrow in Fig. 2.1b), (iii) interband region ($f > E_F/\pi\hbar \approx$ 97 THz): incoming photons cause interband transition of graphene electrons from valence to the conduction band (blue arrow in Fig. 2.1b). This results in a frequency-

independent absorption of $A_{inter} \approx Z_0 e^2 / 4\hbar$ ($Z_0 \approx 377$ Ω: free-space impedance) which depends only on fundamental constants in physics and is $A_{inter} \approx 0.023$ [54].

We note that the conductivity in THz frequencies, that concerns most of the work in this thesis, are dominated by the intraband Drude contribution (2.2).
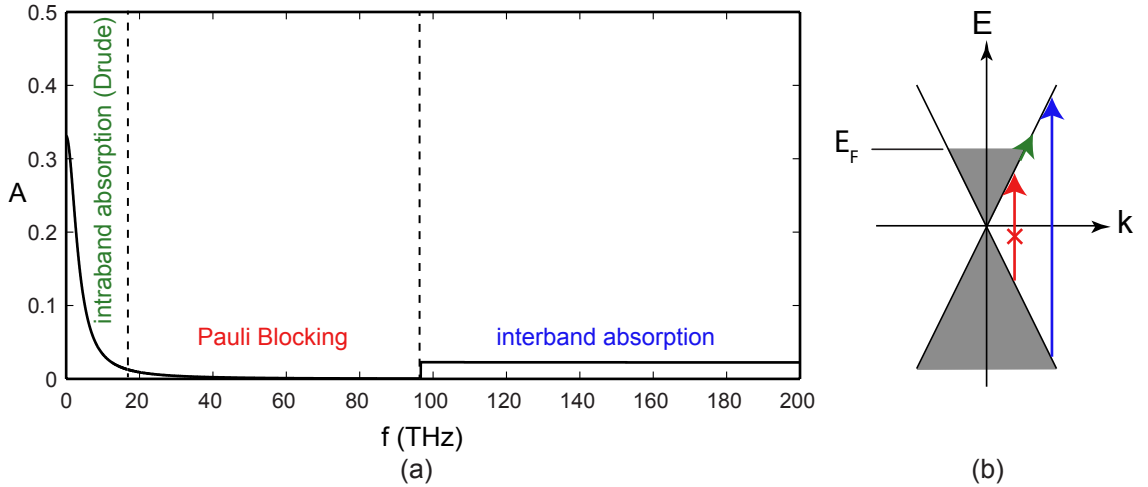
Figure 2.1: (a) Calculated graphene absorption at $T = 0$, as a function of frequency for E_F=0.2 eV and $\Gamma/2\pi = 2.67$ THz. The three different frequency regions (Drude, Pauli blocking, and interband) are separated by dashed lines. (b) Three electronic transitions concerning the three frequency regions shown in part a.

In Fig. 2.2, we plot graphene absorption as a function of frequency for different Fermi levels. As E_F increases, low-frequency Drude absorption increases, and the interband edge shifts to a higher frequency. An attractive feature of graphene as a two-dimensional conductor is the tunability of Fermi level via applying an out of plane electrostatic field. This scheme is illustrated in the inset of Fig. 2.2 where a gate voltage V_g is applied between graphene and a conductor separated by a gate dielectric to change the graphene carrier density. Therefore, graphene absorption

can be readily altered by a gate voltage, an advantageous effect for various opto-
electronics device applications from THz to visible frequency range.
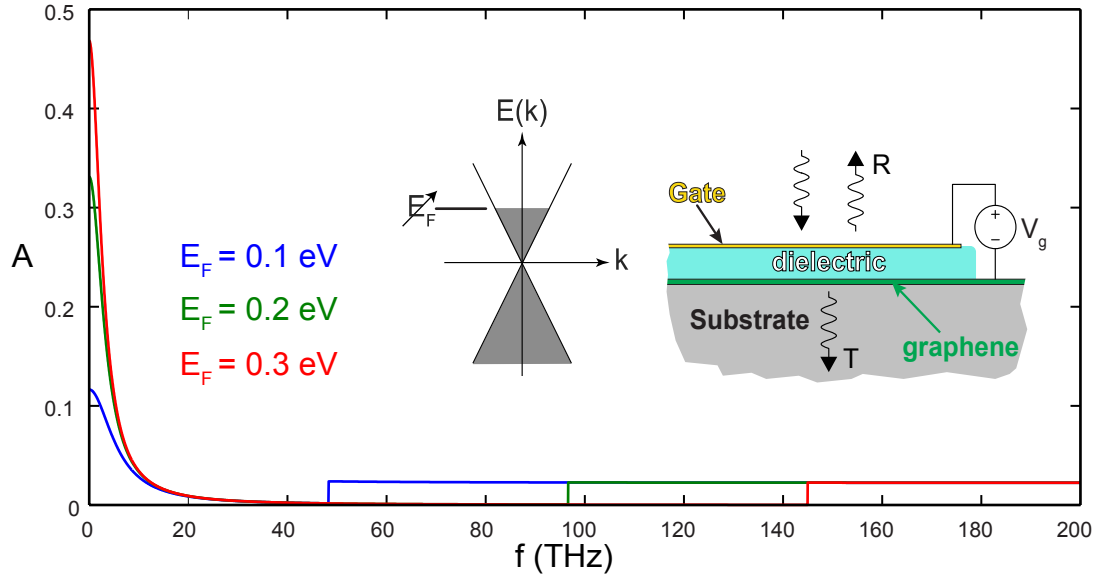
Figure 2.2: Graphene absorption vs frequency for different E_F. The inset illustrates
the electrostatic gate-tunability of the graphene Fermi level.

2.2.1 Optical Properties of a Thin Conductive film

In this section, we present a simple model to calculate optical properties of a
two-dimensional film using its conductivity. When a linearly polarized plane wave is
normally incident on a two-dimensional conductive sheet, the transmission, reflec-
tion, and absorption can be described using a simple transmission-line model shown
in Fig. 2.3.

In this model, the incident and substrate regions are modeled as transmission
lines with characteristic impedances of $Z_1 \equiv Z_0/\sqrt{\epsilon_1}$ and $Z_2 \equiv Z_0/\sqrt{\epsilon_2}$, respectively,
and the two-dimensional sheet is modeled with a frequency-dependent lumped con-
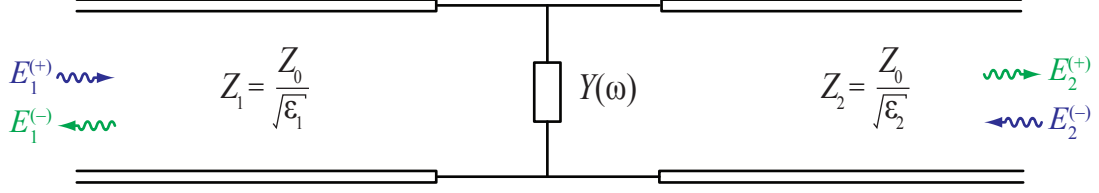
Figure 2.3: Transmission line model of reflection, transmission and absorption in a conductive sheet.

ductance $\sigma(\omega)$.

The relationship between the amplitudes of the incoming and outgoing wave amplitudes can be described by a scattering matrix,

$$
\begin{bmatrix} E_1^{(-)} \\ E_2^{(+)} \end{bmatrix} = \begin{bmatrix} S_{11} & S_{12} \\ S_{21} & S_{22} \end{bmatrix} \begin{bmatrix} E_1^{(+)} \\ E_2^{(-)} \end{bmatrix} \tag{2.6}
$$

For the circuit model shown in 2.3(a), the scattering matrix is calculated to be:

$$
\begin{bmatrix} S_{11} & S_{12} \\ S_{21} & S_{22} \end{bmatrix} = \frac{1}{Y_1 + Y_2 + Y(\omega)} \begin{bmatrix} Y_1 - Y_2 - Y(\omega) & 2Y_2 \\ 2Y_1 & Y_2 - Y_1 - Y(\omega) \end{bmatrix} \tag{2.7}
$$

where $Y_i = 1/Z_i$ and $Y(\omega)$ is the complex admittance (effective conductivity) of the thin film.

For waves incident from region 1, the reflection, transmission and absorption are calculated to be

$$
R(\omega) = |S_{11}|^2 = \left| \frac{Y_1 - Y_2 - Y(\omega)}{Y_1 + Y_2 + Y(\omega)} \right|^2 \tag{2.8}
$$

$$
T(\omega) = \frac{Y_2}{Y_1} |S_{21}|^2 = \frac{4Y_1 Y_2}{|Y_1 + Y_2 + Y(\omega)|^2} \tag{2.9}
$$

$$
A_G(\omega) = 1 - R(\omega) - T(\omega) = \frac{4Y_1 \operatorname{Re}\{Y(\omega)\}}{|Y_1 + Y_2 + Y(\omega)|^2} \tag{2.10}
$$

These relations describe the absorption, transmission, and reflection from a thin film with normally incident radiation.

To model the optical response of a plane graphene sheet, graphene can be described by a Drude conductivity

$$\frac{1}{\sigma(\omega)} = \frac{(1 - i\omega/\Gamma)}{\sigma_0} = R_G - i\omega L_G \tag{2.11}$$

where $\sigma_0 \equiv ne\mu$ represents the DC sheet conductivity of a graphene layer with carrier concentration n and mobility μ, and $\Gamma \equiv ev_F/\hbar\mu\sqrt{\pi n}$ is the scattering rate. From (2.11), the graphene may be modeled by its ohmic resistance, $R_G = \sigma_0^{-1}$, in series with its kinetic inductance, $L_G = (\sigma_0\Gamma)^{-1}$ [55].
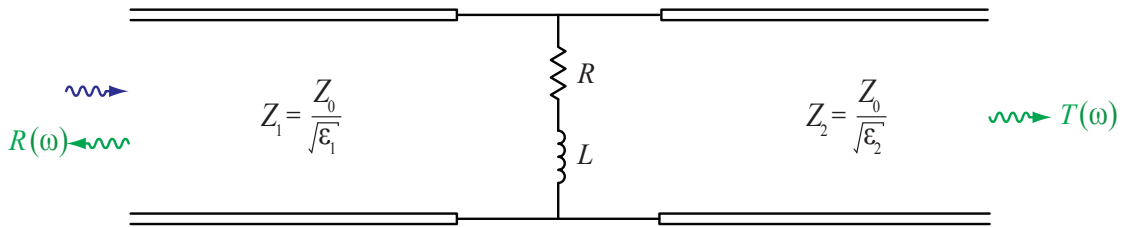
Figure 2.4: Equivalent circuit for Drude absorption by an unpatterned graphene sheet on a substrate.

This model correctly predicts the Drude absorption, reflection, and transmission in the terahertz regime. The transmission line model presented in this section can be generalized to multilayer and finite-thickness substrates by adding additional finite-length transmission line segments.

2.3 Plasmon Resonances in Graphene Ribbons

2.3.1 Overview

Graphene supports strongly confined surface plasmon waves in THz/mid-IR frequencies [6–8, 56]. The plasmon wavelength can be 2-3 orders of magnitude smaller than the free space wavelength, leading to a strong field localization at the plasmon resonance frequency [57]. When the graphene surface is patterned to sub-wavelength structures with dielectric boundaries, standing wave plasmon resonances emerge where electrons collectively oscillate within the subwavelegnth graphene elements [8,9]. In this section, we discuss properties of the fundamental (first) plasmon resonance in a single and array of graphene ribbon(s).

2.3.2 Dispersion of Graphene Plasmons

We assume that graphene is placed at the interface of two dielectrics with dieletric constants of ϵ_1 and ϵ_2. Considering a Drude model for graphene conductivity (2.2), the dispersion relation for plasmons in graphene $\omega_p(k)$ is calculated from [56]

$$\omega_p(\omega_p + i\Gamma) \approx \frac{e^2 E_F}{2\pi\hbar^2\epsilon_0\bar{\epsilon}}k \tag{2.12}$$

where $\bar{\epsilon} = (\epsilon_1 + \epsilon_2)/2$. To obtain (2.12), we assumed that $|k| \gg \omega\sqrt{\bar{\epsilon}}/c$ (non-retarded approximation), which is valid for graphene plasmons in a wide range of frequency [56, 58]. If we ignore the loss in graphene and only focus on the real

part of k ($\mathrm{Re}\, k \equiv q$) in (2.12) which determines the plasmon frequency, and use $E_F = \hbar V_F \sqrt{n\pi}$, we obtain the following

$$\omega_p^2 \approx \frac{e^2 v_F}{2\sqrt{\pi}\hbar\epsilon_0\bar{\epsilon}} \sqrt{n}q \tag{2.13}$$

This equation demonstrates two distinguished properties of plasmons in a two-dimensional conductor: (1) square-root dispersion relation, and (2) $n^{1/4}$ carrier density dependence of the plasmon frequency [8, 56].

2.3.3 Plasmon Resonance Frequency of Graphene Ribbons

Now we use (2.13) to find an approximate expression for frequency of the first plasmon resonance in a graphene ribbon with width w and lateral dielectric boundaries. To a zeroth approximation, one expects that the first plasmon resonance is a dipole mode of the graphene ribbon, and one can find the resonance frequency by placing $q = \pi/w$ in (2.13). However, this is a crude approximation that requires modifications, because the electric field at the graphene boundary is not necessarily zero and can extend into the dielectric boundaries. To account for this, we can still use the dipole approximation, but phase term ϕ needs to be added to the reflected plasmon wave from dielectric boundary, which reulsts in an effective wave vector of $q = (\pi - \phi)/w$ [59, 60]. For an isolated graphene ribbon, we find empirically that $\phi \approx \pi/4$ [59, 61], and from (2.13), one finds the plasmon frequency ω_{ribbon} of

$$\omega_{ribbon}^2 = \frac{3\sqrt{\pi}}{8} \frac{e^2 v_F}{\hbar\epsilon_0\bar{\epsilon}} \frac{\sqrt{n}}{w} \tag{2.14}$$

For an array of graphene ribbons, the electric field extends even further beyond

14

the ribbon due to the dipolar coupling of adjacent ribbons [59, 62]. This results in a reflection phase of $\phi > \pi/4$, and thus a red-shifted plasmon resonance compared to an isolated ribbon. In [60], authors calculate ϕ as a function of ribbon width and array period, which can be placed in the following to calculate the resonance frequency

$$\omega_{ribbons-array}^2 = \frac{\pi - \phi}{2\sqrt{\pi}} \frac{e^2 v_F}{\hbar \epsilon_0 \bar{\epsilon}} \frac{\sqrt{n}}{w} \tag{2.15}$$

2.3.4 Drude Lorentz Model

In this section, we present an equivalent circuit model to approximate the optical properties of the first plasmon mode in an array of graphene ribbons.

When a conductor is patterned into an array of ribbons with period Λ and width w, it forms a capacitive grid that can be modeled by a sheet capacitance of [63]

$$C = 2\epsilon_0 \bar{\epsilon} \Lambda \ln[\sec(\pi w/2\Lambda)]/\pi \tag{2.16}$$

where $\bar{\epsilon} \equiv (\epsilon_1 + \epsilon_2)/2$ is the average dielectric constant. Accounting for the sheet resistance and kinetic inductance of the graphene that comprises the ribbons, the equivalent sheet impedance may be modeled by a resistor, capacitor and inductor in series, as shown in Fig. 2.5 [64]:

$$Z(\omega) = R_G \frac{\Lambda}{w} + i\omega L_G \frac{\Lambda}{w} - \frac{i}{\omega C} \tag{2.17}$$

where R_G and L_G are the graphene sheet resistance and kinetic inductance,

15

and the additional factor of Λ/w accounts for the filling fraction of the graphene.

Defining the Drude weight as $D \equiv \pi\Gamma\sigma_0$, and using the expressions for R_G, L_G and C in (2.11) and (2.16), one finds an equivalent conductivity of

$$\sigma(\omega) = \frac{1}{Z(\omega)} = \frac{w}{\Lambda}\frac{D}{\pi[\Gamma - i(\omega^2 - \omega_r^2)/\omega]} \tag{2.18}$$

where the resonant (or plasmon) frequency is given by

$$\omega_r^2 \equiv \frac{Dw}{2\Lambda^2\epsilon_0\bar{\epsilon}\ln[\sec(\pi w/2\Lambda)]} \tag{2.19}$$

This equation automatically accounts for the dipolar coupling of plasmon fields in the adjacent graphene ribbons and provides an approximated value for plasmon resonance frequency in an array of graphene ribbons as in 2.15 ($\omega_r \approx \omega_{ribbons-array}$).
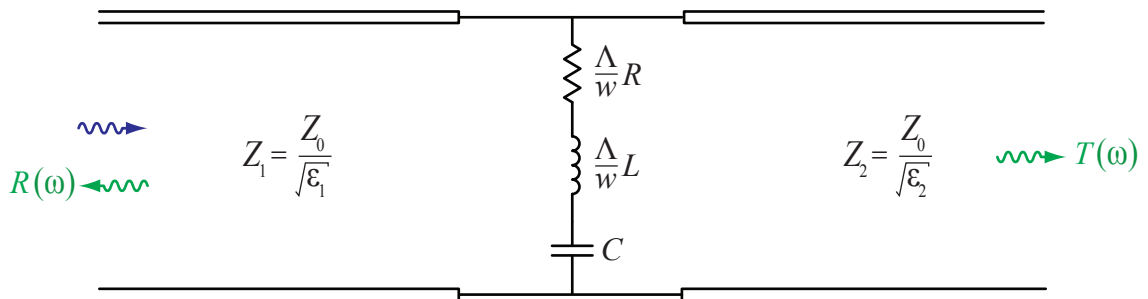
Figure 2.5: Equivalent circuit of graphene ribbon array.

The conductivity given in (2.18) is of the same form as that obtained from the Drude-Lorentz model of conductivity for bound electrons, assuming a resonant oscillation frequency of ω_p. When incorporated into (2.8)-(2.10), this model accurately approximates the transmission, reflection, and absorption spectrum of the graphene ribbons.

2.3.5 Experimental Results

In this section, we present experimental studies of the fundamental plasmon mode in graphene ribbons array. The graphene samples used here are quasi-free-standing bilayer graphene (QFS-BLG) on a SiC substrate. These samples are intrinsically hole-doped with carrier density $n = 1 \times 10^{13}$ cm^{-2} and mobility $\mu = (3900 \pm 200)$ cm^{2}V^{-1}s^{-1}. Three graphene ribbons samples with widths w=0.75, 1.5, 7 μm and periods Λ=1.5, 3, 16 μm were patterned using electron-beam lithography with a PMMA resist and oxygen plasma etch to remove the graphene from the exposed areas. Each of graphene gratings covered a region of 2×2 mm. Fig. 2.6a is a false-colored SEM image of the second sample with width and period of 1.5 μm and 3 μm respectively.

Far IR measurements were performed using a Bomem DA-8 FTIR spectrometer with a mercury lamp as a source and a 4 K silicon composite bolometer as a detector. Sample and reference SiC substrate were glued to identical copper circular apertures. THz beam illuminates the backside of the sample through a 1.5 mm diameter aperture. A rotating polarizer in front of the sample is used for transmission measurements with the electric field of light parallel and perpendicular to graphene strips which yield the plasmonic and Drude responses. We measured the ratio of transmissions for sample and bare SiC substrate glued on top of identical holes in copper sample holder because this gives the best photometric accuracy of the bolometer. The aforementioned transmission ratios were corrected by the transmission ratio of the empty holes. The transmission is defined as the transmission

17

spectra of the graphene on SiC divided by the transmission spectra of bare SiC, giving the transmission of graphene. Fig. 2.6b depicts the measurement scheme described here.

Fig. 2.6c illustrates the calculated charge density profile at the plasmon frequency of graphene ribbons. Charges in graphene ribbons collectively oscillate back and forth within the dielectric boundaries, leading to the accumulation of opposite charges on either sides.

Fig. 2.6d plots the measured normalized transmission spectra for three ribbons samples considered here. Minima (about 30% decrease) in the transmission spectra observed at plasmon frequencies due to increased on-resonance absorption of excited plasmons in graphene ribbons. As ribbons width decrease, the plasmon resonance frequency shifts to a higher frequency with a square-root dependence as expected from (2.15). Fig. 2.6d also presents the transmission spectrum through an unpatterned graphene sheet where Drude absorption causes strong decrease in transmission at low frequencies. Green curves in Fig. 2.6d represents Drude Lorentz fits (plus accounting for the etalon effect in the SiC substrate) to the experimentally measured spectra.

As discussed earlier in this chapter, an interesting feature of graphene is the gate-tunability of the carrier density. This enables a tunable resonance effect in a plasmonic device like graphene ribbons , as plasmon frequency and strength depends on carrier density (2.10 and 2.15). To experimentally demonstrate this, we spin-coat a thin layer of PEO/LiClO$_4$ as an electrolyte top gate and apply a DC gate voltage V_g to the first graphene ribbons device that had an un-gated plasmon frequency of
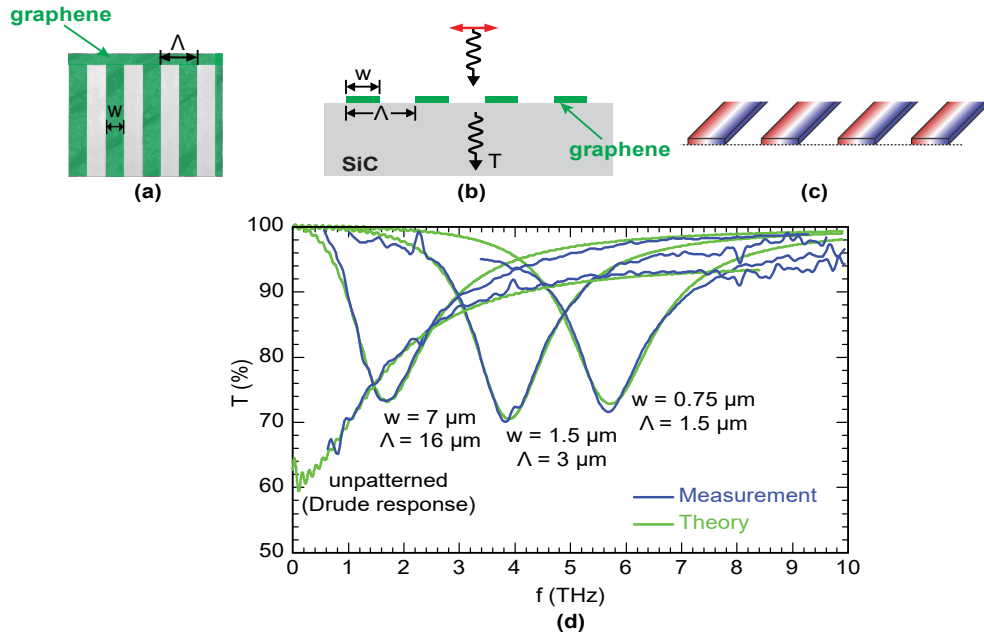
Figure 2.6: (a) False-colored SEM image of graphene ribbons with width w and period Λ on a SiC substrate. (b) Schematic of FTIR transmission (T) and reflection (R) measurements. (c) Calculated charge density profile at the plasmon frequency of graphene ribbons (d) Measured transmission spectrum through an un-patterned graphene sheet, and three different arrays of graphene ribbons. Green curves are fits from the Drude-Lorentz model. The minima (1.7 THz, 3.9 THz, 5.7 THz) in transmission spectra occur because of plasmon resonances of graphene ribbons arrays.

5.7 THz. Fig. 2.7 presents the measured transmission spectrum at different gate voltages/carrier densities. Increasing the gate voltage V_g toward positive values decreases the carrier density and red-shifts/weakens the plasmon resonance, as a result of reduction in Drude weight (2.15).
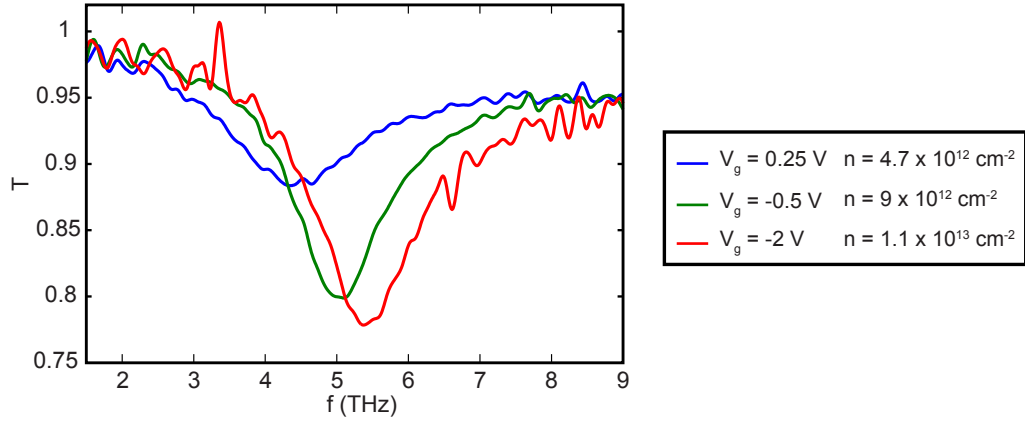
Figure 2.7: Measured transmission spectra for different graphene carrier densities tuned by applying a gate voltage V_g.

2.4 Plasmon Modes in Metal/Graphene Grating

2.4.1 Integral Equation

Maxwell's equations are solved for the general case of plasmon modes in a graphene-metal array with period Λ under normal-incidence plane-wave excitation as shown in Figure 2.8.

To calculate the plasmon resonances and absorption in these structures, we adapt the method of [65] to obtain an integral equation for the in-plane electric field when the structure is illuminated by a normally incident plane wave at frequency ω
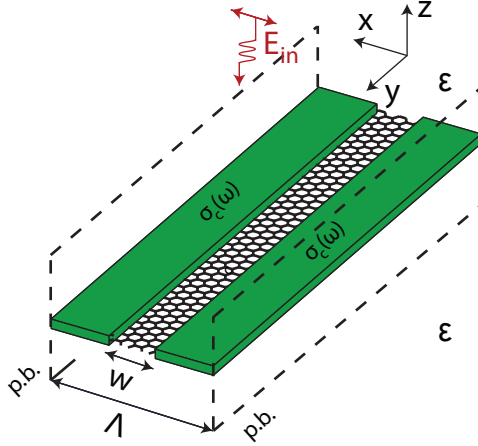
Figure 2.8: A unit cell of a periodic array (in x direction) of graphene-contact. Λ is the array period and w is the graphene channel width. ϵ is the dielectric constant of the surrounding material. $\sigma_c(\omega)$ is the contact conductivity. (p.b.: periodic boundary)

that is linearly polarized in the direction perpendicular to the graphene channels,

$$E(x) = \frac{\beta_c}{\beta\left(1 + \frac{\beta_c}{2}\right)} E_{\text{in}} + \frac{\beta - \beta_c}{\beta\Lambda} \sum_{l=-\infty}^{\infty} \frac{e^{i2\pi lx/\Lambda}}{1 + i\frac{\kappa_l\beta_c}{2}} \int_{-w/2}^{w/2} E(x')e^{-i2\pi lx'/\Lambda}dx' \qquad (2.20)$$

where E_{in} denotes the complex amplitude of the normally-incident, x-polarized incident plane wave with free-space wavelength λ, and $\kappa_l^2 = [(l\lambda/\Lambda)^2 - 1]$. β and β_c represent the frequency-dependent (Drude) conductivity of the 2D material and contact, respectively, normalized to the free-space impedance,

$$\beta = \sigma(\omega)\frac{Z_0}{\sqrt{\epsilon}} \qquad , \qquad \beta_c = \sigma_c(\omega)\frac{Z_0}{\sqrt{\epsilon}}$$

where Z_0 ($= 377\ \Omega$) is the wave impedance in vacuum. The contact conductivity σ_c is either zero, to model isolated graphene ribbons without contacts, or infinity to model a perfect electrical conducting boundary, or more generally it can describe

21

the Drude response of an arbitrary conductive contact. The sheet conductivity of the metal was estimated from the bulk Drude conductivity, multiplied by the metal film thickness.

By Fourier-expanding the electric field in the graphene channel from $-w/2$ to $+w/2$,

$$E(x) = \sum_{n=0}^{\infty} E_n \cos(2\pi nx/w) \tag{2.21}$$

the integral equation (2.20) can be re-cast as a matrix equation,

$$\left[\frac{1 + \delta_{0m}}{2} \delta_{mn} + \frac{(\beta_c - \beta)}{4\beta} \frac{w}{\Lambda} \sum_{l=-\infty}^{\infty} \frac{R_{mn}^{(l)}}{1 + i \frac{\kappa_l \beta_c}{2}} \right] E_n = \delta_{m0} \frac{\beta_c}{\beta(1 + \beta_c/2)} E_{\text{in}} \tag{2.22}$$

where

$$R_{mn}^{(l)} \equiv [\text{sinc}(n\pi + l\pi w/\Lambda) + \text{sinc}(n\pi - l\pi w/\Lambda)]$$

$$\times [\text{sinc}(m\pi + l\pi w/\Lambda) + \text{sinc}(m\pi - l\pi w/\Lambda)] \tag{2.23}$$

The Fourier components of the electric field can be obtained by numerically solving (2.22). In practice, for smoothly-varying plasmon modes, only the lowest few Fourier components are needed to accurately approximate the field.

Then, from $E(x)$, the fractional absorbed power in the 2D material is computed as

$$A_G(\omega) = \frac{Z_0/\sqrt{\epsilon_0}}{2\Lambda |E_{\text{in}}|^2} \int_{-w/2}^{w/2} \text{Re}\left\{ J^*(x)E(x)dx \right\} = \frac{\text{Re}\{\beta\}}{2\Lambda} \frac{1}{|E_{\text{in}}|^2} \int_{-w/2}^{w/2} |E(x)|^2 dx \tag{2.24}$$

Figure 2.9a shows the structure of the metal-contacted graphene plasmonic device considered here, which is comprised of a periodic array of narrow slots in a metallic layer that is patterned on top of a continuous graphene layer. For comparison, in Figure 2.9b we also consider an array of isolated graphene ribbons of

22

comparable dimension. In both cases, the period Λ is taken to be small compared to the free-space wavelength. The resonant modes and fractional absorption in the graphene $A(\omega)$ is then found by integrating the Joule power density over the graphene ribbon, and normalizing to the incident power of the plane wave. The calculated absorption spectrum reveals all of the dipole-active plasmon resonances and the relative coupling of these modes to radiation. In this thesis we focus on the fundamental low frequency plasmon mode. Higher order modes resonate at higher frequencies and can also be optimally coupled to the THz radiation.

In Figure 2.9c we present the theoretically computed absorption spectrum $A(\omega)$ for several different metal periods Λ, with the graphene ribbon width $w = 350$ nm held constant. The mobility and carrier density (electron or hole) were taken to be $\mu = 1000$ cm^{2}V^{-1}s^{-1} and $n = 1.5 \times 10^{13}$ cm^{-2}, respectively. The array shows no discernable plasmon resonance when the period Λ and graphene width w are comparable, giving instead a Drude-like response. However, when the metal contacts are made much wider than the graphene channel, a strong resonance emerges, characterized by high absorption in the graphene ribbon, at a resonant frequency that scales with $n^{1/4}w^{-1/2}$, similar to the plasmon resonances in uncontacted graphene ribbons [8, 62]. The surrounding material is assumed to be a uniform dielectric, in which case, the maximum achievable absorption in a two-dimensional layer is 50% [66] (also section 2.4.3.2). As shown in Figure 2.1c, at the resonant frequency, the graphene absorption reaches a peak of the maximum possible value (50%), even when the geometrical fill factor is only $w/\Lambda = 1/20$ (5%). This suggests an extremely high confinement of the THz field in the narrow slots where graphene is

23
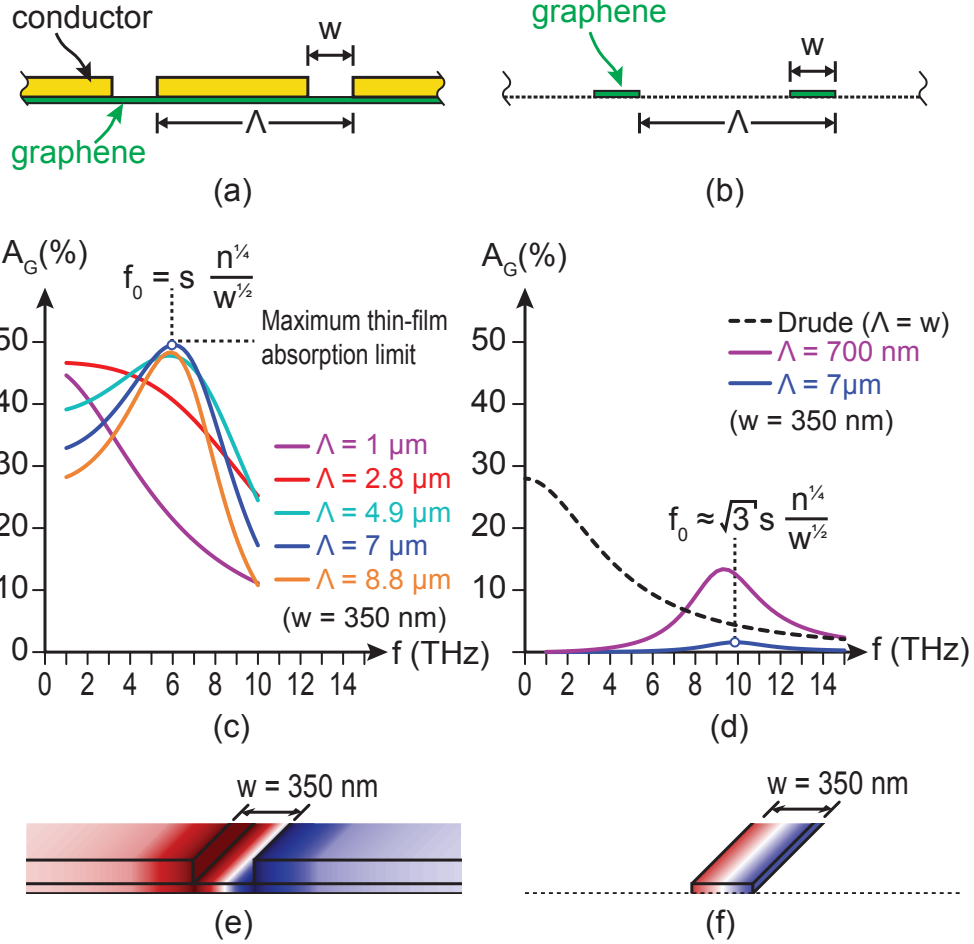
Figure 2.9: (a) Geometry of hybrid metal-graphene structure considered here. (b) Comparable array of isolated graphene ribbons. (c) Calculated graphene absorption spectrum $A_G(\omega)$ for the hybrid metal-graphene device with periods of $\Lambda = 1$, 2.8, 4.9, 7 and 8.8 μm, for a graphene channel with $w = 350$ nm, $n = 1.5 \times 10^{13}$ cm^{-2}, and $\mu = 1000$ cm^{2}V^{-1}s^{-1}. The upper and lower dielectric regions were assumed to be identical, with $\epsilon_1 = \epsilon_2 = 5$, in which case the theoretical maximum thin-film absorption is 50% [66], indicated by the horizontal dashed line. (d) Calculated absorption spectrum for isolated graphene ribbons with material properties identical to the channels considered in (c), and periods of $\Lambda = 0.7$ and 7 μm. For comparison, the dashed line indicates the Drude absorption spectrum for a continuous graphene sheet. (e)/(f) Calculated charge density profile at the plasmon resonant frequency for the hybrid metal-graphene device and graphene ribbon, respectively.

located. We note that by using known techniques such as an anti-reflection coating or a Salisbury screen [67] on top of the grating, the thin film limit absorption can be increased to nearly 100%, and a perfect tunable graphene plasmonic absorber can be achieved. The calculations confirm that these resonances disappear when the graphene is absent, when the polarization is rotated parallel to the channels, or when the graphene is electrostatically gated to the charge neutral point. For comparison, in Figure 2.9d, we show the absorption spectrum for an array of electrically isolated graphene ribbons of identical width, carrier density, and mobility, which yields a far lower on-resonant absorption (blue curve), even when the fill-factor is increased to 50% (purple curve).

The nature of the fundamental metal-graphene plasmon resonance is illustrated in Fig. 2.9e, which shows the charge density calculated at the resonant frequency. For comparison, we also show in Figure 2.9f the plasmon resonance for an uncontacted graphene ribbon of the same dimension. In the contacted graphene, the metal regions act as capacitive reservoir for charge accumulation, and the graphene serves as an inductive channel, thus forming a resonant circuit that interacts strongly with the incident radiation. This is in striking contrast to the isolated ribbon case, where the coupling to incident radiation is weaker, and does not depend sensitively on the grating period [8,9,62]. The extension of the spatial mode is accompanied by a significant reduction in the plasmon frequency (by a factor of $\approx \sqrt{3}$ in comparison to that of an isolated graphene ribbon [65]). The factor $\sqrt{3}$ is an approximate ratio that is consistent the postulate that a plasma wave incurs an approximate phase shift of approximately $\pi/4$ upon reflection from an open boundary [59,60], and $3\pi/4$

upon reflection from a conductive boundary.

2.4.2 Equivalent Circuit Model

The optical properties of the metal-graphene plasmonic grating in the sub-wavelength limit ($\Lambda < \lambda$) can be modeled by an equivalent two-port circuit at the junction of two semi-infinite transmission lines with impedances $Z_0/\sqrt{\epsilon_1}$ and $Z_0/\sqrt{\epsilon_2}$, that represent the upper and lower regions respectively, as shown in Figure 2.10 ($Z_0 = 377\ \Omega$, free space impedance). From (2.11), the graphene may be modeled by its ohmic resistance, $R_G = \sigma_0^{-1}$, in series with its kinetic inductance, $L_G = (\sigma_0 \Gamma)^{-1}$ [55]. R_G and L_G must each be multiplied by a geometrical factor of w/Λ to account for the filling factor in this periodic structure. The conducting contacts act as a capacitive grid [63, 68] that can be described by a capacitance $C_M = 2\epsilon_0 \bar{\epsilon} \Lambda \ln(\csc(\pi w/2\Lambda))/\pi$, where $\bar{\epsilon} = (\epsilon_1 + \epsilon_2)/2$ is the average dielectric permittivity. The finite size graphene channels contribute to an additional parallel capacitance [64], to give a total capacitance of $C = C_M + C_G = 2\epsilon_0 \bar{\epsilon} \Lambda \ln(2 \csc(\pi w/\Lambda))/\pi$.

Therefore, the resistance, inductance and capacitances appearing in this model are defined as:

$$R_G = \sigma_0^{-1} \tag{2.25}$$

$$L_G = (\sigma_0 \Gamma)^{-1} \tag{2.26}$$

$$C_G = 2\epsilon_0 \bar{\epsilon} \Lambda \ln[\sec(\pi w/2\Lambda)]/\pi \tag{2.27}$$

$$C_M = 2\epsilon_0 \bar{\epsilon} \Lambda \ln[\csc(\pi w/2\Lambda)]/\pi \tag{2.28}$$

and the incident and substrate regions are modeled as transmission lines with char-

acteristic impedances of $Z_1 \equiv Z_0/\sqrt{\epsilon_1}$ and $Z_2 \equiv Z_0/\sqrt{\epsilon_2}$, respectively.

The graphene and contact capacitances can be combined into a single equivalent capacitance of

$$C = C_G + C_M = 2\epsilon_0\bar{\epsilon}\Lambda \ln(2\csc(\pi w/\Lambda))/\pi \tag{2.29}$$
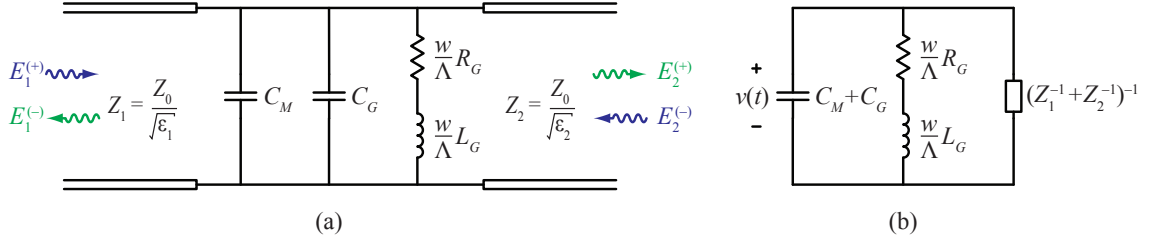
Figure 2.10: (a)Two-port equivalent circuit used to model for the hybrid metal-graphene grating. R_G and L_G are the graphene ohmic resistance and kinetic inductance respectively. C_G is the graphene ribbon array capacitance, and C_M is the capacitance of the metallic grid. The transmission $(T = \sqrt{\epsilon_2/\epsilon_1}|E_t/E_i|^2)$, reflection$(R = |E_r/E_i|^2)$, and graphene absorption $(1-R-T)$ can be approximately found from this circuit. $Z_1 \equiv Z_0/\sqrt{\epsilon_1}$ and $Z_2 \equiv Z_0/\sqrt{\epsilon_2}$ are wave impedances in the upper and lower semi-infinite regions with dielectric constants of ϵ_1 and ϵ_1, respectively. (b) Simplified circuit model when there are no input waves to the system, which is used to determine resonant (plasmon) frequency and damping rate.

2.4.2.1 Resonant Frequency and Linewidth

If there are no input waves applied to the system, the two transmission lines representing regions 1 and 2 may be simply replaced by their equivalent parallel impedance, which results in the simple second-order circuit shown in Figure 2.10(b).

In this circuit model, the power dissipated in Z_1 and Z_2 represents the radiative loss into regions 1 and 2 respectively, while the power consumed in R_G gives the absorption in the two-dimensional material. Applying Kirchoff's laws, the voltage $v(t)$ is found to satisfy the following second-order homogeneous differential equation:

$$\ddot{v}(t) + \left[\frac{R_G}{L_G} + \frac{(Y_1 + Y_2)}{C}\right]\dot{v}(t) + \left[\frac{\Lambda/w}{L_G C} + \frac{R_G(Y_1 + Y_2)}{L_G C}\right]v(t) = 0 \qquad (2.30)$$

which describes a damped harmonic oscillator. In the limit of low-damping, the resonant frequency (or plasmon frequency) is

$$\omega_0 = \sqrt{\frac{\Lambda/w}{L_G C}} \qquad (2.31)$$

$$= e\sqrt{v_F\sqrt{\pi}/2\hbar}\sqrt{\frac{\sqrt{n}}{w\epsilon_0\bar{\epsilon}\ln[2\csc(\pi w/\Lambda)]}} \qquad (2.32)$$

As noted earlier, the resonant frequency scales in proportion to $n^{1/4}w^{-1/2}$, as for the case of uncontacted graphene ribbons considered in [8], indicating that ω_0 can be tuned through the application of a gate voltage or by adjusting the graphene width. The resonant frequency blue-shifts weakly with increasing the duty cycle w/Λ, but in all of the cases considered here the resonance frequency is lower than that of an uncontacted graphene ribbon of the same width. (2.2) predicts that increasing the period Λ for a fixed width w, will result in a slight red-shift of the plasmon frequency, which is in direct contrast to the case of uncontacted graphene ribbons, where the plasmon frequency is blue-shifted by increasing the period, as a result of reduced dipolar plasmon mode coupling in adjacent ribbons [62].

The damping rate describes the linewidth of the plasmon resonance, which is

found to be:

$$\Delta\omega = \frac{R_G}{L_G} + \frac{(Y_1 + Y_2)}{C} \tag{2.33}$$

$$= \Gamma + \frac{\pi}{2\epsilon_0\bar{\epsilon}\Lambda\ln[2\csc(\pi w/\Lambda)]}\left(Z_1^{-1} + Z_2^{-1}\right) \tag{2.34}$$

The first term in (2.34) is the conventional Drude linewidth, which is constrained by the mobility and carrier density, while the second term describes the radiative linewidth of the plasmon, which does not depend on the graphene quality or material properties. This second term, which is negligible for uncontacted graphene ribbons, fundamentally limits the quality factor ($Q = \omega_0/\Delta\omega$). This predicts that the quality factor of the plasmon resonance improves upon increasing Λ. For the parameters considered in Fig. 2.9a, this predicts that for $\Lambda > 11.5w$, a plasmon resonance with $Q > 1$ can be achieved.

2.4.2.2 Absorbed Power and Impedance Matching

In many applications, one wishes to optimize the power that is absorbed in the graphene layer, by appropriately designing or selecting the properties and dimensions of the grating and film. The equivalent circuit model can also be used to predict the condition under which maximum power is delivered to the graphene layer. The maximum on-resonant graphene absorption is achieved when the material scattering rate Γ and radiative decay rates are equal, which also corresponds to the impedance matching between two dissimilar media [69, 70]. By maximizing the absorption (2.10) with respect to the complex admittance $Y(\omega)$, one readily finds

the optimal load admittance is

$$Y_{\mathrm{opt}} = (Y_1 + Y_2)^*$$
(2.35)

Since Y_1 and Y_2 are real numbers, (2.35) implies that $Y(\omega)$ must be real, which occurs at an optimal frequency that is close to the resonant frequency,

$$\omega_{\mathrm{opt}} = \sqrt{\frac{\Lambda/w}{L_G C} - \left(\frac{R_G}{L_G}\right)^2}$$
(2.36)

$$Y(\omega_{\mathrm{opt}}) = \frac{R_G}{L_G C}$$
(2.37)

In this case, the condition for maximum power transfer to the graphene layer can be expressed as

$$\frac{R_G}{L_G} = \Gamma = (Y_1 + Y_2)/C$$
(2.38)

which means that for maximum on-resonant absorption, the intrinsic material damping Γ is equal to the radiation damping.

Under these matched conditions, the lumped circuit may be regarded as impedance matching between two dissimilar media. The maximum fractional absorbed power is

$$A_{\mathrm{max}} = \frac{Y_1}{(Y_1 + Y_2)}$$
(2.39)

For the parameters considered in Fig. 2.9a, this matching condition occurs when $\Lambda \approx 23w$, which is consistent with Fig. 2.9c. We note that this circuit model can be generalized by including an inductor [55,69,70] in series with C_M to describe metal-graphene plasmonic devices coupled to antennas. In the circuit model, metal was treated as a perfect conductor. This is a very good approximation when metal

is gold with Drude conductivity ($\Gamma=3.33\times 10^{13}$ rad/s, $\omega_p=1.36 \times 10^{16}$ rad/s). It is possible to account for the ohmic loss in the metal by adding a resistor in series with C_M in the equivalent circuit model [63]. However, for the typical dimensions, frequencies, and conductivities considered here, the series resistance is calculated to be much smaller than the reactance of the capacitive grid. We do not expect that this equivalent circuit model can be applied at infrared and optical frequencies, where the metallic structure has its own plasmonic behavior that cannot be ignored [71,72].

2.4.2.3   Circuit Model vs Finite Element Calculations

Fig. 2.11 compares the transmission (T) and reflection (R) obtained from the full-wave finite element calculation (a and b) with the approximated values from circuit model (c and d). This figure exhibits close agreement between the results from circuit model (Fig. 2.11a) and the exact solution for different grating periods.

2.4.3   Measurement and Experimental Results

A single layer of graphene was formed on 8mm $\times$ 8mm semi-insulating (resistivity $> 10^{10}$ $\Omega\cdot$cm) (0001)6H-SiC terraces by the Si sublimation process in an Ar ambient. The substrates, misoriented from the basal plane by approximately 0.1 deg, were etched in H_2 prior to graphene synthesis [73]. Gold strips were fabricated on top of graphene using electron-beam lithography followed by Cr/Au (thickness: 5 nm/75 nm) thermal evaporation (Cr as the adhesion layer), and a lift-off process. The Au strips are 1.5 mm long and the whole grating is 1.5 mm wide creating a
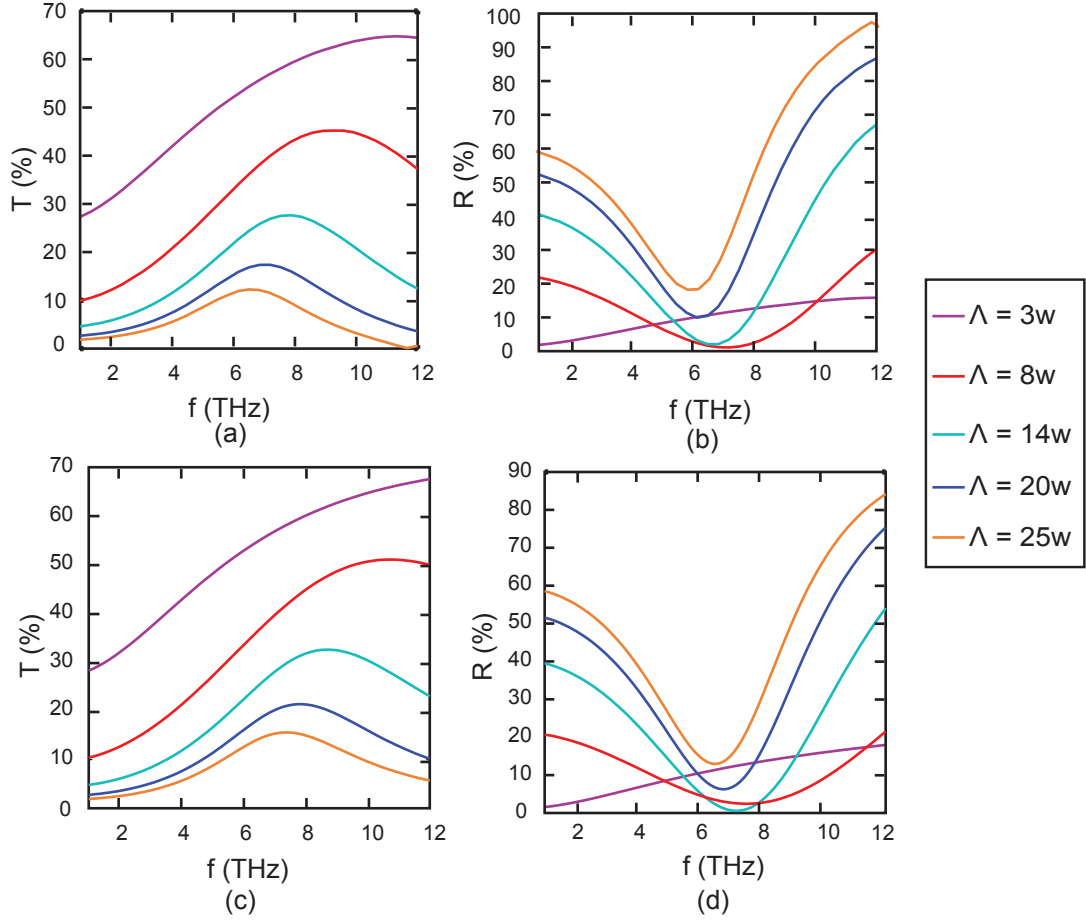
Figure 2.11: (a)/(b) transmission/reflection for different periods computed by full-wave finite element calculations. (c)/(d) transmission/reflection for different periods calculated by the circuit model shown in Fig. 2.10a. $\epsilon_1 = 1$ (air), $\epsilon_2 = 9$ (SiC), $w = 0.35$ μm, $\mu = 1000$ cm^2/Vs, $n = 1.5 \times 10^{13}$ cm^{-2}

grating that has a 2.25 mm^2 area. To electrically isolate the grating from other parts of the graphene/SiC chip, a narrow ribbon (7 μm) was defined by electron-beam lithography using PMMA resist as a mask and oxygen plasma to remove the unmasked areas. Finally, electrolyte (Polyethylene oxide/LiClO$_4$) was drop-cast on the sample as the top gate. The gate voltage was applied between the grating device and the other electrically isolated part of the SiC graphene substrate. Fig. 2.12 shows a scanning-electron micrograph image of a device with $w = 350$ nm and $\Lambda = 7\,\mu$m that was used to study the hybrid metal-graphene plasmons.
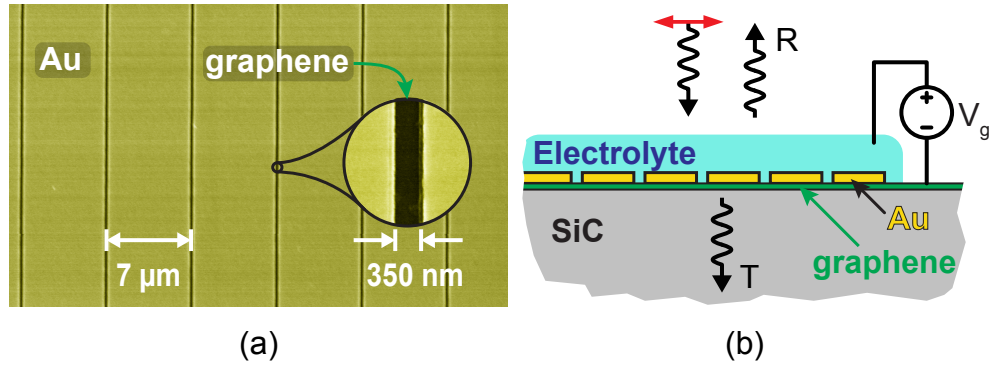
Figure 2.12: (a) The false-colored SEM image of the gold-graphene grating (top view). w=350 nm, $\Lambda = 7$ μm. (b) Diagram of the device with electrolyte top gate, and the reflection/transmission measurement scheme. The incident beam is polarized perpendicular to the gold strips.

Far infrared simultaneous transmission/reflection measurements are performed in a BOMEM DA-8 FTIR system with mercury lamp as a source and two 4 K silicon composite bolometers as detectors. A polarizer is placed in the beam path and only passes polarization perpendicular to metal strips. The 1.5×1.5 mm^2 metal-graphene grating device is mounted on a copper plate with a 1.5 mm diameter

aperture. The incident THz beam illuminated the back of the device making an angle about $10°$ from the normal. One bolometer is located on the transmitted beam path and one at the reflection side. A separate measurement on the sample without electrolyte was carried out to find and remove the electrolyte effect on the measured data.

Fig. 2.13a shows the measured transmission as a function of frequency for different carrier density levels tuned by application of the gate voltage V_g. A resonant peak is observed in the transmission, which grows in strength and shifts to higher frequency with increasing carrier density. In reflection, the plasmon resonance exhibits a minimum that also becomes stronger and blue-shifts as the carrier density is increased (Fig. 2.13b). In this figure, we present the reflection normalized to the lowest carrier density data to exhibit the plasmon resonance dip more clearly. The measured absorption $(A = 1 - R - T)$ is presented in Fig. 2.13c, showing how the frequency and strength of THz resonant absorption can be controlled by tuning the carrier density with a gate voltage. The carrier density was extracted from the plasmon frequency at each gate voltage and by comparing the experimental spectra to finite element calculations.

Finite element calculations of the same measured quantities presented in Fig. 2.13a and 2.13b respectively are shown in Fig. 2.13d and e, showing agreement with the experimental observations. Frequency-domain finite element calculations were performed on a unit cell of the metal-graphene grating on top of the SiC substrate (refractive index=3) with periodic boundary condition. The gold was modeled as a 75 nm thick Drude metal with Γ=3.33$\times 10^{13}$ rad/s, ω_p=1.36 $\times 10^{16}$ rad/s. The
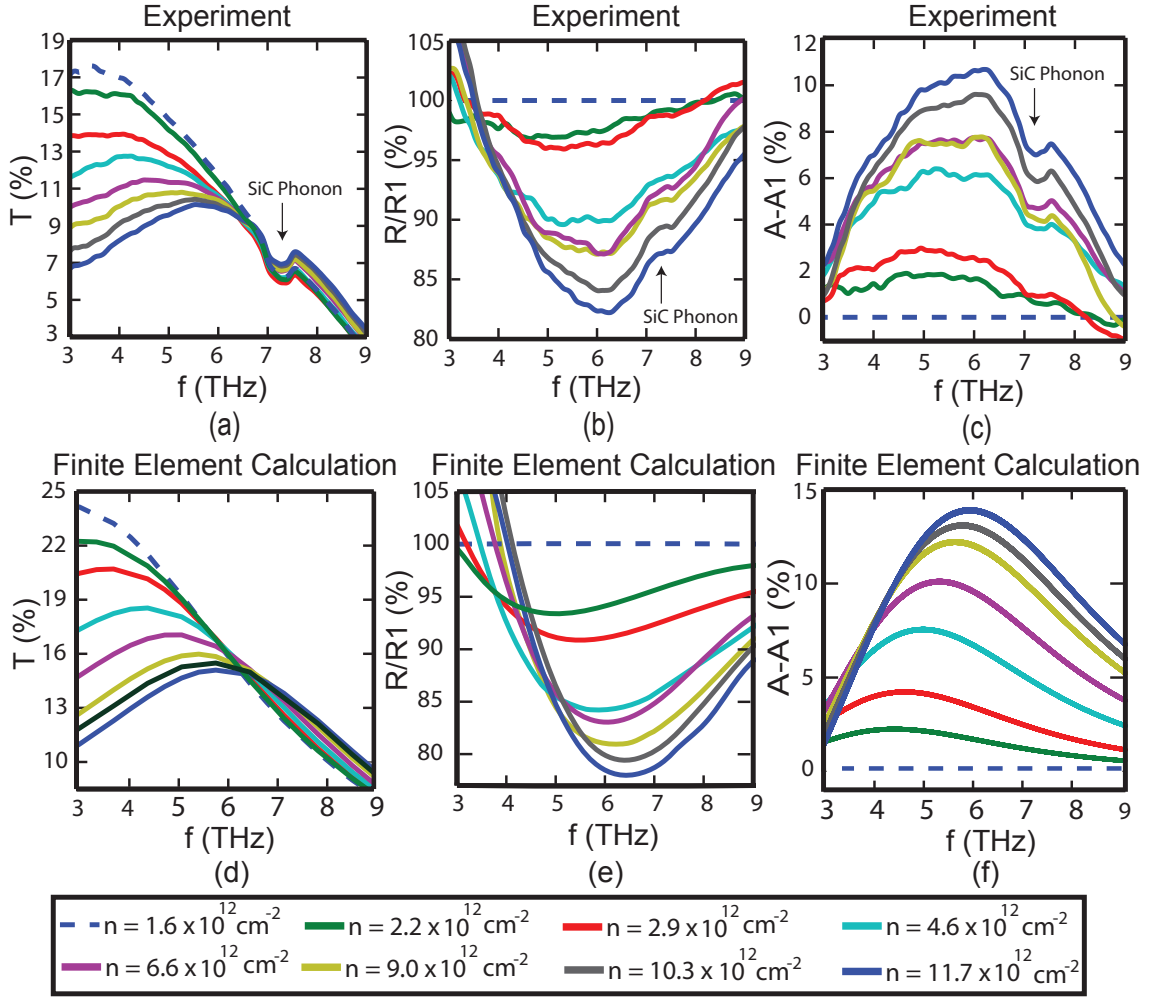
Figure 2.13: (a) Measured transmission (T) for different graphene carrier densities tuned by applying a gate voltage V_g. (b) Measured Reflection (R) off the device for different carrier densities normalized to the lowest carrier density ($n = 1.6 \times 10^{12}$ cm^{-2}) data. (c) Control of the device absorption (relative to the lowest carrier density) by electrically tuning the graphene carrier density ($A = 1 - R - T$). (d) Finite element calculations of transmission for different carrier densities . (e) Finite element calculations of the normalized reflection. $w = 350$ nm, $\Lambda = 7$ μm, $\mu = 1,010$ cm^{2}V^{-1}s^{-1} at $n = 5 \times 10^{12}$ cm^{-2}. The feature at 7.2 THz is the phonon resonance of the substrate (SiC). R1 and A1 are the reflection and absorption spectra for the lowest carrier density ($n = 1.6 \times 10^{12}$ cm^{-2}).

electrolyte on top of grating was modeled as a dielectric (refractive index=1.7). Currents, fields, and charge density in graphene and metal were calculated. Transmission and reflection of an incident plane-wave, polarized perpendicular to the metal strips, were also calculated. In the carrier-density-dependent calculations, a constant scattering rate was assumed for graphene. Mobility was taken to be $1{,}010 \text{ cm}^2\text{V}^{-1}\text{s}^{-1}$ at $n = 5 \times 10^{12} \text{ cm}^{-2}$, based on van der Pauw Hall measurements taken on the full graphene on SiC sample prior to processing. In the finite element calculations Fermi-level pinning at graphene-metal junction [74] was ignored. A constant Fermi level across the graphene channel and zero graphene-metal contact resistance were assumed. The close agreement between experimental results and theory suggest that the Fermi-level pinning and non-zero contact resistance effects are negligible in the devices we studied. However, we expect that they should have a noticeable effect for narrow graphene channels (<100 nm.) [74].

2.4.4   Geometrical Dependence

As with isolated graphene ribbons, the resonant frequency can also be changed by tailoring the width of the graphene channel, as predicted in (2.32). The equivalent circuit model predicts that the plasmon resonant frequency depends on the graphene channel width w and period Λ according to (2.32). Apart from the weak logarithmic dependence on the duty cycle w/Λ, the resonant frequency is predicted to scale in proportion to $w^{-1/2}$, as for isolated graphene ribbons [8,56]. To confirm this scaling relation, we conducted a second set of reflection measurements using a graphene

sample that was fabricated with a narrower channel. Fig. 2.14 shows the normalized reflection measurement for metal-graphene gratings with two different graphene channel widths of $w = 350$ nm and 200 nm. For the same carrier density, the resonant frequency is seen to increase by approximately 30% $(= \sqrt{350 \text{ nm}/200 \text{ nm}})$ when the width is decreased, as predicted by (2.32).
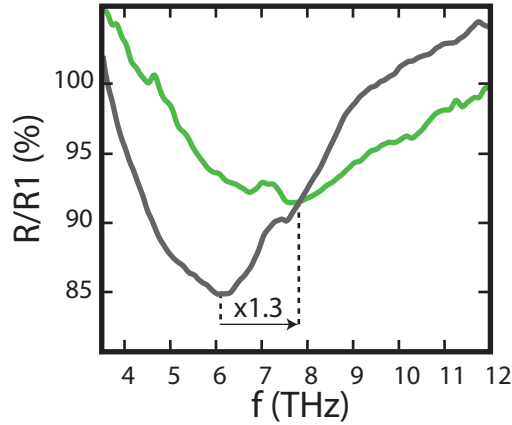
Figure 2.14: Comparison of measured normalized reflection for $w = 200$ nm, $\Lambda = 5$ μm (green curve), with $w = 350$ nm, $\Lambda = 7$ μm (gray curve) at the same carrier denisty $n = 10.3 \times 10^{12}$ cm^{-2}. Plasmon resonance is blue-shifted by about 30%.

Finally, we note that these metal-graphene plasmonic structures can exhibit near 100% resonant transmission in a high mobility graphene sample, a feature that could be very useful in THz transmission filters or modulators. Fig. 2.15a shows the calculated power transmission spectrum $T(f)$ for the case of $w/\Lambda = 1/20$, and for graphene mobilities ranging from 1,000 to 100,000 cm^{2}V^{-1}s^{-1} ($n = 1.5 \times 10^{13}$ cm^{-2}). When the graphene mobility is increased, the graphene absorption decreases, but is replaced by a resonant peak in the transmission that approaches 100% transmission in the limit of high mobility. Again, we note that this resonance shifts to zero
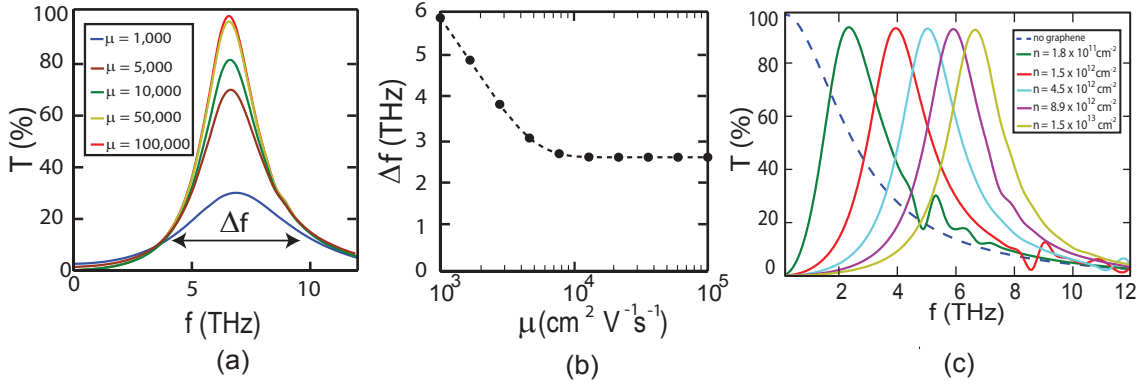
Figure 2.15: (a) Calculated transmission through the metal-graphene grating for different graphene mobility (μ) and $n = 1.5 \times 10^{13}$ cm^{-2}. (b) The plasmon resonance width as a function of graphene mobility. (c) Transmission through the metal-graphene grating for different carrier density levels. $w = 350$ nm, $\Lambda = 7$ μm, $\mu = 50,000$ cm^{2}V^{-1}s^{-1} at $n = 1.5 \times 10^{13}$ cm^{-2}. In all these results, the surrounding material was assumed to be uniform with $\epsilon = 5$.

frequency when the graphene is absent or charge-neutral, proving that the inductive graphene channel is essential to support the plasmonic resonance. As shown in Fig. 2.15b, the spectral width of this resonance decreases inversely with the mobility, but reaches a plateau in the limit of high mobility. Above this point, the plasmon linewidth is dominated by radiation damping, and cannot be further reduced by improving the material quality, as predicted by (2.34). In contrast to isolated graphene ribbons, the plasmons in metal-contacted graphene are naturally radiative – a feature that can have important consequences in tunable graphene emitters. Fig. 2.15c demonstrates the tunability of the near 100% resonant transmission through changing the graphene carrier density. The calculated transmission spectra also illustrate the existence of higher order plasmon modes that are not described by the simple equivalent circuit model of Fig. 2.10. The next section briefly considers these higher order modes and how they can be optimized.

2.4.5   Higher Order Plasmon modes

Beyond the fundamental mode that is considered in this letter, higher order plasmon modes also exist in the hybrid graphene-metal structure. Fig. 2.16a shows the charge density profile for the next dipole-active (third order) mode. Fig. 2.16b is the same plot as in Fig. 1e but extended to show the behavior at higher frequencies. The third order mode appears as a small peak in the absorption around 17 THz. For the parameters chosen in this figure, the highest on-resonant absorption is obtained for $\Lambda = 8w = 2.8$ μm (red curve).
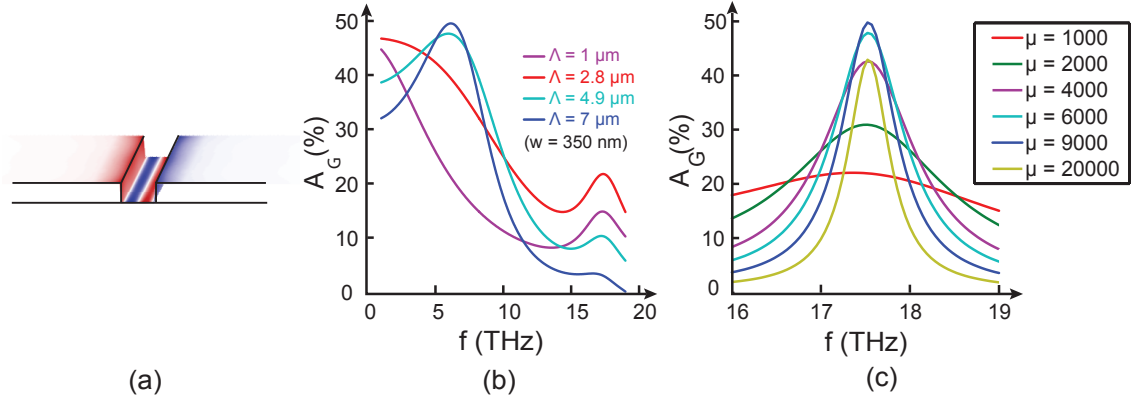
Figure 2.16: (a) Charge density profile at the 3rd plasmon mode frequency for metal-graphene structure. (b) Graphene absorption (A_G) under plane-wave excitation of metal-graphene gratings with different periods ($w = 350$ nm, $n = 1.5 \times 10^{13}$ cm^{-2}, $\mu = 1000$ cm^2 /Vs). The surrounding material was assumed to be uniform ($\epsilon_1 = \epsilon_2 = 5$). (c) Graphene absorption in metal-graphene gratings ($w = 350$ nm, $n = 1.5 \times 10^{13}$ cm^{-2}) with $\Lambda = 8w$ as a function of graphene mobility. The absorption is close to the maximum value (50%) for $\mu = 9000$ cm^{2}V^{-1}s^{-1}.

For the higher order modes, the equivalent circuit model Figure 2.10 can no longer be used to characterize the resonant frequency and radiative damping rate. We nonetheless expect that, as with the fundamental mode, optimal resonant absorption in the graphene can be attained when the radiative losses are matched to the graphene scattering rate. To confirm this principle, we varied the scattering rate Γ by changing the mobility μ. Figure 2.16c plots the calculated absorption for $\Lambda = 2.8$ μm for six different graphene mobilities ranging from 1000 to 20,000 cm^{2}V^{-1}s^{-1}. The absorption at the 3rd order peak approaches the theoretical maximum (50%) for graphene mobility of 9,000 cm^{2}V^{-1}s^{-1}. This demonstrates that, unlike most plasmonic structures in which higher order modes are weakly coupled to the incident plane-wave, the plasmon modes in the hybrid graphene-metal system can be efficiently excited by appropriately choosing the geometry of the metal contacts and graphene properties.

These results demonstrate how the hybrid metal-graphene resonances can be designed and tuned to produce strongly enhanced absorption at a chosen resonant frequency. These hybrid plasmon modes could also be incorporated in graphene-integrated metamaterials [55, 75, 76], where the metal-graphene plasmon enhances the metamaterial resonance.

2.5 Conclusion

We report a new type of plasmon resonance that occurs when graphene is connected to a metal. These new plasmon modes offer the potential to incorpo-

rate a tunable plasmonic channel into a device with electrical contacts, a critical step towards practical graphene terahertz optoelectronics. Through theory and experiments, we demonstrate, for example, anomalously high resonant absorption or transmission when subwavelength graphene-filled apertures are introduced into an otherwise conductive layer. These tunable plasmon resonances are essential yet missing ingredients needed for terahertz filters, oscillators, detectors, and modulators.

Chapter 3: Nonlinear Terahertz Response of Graphene Plasmons

3.1 Overview

In the terahertz and mid-IR regime, the light-graphene interaction can be greatly increased by exploiting plasmon resonances, where the field is strongly localized and resonantly enhanced in a sub-wavelength graphene region [57, 77]. A dramatic enhancement of the linear absorption has been experimentally observed in isolated subwavelength graphene elements [8, 78, 79], and graphene-filled metallic apertures [51] at resonant frequencies that can be controlled through the graphene dimensions and carrier concentration. Significant enhancement in the nonlinear response of graphene can be expected and has been theoretically predicted [57, 80–83]. To date, there have been no experimental demonstrations to study this effect, or to explore the energy loss dynamics of these collective plasmonic excitations.

3.2 Nonlinear Plasmonic Response of CVD Graphene Ribbons

3.2.1 Overview

In this section, we measure the nonlinear response of plasmon resonances in an array of graphene nanoribbons using THz pump-THz probe measurements with

a free-electron laser that is tuned to the plasmon resonance (9.4 THz.) We observe a resonantly-enhanced pump-induced nonlinearity in the transmission that is orders of magnitude stronger than that of unpatterned graphene. The pump-probe measurements reveal an energy relaxation time of approximately 10 ps (measured at 20K). We present a thermal model of the nonlinear plasmonic response that includes scattering through LA phonons and disorder-assisted supercooling, which matches both the observed timescale and power-scaling of the nonlinear response [84].

3.2.2   Device Fabrication and FTIR Characterization

The plasmonic devices were fabricated using CVD-grown monolayer graphene that was transferred onto a 300 nm silicon oxide on lightly doped silicon (250 Ω·cm). Graphene ribbons with width w =730 nm and period Λ =1.5 μm were patterned using electron-beam lithography with a PMMA resist and oxygen plasma etch to remove the graphene from the exposed areas. The graphene grating covered a region of 1.5 $\times$ 1.5 mm. Fig. 3.1a-b shows the structure, dimensions, and scanning-electron micrograph of the graphene plasmonic resonant structure considered here, and Fig. 3.1c shows the measured room-temperature linear transmission spectrum of the sample, which exhibits a strong dip in transmission centered at 9.4 THz that is associated with plasmonic absorption of the nanoribbons.

The plasmon resonance can be approximated by assuming an equivalent sheet conductivity of the graphene ribbon array [61,64] (Chapter 2, section 2.3.4),

$$\sigma(\omega) = \frac{w}{\Lambda} \frac{D}{\pi[\Gamma - i(\omega^2 - \omega_p^2)/\omega]} \tag{3.1}$$

where Γ is the scattering rate and $D \simeq \sqrt{\pi n} e^2 v_F / \hbar$ is the Drude weight of graphene with a carrier concentration of n and Fermi velocity v_F. The plasmon resonant frequency is related to the Drude weight by $\omega_p^2 \equiv Dw / [2\Lambda^2 \epsilon_0 \bar{\epsilon} \ln{(\sec{(\pi w/2\Lambda)})}]$, where $\bar{\epsilon} = (\epsilon_1 + \epsilon_2)/2$ is the average of the substrate and incident dielectric constants [64].

The relative power transmission through such a conductive sheet, accounting for reflection and transmission by the silicon substrate, is given by (Chapter 2, section 2.2.1)

$$\tau(\omega)/\tau_0 = |1 + \sigma(\omega)/(Y_1 + Y_2)|^{-2} \qquad (3.2)$$

where τ_0 denotes the transmission with the graphene film absent, and $Y_j \equiv (\epsilon_0 \epsilon_j / \mu_0)^{1/2}$ is the admittance of the incident ($j = 1$) or substrate ($j = 2$) region. The green curve in Fig. 3.1b shows the best-fit transmission spectrum calculated using this model, from which we determined the carrier concentration and graphene scattering rate to be $n = 9 \times 10^{12}$ cm^{-2} and $\Gamma = 23$ rad/ps, respectively at room temperature, which corresponds to a Fermi energy of 0.35 eV and carrier mobility of 1,250 cm^{2}V^{-1}s^{-1}.

3.2.3 Pump-probe Measurements

Fig. 3.2 illustrates the experimental setup that was used to investigate the nonlinear THz response of the graphene plasmons. The free electron laser was tuned to produce 5.5 ps pulses with a repetition rate of 13 MHz that are resonant to
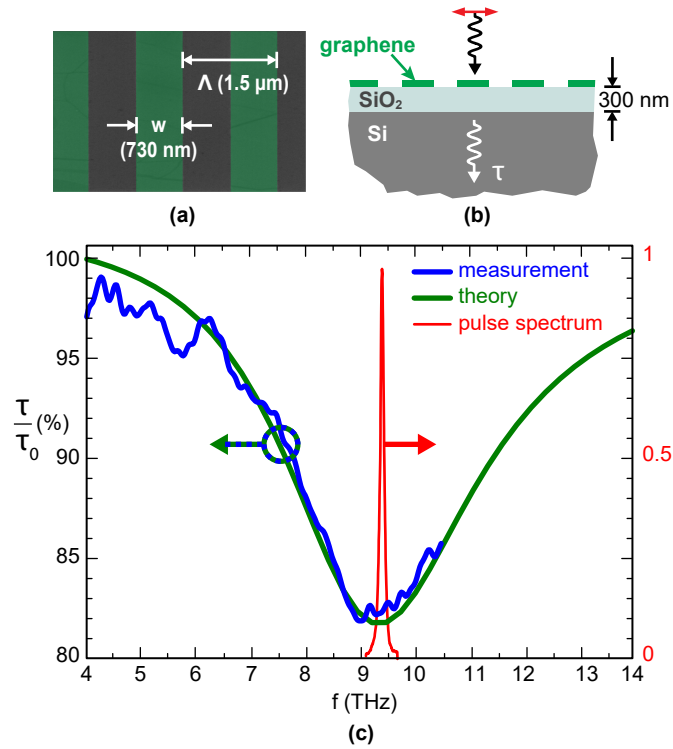
Figure 3.1: (a) False color scanning electron micrograph of fabricated graphene ribbons. (b) Cross sectional diagram of device. (c) Measured (blue) and best fit (green) linear transmission spectrum of device, showing a decreased transmission at the plasmon frequency of 9.4 THz. The superposed red curve shows the measured spectrum of the free electron laser pulse source that was used to observe the nonlinear response.

the plasmon frequency of 9.4 THz. Compared to the plasmon resonance, the FEL radiation was spectrally narrow (cf. Fig. 3.1c) The beam was split into pump and probe beams that were delayed relative to one another using a mechanical delay line. In all measurements the pump and probe beams were co-polarized, but the state of polarization could be set to be either perpendicular or parallel to the graphene ribbons, in order to control whether or not the plasmons were excited, respectively. An off-axis parabolic mirror was employed to focus and overlap both beams at the graphene ribbon array. The sample was cooled to a (lattice) temperature of 20 K for all of the pump-probe measurements. While the emerging pump beam was extinguished, the intensity of the transmitted probe beam was measured using a cryogenically cooled bolometer as a function of the pump-probe delay Δt.

This signal, recorded as a function of the pump-probe delay Δt, is depicted in Fig. 3.3a for several pump fluences. In all cases, the pump causes a transient increase in transmission that is accompanied by a decrease in absorption. The observed nonlinear response decays in the wake of the pump pulse with a time constant of $\sim$ 10 ps, which is close to the previously reported hot electron-phonon relaxation time in graphene at the measurement temperature (20 K) [85].

3.2.4   Discussion and the Nonlinear Thermal Model

The electron temperature T in the graphene evolves in response to the terahertz pump pulse with intensity $I(t)$ at the center frequency ω_0 according to [31]

$$\alpha T \frac{dT}{dt} + \beta(T^3 - T_L^3) = A(\omega_0; T)I(t) \tag{3.3}$$
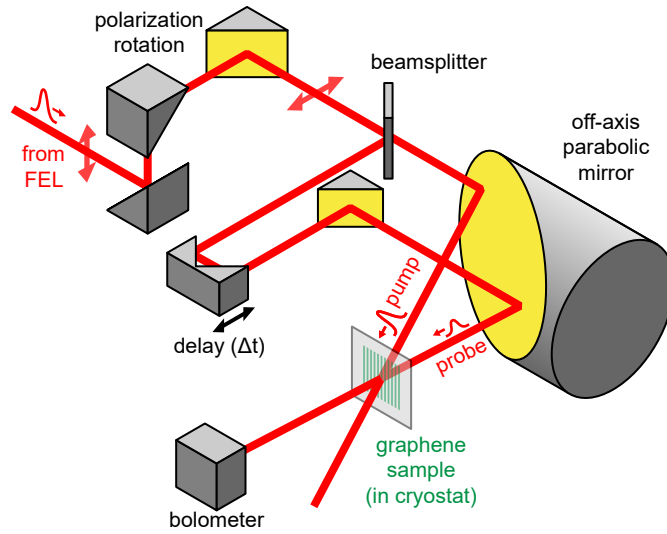
Figure 3.2: Sketch of the experimental setup for the pump-probe measurements. An optional reflective polarization rotation system orients the polarization perpendicular to the graphene ribbons. The pulses were separated into parallel, co-polarized pump and probe pulses that were focused onto the graphene sample inside of a cryostat. The transmitted probe power was measured as a function of the relative pump-probe delay Δt, which was controlled through a mechanical delay stage.

where αT is the specific heat of graphene with $\alpha = 2\pi k_B^2 \varepsilon_F/(3\hbar^2 v_F^2)$, $\beta = \zeta(3)V_D^2 \varepsilon_F k_B^3/(\pi^2 \rho \hbar^4 v_F^3 s^2 l)$ is the cooling coefficient, T_L is the lattice temperature, $A(\omega_0; T)$ is the fractional absorption in the graphene, which itself depends on temperature. k_B is the Boltzmann constant, ρ is the areal mass density, s is the speed of sound in graphene, ζ is the Riemann zeta function, l is the electron-disorder mean free path, and V_D is the acoustic deformation potential. We assume that the temperature relaxation is dominated by disorder-assisted supercollision cooling $\propto T^3$ [31, 86], rather than momentum-conserving cooling [87].

The fractional absorption appearing in (3.2) can be derived from the equivalent conductivity (3.1) (Chapter 2, section 2.2.1),

$$A(\omega_0; T) = \frac{4Y_1 \operatorname{Re}\{\sigma(\omega_0)\}}{|Y_1 + Y_2 + \sigma(\omega_0)|^2} \tag{3.4}$$

where ω_0 denotes the carrier frequency of the quasi-CW pump and probe pulses. The basis of the thermal model is that the Drude weight D, scattering rate Γ, and plasmon frequency appearing in (3.1) implicitly depend upon the electron temperature T, which increases when the incident pump pulse is absorbed in the graphene layer.

The temperature-dependent Drude weight [5,88] and plasmon frequency (Chapter 2, section 2.3.4) are calculated as

$$D(T) = \frac{2e^2}{\hbar^2} k_B T \ln\left[2\cosh\left(\frac{\mu(T)}{k_B T}\right)\right] \tag{3.5}$$

$$\omega_p^2(T) = \frac{D(T)w}{2\epsilon_0 \bar{\epsilon}\Lambda^2 \ln\left(\sec\left(\pi w/2\Lambda\right)\right)} \tag{3.6}$$

The scattering rate Γ also varies with temperature, both because of temperature-dependent scattering from long-range Coulomb impurities and longitudinal acoustic

(LA) phonons [89].

$$\Gamma(T) = \frac{\Gamma_0 \varepsilon_F}{\mu(T)} + \frac{k_B T \varepsilon_F V_D^2}{4\hbar^3 v_F^2 \rho s^2} \qquad (3.7)$$

The second term in (3.7) describes the temperature dependent LA phonon scattering, which was essential in order to match the observed fluence dependence of the nonlinear response, shown in Fig. 3.3c. The fluence dependence will be discussed further in this section.

As the fast electron-electron scattering leads to a thermalization of the carrier distribution on a time scale of femtoseconds, we assume that the electron population maintains a Fermi distribution, with a temperature that evolves in response to the terahertz pump pulse according to (3.2). The total electron population n must remain constant as the electrons heat and cool, which defines the following implicit relationship between the electron temperature and the chemical potential $\mu(T)$,

$$n = \int_{-\infty}^{\infty} \frac{\nu(E)dE}{1 + \exp\left[\dfrac{E - \mu(T)}{k_B T}\right]} \qquad (3.8)$$

where $\nu(E)$ is the density of states in graphene. For a given temperature T, (3.4) can be numerically solved to determine the associated chemical potential $\mu(T)$.

To account for the duration of the pump pulse in our experiment, which is of the same order of magnitude as the carrier relaxation time, the temporal evolution of the carrier temperature is calculated by numerically solving (3.2) via the Euler's method, assuming a 5.5 ps Gaussian input pulse $I(t)$. At each time-step, the chemical potential, Drude weight, plasmon frequency, conductivity, and fractional absorption for the subsequent time step were adjusted based upon (3.4), (3.5), (3.6), (3.1) and (3.3), respectively. The step size for this calculation is an order of mag-

nitude smaller than the duration of the pump pulse to minimize the error caused by this step by step solution. Knowing the instantaneous temperature transient $T(t)$, the fractional change in probe transmission is then numerically computed as a function of the pump-probe delay Δt using a correlation integral.

The results from the thermal model (Fig. 3.3b) are in close agreement with the experimental data (Fig. 3.3a), and correctly predict the 10 ps response time. This agreement suggests that non-thermal nonlinearities in graphene, which were theoretically proposed in recent studies [90,91], are weak in our experiment. The increased transmission is a result of a decreased plasmon frequency, which is caused by a reduced value of the chemical potential at elevated electron temperatures (cf. Eq. (3.4) and (3.5)), and a broadening of the resonance caused by a faster scattering rate. While both effects lead to an increased transmission at resonance, the calculations show a decreased transmission for photon frequency below the plasmon resonance (to be discussed in section 3.2.7). At higher fluence, our measurements show a longer tail that is not reproduced by the model. This slight discrepancy might be caused by a bottleneck in the phonon heating [92], which was not included in our model. Fig. 3.3c plots the peak value of the (observed and calculated) transient response as a function of the incident pump fluence F, which shows an approximate $F^{1/2}$ dependence. Along the right axis, we plot the corresponding simulated peak electron temperature as a function of fluence, showing the expected $F^{1/3}$ dependence. The observed power scaling was best matched by assuming supercollision cooling as the single dominant cooling mechanism, together with temperature-dependent momentum scattering through LA phonons [5,89].
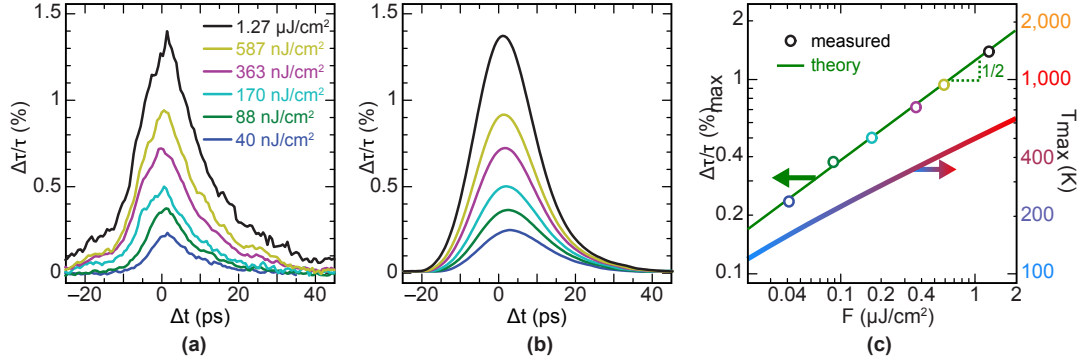
Figure 3.3: (a) Measured relative change in transmission of the probe signal for different pump fluences as a function of pump-probe time delay Δt. The positive signal indicates a decrease in absorption that becomes stronger at higher pump fluences. (b) Calculated relative change in transmission based on a nonlinear thermal model for plasmonic absorption in graphene nanoribbons that includes supercollision cooling and LA phonon scattering. (c) Measured and simulated peak of relative transmission change (left) and peak electron temperature (right) as a function of pump fluence F.

Only two free parameters were used in the numerical simulations: the acoustic deformation potential V_D and the electron disorder mean free path l, which together control the strength of dominant cooling and scattering mechanisms. The observed $F^{1/2}$ power scaling seen in Fig. 3.3c was matched by choosing $V_D = 11$ eV, which is consistent with values reported in the literature for similar graphene [87, 93]. The mean free path l was adjusted to match the overall magnitude of the nonlinearity, from which we obtained $l = 2$ nm, which is smaller than that expected from the scattering rate, but consistent with other recent experimental measurements of cooling in large-area graphene [93]. The origin of this discrepancy remains to be explained.

3.2.5   Fluence Dependence

As shown in Fig. 3c, the pump-induced change in transmission $\Delta\tau$ increases approximately with the fluence $F^{1/2}$. Here we present a approximate model to explain the nature of this dependence.

The on-resonant transmission through the plasmonic ribbons can be expressed in terms of the three temperature dependent parameters D, Γ and ω_p^2 using (3.1) and (3.2):

$$\tau = \frac{4Y_1 Y_2}{\left| Y_1 + Y_2 + \dfrac{w}{\Lambda} \dfrac{D}{\pi[\Gamma - i(\omega^2 - \omega_p^2)/\omega]} \right|^2} \tag{3.9}$$

When the relative changes in these parameters are small, as is the case for the measurements reported here, the resulting fractional change in transmission $\Delta\tau/\tau$ may be approximated by Taylor-expanding (3.9) to first order, with the assumption

53

that $\omega = \omega_p$,

$$\frac{\Delta\tau}{\tau} = \frac{2\frac{w}{\Lambda}\frac{D}{\pi\Gamma}}{\left[Y_1 + Y_2 + \frac{w}{\Lambda}\frac{D}{\pi\Gamma}\right]}\left(\frac{\Delta\Gamma}{\Gamma} - \frac{\Delta D}{D}\right) \tag{3.10}$$

We note that when evaluated at the resonant frequency, the thermally-induced red-shift $\Delta\omega_p^2$ causes only a higher-order change in $\Delta\tau$, which is omitted in (3.10).

The Drude weight can be approximated as

$$D(T) = \frac{2e^2}{\hbar^2}k_B T \ln\left[2\cosh\left(\frac{\mu(T)}{k_B T}\right)\right] \tag{3.11}$$

$$\simeq \frac{2e^2}{\hbar^2}\mu(T) \tag{3.12}$$

$$\simeq \frac{2e^2\varepsilon_F}{\hbar^2}\left(1 - \frac{\pi^2 k_B^2 T^2}{6\varepsilon_F^2}\right) \tag{3.13}$$

In the second line, we have used the fact that even for the hottest electron temperatures considered (660 K = 57 meV), the Fermi energy (350 meV) and chemical potential significantly exceed $k_B T$. In the third line we have employed the Sommerfeld expansion to approximate the relation between electron temperature T and chemical potential $\mu(T)$. The fractional decrease in Drude weight is then found to be:

$$\frac{\Delta D}{D} = -\frac{\pi^2 k_B^2 T^2}{6\varepsilon_F^2} \tag{3.14}$$

We note that the change is estimated relative to that at absolute zero temperature, whereas in the measurements, the lattice temperature was small ($T_0 = 20$ K), but non-zero.

The scattering rate can likewise be approximated as:

$$\Gamma(T) = \frac{\Gamma_0 \varepsilon_F}{\mu(T)} + \frac{\varepsilon_F V_D^2 k_B T}{4\hbar^3 v_F^2 \rho s^2} \tag{3.15}$$

$$\simeq \Gamma_0 \left(1 + \frac{\pi^2 k_B^2 T^2}{6\varepsilon_F^2} \right) + \frac{\varepsilon_F V_D^2 k_B T}{4\hbar^3 v_F^2 \rho s^2} \tag{3.16}$$

where we have again assumed $\varepsilon_F \gg k_B T$ and employed the Sommerfeld expansion. The fraction increase in scattering rate (relative to absolute zero temperature) is then given by:

$$\frac{\Delta\Gamma}{\Gamma} = \frac{\varepsilon_F V_D^2 k_B T}{4\Gamma_0 \hbar^3 v_F^2 \rho s^2} + \frac{\pi^2 k_B^2 T^2}{6\varepsilon_F^2} \tag{3.17}$$

When (3.14) (3.17) are combined as in (3.10), both effects sum to cause an increase in the transmission that is proportional to:

$$\left(\frac{\Delta\Gamma}{\Gamma} - \frac{\Delta D}{D} \right) = \frac{\varepsilon_F V_D^2 k_B T}{4\Gamma_0 \hbar^3 v_F^2 \rho s^2} + \frac{\pi^2 k_B^2 T^2}{3\varepsilon_F^2} \tag{3.18}$$

The first term ($\propto T$) is associated with the temperature-dependent LA phonon scattering rate, and the second term ($\propto T^2$) results from the temperature-dependent chemical potential. The relative strength of these two terms is related to the deformation potential V_D, which was adjusted to match the experimentally observed fluence dependence. For the parameters considered in the experiment, these two terms would be equal to one another at an electron temperature of $T = 336$ K. For the range of experimental conditions considered here, neither term can be neglected, and hence we expect a dependence of $\Delta\tau$ on electron temperature T that falls somewhere between linear and quadratic.

For the narrow-band terahertz pulses considered here, the relationship between peak temperature T and fluence F can be estimated by assuming that the peak

temperature and peak intensity are nearly coincident in time. From equation (2) in the main text,

$$\beta T_{\max}^3 = A(\omega) I_{\max} \tag{3.19}$$

where $T_{\max}$ denotes the peak electron temperature, and $I_{\max} = 0.94 F / \Delta t_{\mathrm{FWHM}}$ is the peak intensity of a Gaussian pulse with fluence F and duration Δt_{FWHM}. We have again neglected the small term βT_0^3 on the left-hand side that describes the lattice temperature, and ignored the higher-order temperature-dependent change in the absorption coefficient A appearing on the right-hand side. (3.19) predicts that the peak temperature will scale as $F^{1/3}$, as confirmed by the numerical simulations of Fig. 3c.

Substituting this relationship into (3.18), one concludes that for the experimental conditions considered here the change in transmission $\Delta \tau$ should exhibit a non-power-law dependence on fluence that falls intermediate between $F^{1/3}$ and $F^{2/3}$. As shown in Fig. 3b, empirically observed and simulated scaling relation close to $F^{1/2}$ is consistent with this model. We note that including the temperature-dependent LA phonon scattering in addition to conventional Coulomb impurities was essential to correctly match the observed fluence dependence.

3.2.6 Nonlinear Signal with No Excited Plasmons

To confirm the plasmonic enhancement of the nonlinearity, we repeated the pump-probe measurements with the pump and probe co-polarized in the direction parallel to the graphene ribbons, thus ensuring that the plasmons are not excited.

Fig. 3.4a compares the measurements from the two polarization cases for the same incident pump fluence and frequency. The measured nonlinearity is far stronger when the plasmons are excited than for the opposite polarization, consistent with the thermal predictions. Fig. 3.4b shows the electric field profile at the plasmon resonance, estimated by frequency-domain finite element calculations, showing the dramatic field enhancement that occurs near the graphene sheet, which contributes to the enhanced nonlinearity.

3.2.7 Frequency Dependence of the Nonlinear Absorption

The increased carrier temperature changes the strength of the plasmon absorption as well as its resonance frequency. Hence, the nonlinear absorption is highly frequency dependent. While both effects lead to an increase of the transmission at resonance, the situation changes for photon frequencies below resonance. In this case, red shift of the plasmon resonance leads to a decrease of the transmission, opposed to the effect of the weakened plasmon absorption. Whether the overall change in transmission is positive or negative depends on which of these processes dominates. To investigate this behavior, we calculated the change of the transmission as a function of the probe photon frequency with the model described in the main text. The parameters of the calculation were the same as in the simulation of the experiment, only the photon frequency of the probe was varied. The calculated change in transmission as a function of the probe frequency for different pump-induced electron temperature rise is depicted in Fig. 3.5. Our calculations show clearly that the
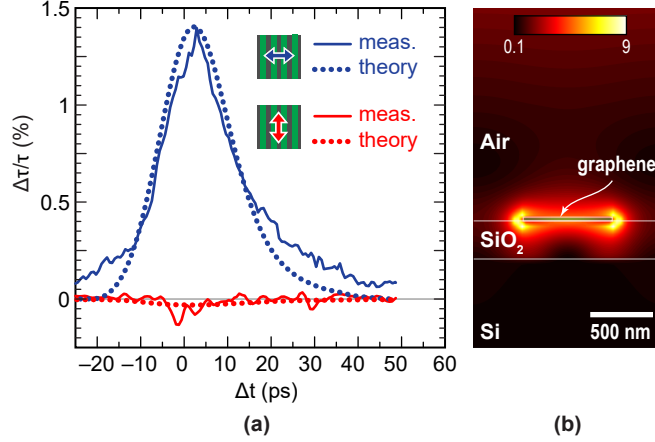
Figure 3.4: (a) Comparison of normalized change in transmission for two differ-
ent polarizations. The blue curves show the measured and simulated pump-probe
response when the pump and probe were polarized perpendicular to the graphene
nanoribbons, thereby exciting the plasmon. The red curves show the measured and
simulated response for the same incident pump fluence, but opposite polarization,
where there is no plasmonic excitation, and the nonlinear response is correspond-
ingly much lower. (b) Electric field profile at the resonant frequency, calculated
using a (linear) finite element time domain method with a normally incident wave
from above, showing the field-enhancement at the graphene surface. The color in-
dicates the electric field intensity $|\mathbf{E}|^2$, relative to that of the incident plane wave,
showing a nearly 9-fold intensity enhancement at the graphene surface.

red shift is the dominating effect and therewith the overall pump-induced change in transmission is predicted to be negative for photon frequencies below resonance.
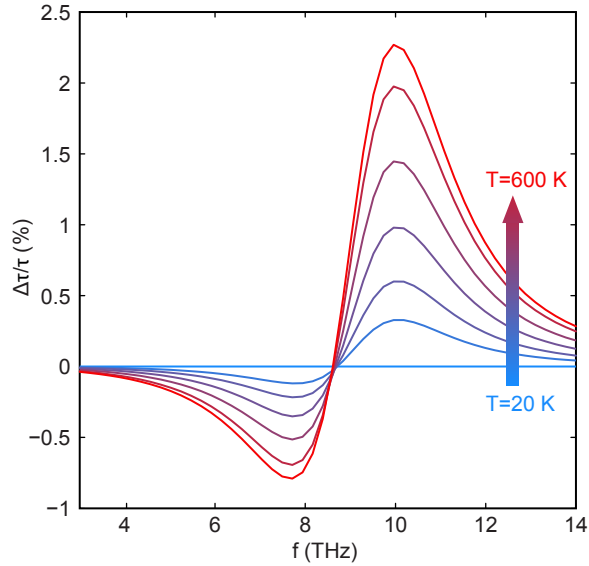
Figure 3.5: Peak change of transmission as function of frequency calculated for the sample used in our experiments.

3.3   Pump-probe Measurements on QFSBL-graphene Ribbons

3.3.1   Overview

In this section, we present nonlinear pump-probe measurements on an array of quasi-free-standing bilayer graphene (QFSBL-graphene)ribbons. These graphene samples have low carriers scattering rate, by about a factor of 3 smaller than the CVD graphene considered previously in this chapter. This leads to sharper/stronger plasmon resonances and much higher nonlinear response, as predicted in previous section. We also study the nonlinear response of graphene ribbons at different fre-

quencies around the plasmon resonance. These measurements confirm the nonlinear red-shift of plasmon resonance predicted by our nonlinear thermal model.

3.3.2 Device Fabrication and FTIR Characterization

The plasmonic graphene ribbons devices were fabricated on QFSBL-graphene. Ribbons with width $w = 900$ nm and period $\Lambda = 1.2$ μm were patterned using electron-beam lithography with a PMMA resist and oxygen plasma etch to remove graphene from the exposed areas. The graphene grating covered a region of 1.5×1.5 mm. Fig. 3.6 plots the measured room-temperature linear transmission spectrum of the sample, which exhibits a strong narrowband plasmonic absorption at 3.9 THz. The green curve shows the Drude-Lorentz fit to the measured FTIR spectrum using $n = 9 \times 10^{12}$ cm^{-2} and $\Gamma = 8.6$ rad/ps. Based on the fit, the QFSBL-graphene has a similar carrier density to the CVD graphene considered before, but the scattering rate is 2.7 times smaller. For Drude-Lorentz fitting to the measured data, we used the extinction ratio and the resonance width as free parameters and assumed a resonance frequency at 3.9 THz as observed from FTIR measurements.

3.3.3 On-Plasmon Resonance Pump-Probe Measurements

We employ transmission pump-probe measurements (Fig. 3.2) to study nonlinear response of QFSBL-graphene ribbons at the plasmon resonance (3.9 THz). Both pump and probe are polarized perpendicular to graphene ribbons. Fig. 3.7a shows the measured relative change in transmission of the probe for different pump
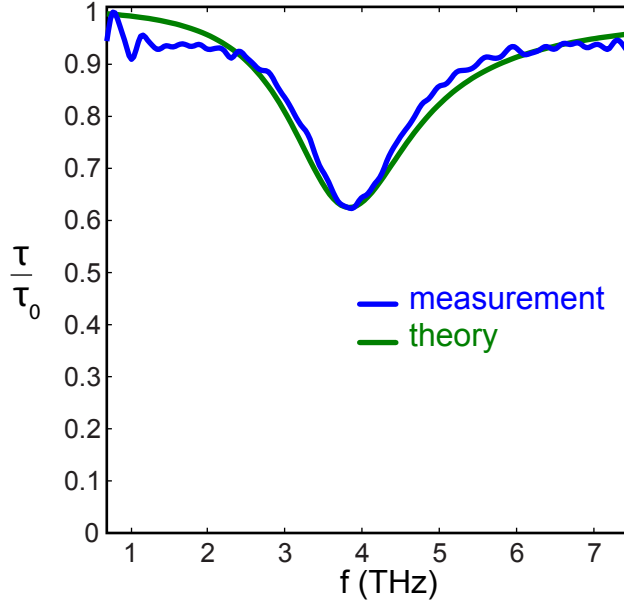
Figure 3.6: Measured (blue) and best fit (green) linear transmission spectrum of device, showing a decreased transmission at the plasmon frequency of 3.9 THz.

fluences as a function of pump-probe time delay. A very strong saturable absorption of plasmons is observed, which increases at higher pump fluences. We note that, for a similar pump fluence, the saturable absorption is about 6 times stronger than what observed on CVD graphene with 2.7 times larger scattering rate, i.e. wider/weaker plasmon resonance (Fig. 3.3a). In general, it is expected that nonlinearity significantly grows with decreasing losses in graphene, as the effect of both nonlinear thermal widening and red-shifting of plasmon resonances is more significant for stronger/spectrally-narrower plasmon resonances.

Fig. 3.7b shows the measured peak of relative transmission change as a function of pump fluence, which exhibits a square-root-like dependence similar to the observed results in CVD graphene ribbons (Fig. 3.3c). Based on our nonlinear thermal model, the observed square-root fluence dependence suggests that QFSBL-

graphene and the CVD graphene considered here have similar deformation potential V_D and supercollision cooling coefficient β_3.

Figure 3.7: (a) Measured relative change in transmission of the probe signal for different pump fluences as a function of pump-probe time delay Δt. The positive signal indicates a decrease in absorption that becomes stronger at higher pump fluences. (b) Measured peak of relative transmission change as a function of pump fluence F. The black curve is a square-root fit to the measured data.

3.3.4 Frequency Dependence in the Nonlinear Thermal Response

In this section, we measure and theoretically model the nonlinear thermal response of graphene plasmons at different frequencies. The pump-probe measurements presented here are similar to what discussed previously in this chapter with two distinctions: (i) Pump is polarized parallel to ribbons (probe polarization: perpendicular to ribbons). Therefore, the pump pulse doesn't excite plasmons

in graphene ribbons and only elevates the electron temperature. (ii) Pump/probe frequency is varied around the plasmon frequency (3.9 THz) from 2 THz to 4.9 THz.

Fig. 3.8a presents the measured relative change in transmission of probe for different pump/probe frequencies. The largest change in transmission is observed close to the plasmon frequency and becomes smaller by going off-resonance to either sides of the resonance. The fact that for the same amount of off-resonance detuning, a positive signal (same sign as on-resonance case) observed on the blue side but a negative signal on the red side suggests a pump-induced red-shift of plasmon frequency. This is consistent with the nonlinear red-shift of plasmon resonance predicted by the thermal model for nonlinear plasmon response (section 3.2.4).

Fig. 3.8b plots the largest (positive or negative) relative change in transmission as a function of frequency f. The black curve is theory calculations based on the nonlinear thermal model described in section 2.2.4. The calculations exhibits a very good agreement with the measured results using the deformation potential $V_D = 12$ eV and disorder mean free path l=1 nm which are very close to the values we used to simulate the nonlinear response for the CVD graphene ribbons in section 2.2.4.

As shown in Fig. 3.8b, the large on-resonance positive signal becomes negative at 3.25 THz (0.65 THz below resonance) and 5.05 THz (1.15 THz above resonance). This asymmetric feature around the plasmon frequency is a clear manifestation of pump-induced red-shift (about 0.25 THz) of plasmon resonance due to increase in electron temperature.
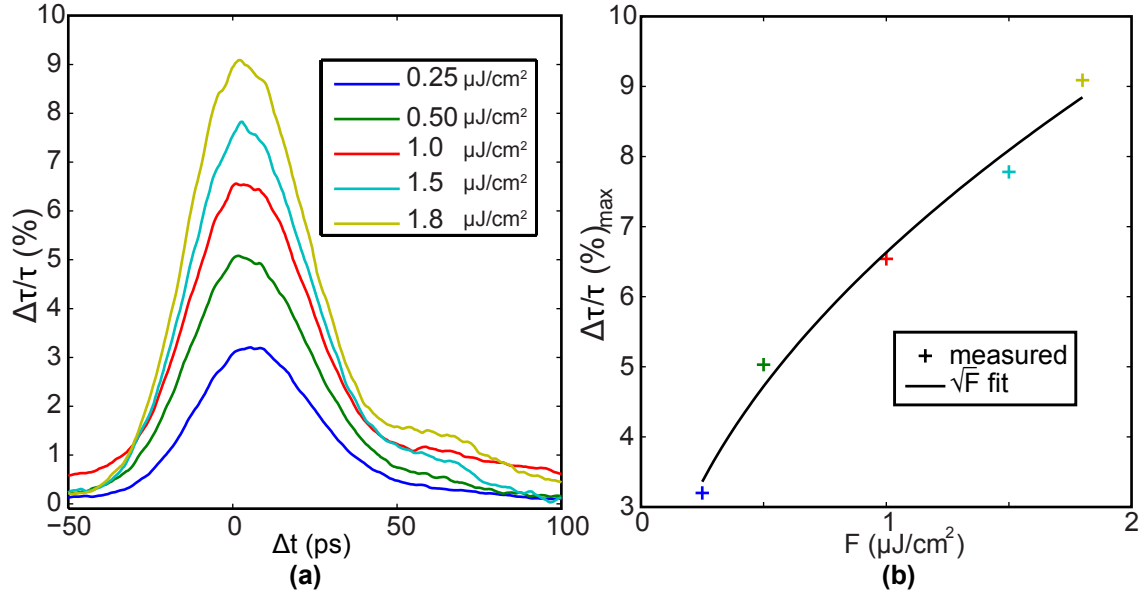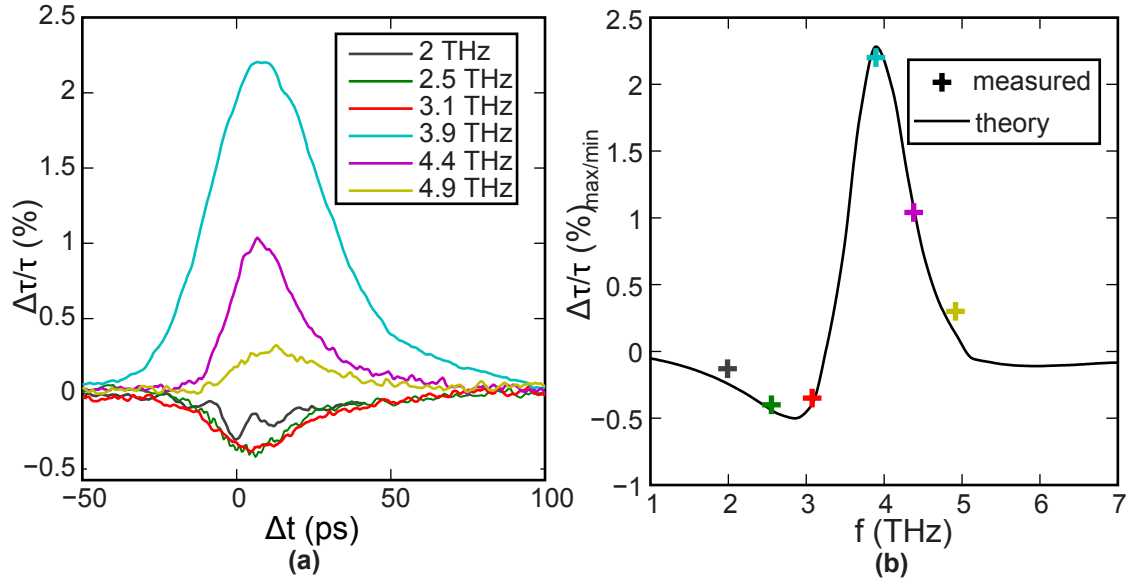
Figure 3.8: (a) Measured relative change in transmission of the probe signal for different pump/probe frequency as a function of pump-probe time delay Δt. (b) Measured peaks of relative transmission change as a function of pump/probe frequency. The black curve shows the calculated value from the nonlinear thermal model.

3.4 Nonlinear Plasmonics Response in Higher Quality Graphene

The thermal model predicts that even greater resonant enhancement of the nonlinear response can be expected in high-mobility graphene. Fig. 3.9 presents a calculation of how the observed nonlinearity would be further enhanced by employing higher quality graphene nanoribbons with a realistic mobility of 25,100 $cm^2V^{-1}s^{-1}$ [94]. The calculated power transmission is shown as a function of frequency (in the vertical direction) and time (in the horizontal direction), assuming an input fluence of 1.27 $\mu J/cm^2$. The upper horizontal plot shows the calculated pump-induced change in transmission at the equilibrium plasmon resonance frequency (marked by the horizontal white line), showing a nonlinear response in the order of unity. The right vertical plot in Fig. 3.9 shows the calculated transmission spectrum before and during the pump pulse (marked by the vertical white lines), illustrating the nature of plasmonic enhancement in the nonlinearity. The resonant absorption causes a significant increase in the carrier temperature, which leads to: (i) a broadening of the the plasmon linewidth caused by an increased carrier scattering (ii) a corresponding weakenening of the the plasmon resonance and (iii) a red-shift of the plasmon resonance. While the first two effects also occur for traditional Drude absorption in graphene, albeit a lower frequencies, the third is unique to plasmon resonances and only occurs in patterned graphene structures. For the experimental conditions considered here, all three effects contribute similarly to the observed response. For high quality graphene, as shown in the right panel of Fig. 3.9, red-shift of plasmon frequency has the most substantial impact on transmission.
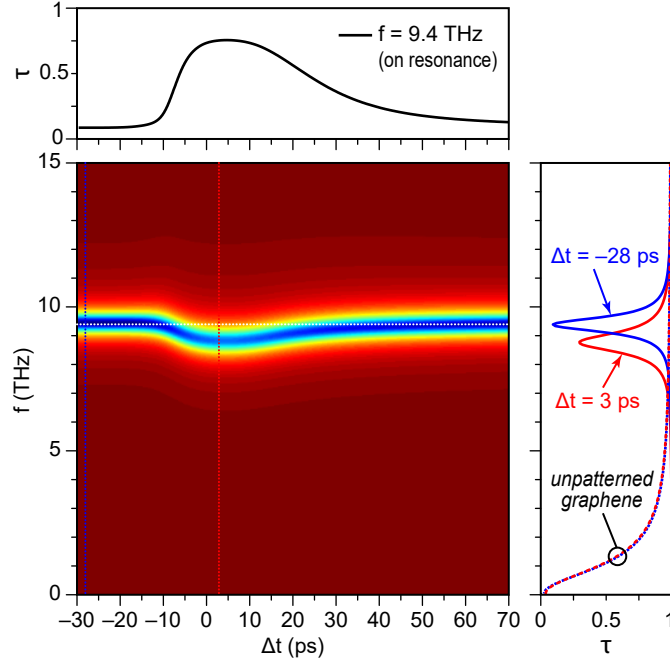
Figure 3.9: Numerically predicted change in transmission as a function of frequency f and time Δt, calculated assuming a higher graphene mobility of $25,100 \, \mathrm{cm^2 V^{-1} s^{-1}}$. The pump pulse causes a transient red-shift and broadening of the plasmon resonance, as shown by the two vertical sections plotted on the right. The dashed curves indicated in the right panel show the calculated Drude response for an unpatterned graphene sheet, which shows no plasmon resonance, and very little pump-induced change in transmission. A signal tuned to the resonant frequency would experience a corresponding transient increase in transmission, as shown in the horizontal section plotted on the top.

3.5 Conclusion

To conclude, the temperature dependent absorption, cooling, and scattering of hot electrons in graphene causes a nonlinear response to terahertz waves. Using terahertz pump-probe measurements, we show that when graphene is patterned into sub-wavelength structures that exhibit a plasmon resonance, this nonlinearity is greatly enhanced at the resonant frequency. This enhanced nonlinearity is caused by a stronger on-resonance absorption, followed by a spectral red-shift and broadening of the plasmon resonance with electron temperature.

We provide a thermal model that explains the observed nonlinear enhancement, and sheds light on the dominant cooling and scattering mechanisms for hot electrons collectively excited in a graphene plasmon. The frequency-dependence measurements on QFSBL-G confirms the nonlinear red-shift of plasmon resonance predicted by the nonlinear thermal model.

The theory predicts that in higher-mobility graphene the nonlinearity in transmission could approach unity, enabling high-speed terahertz-induced switching or modulation.

Chapter 4: Continous-wave Photomixing Spectroscopy of Graphene Thermal Relaxation

4.1 Overview

Like most conductive materials, when graphene is illuminated with light, its free electrons heat up. However, unlike most materials, hot electrons in graphene interact weakly with the carbon lattice and can produce a measurable voltage through the Seebeck effect. The speed and sensitivity of this effect is related to the physical cooling processes occurring in graphene, which are governed by scattering by phonons and spatial disorder. Recent theoretical studies have predicted that the role of disorder will depend on the carrier concentration, which in graphene can be electrically tuned. Until now, there had been no conclusive experimental demonstration of this effect.

Prior to this work, supercollision cooling was thought to be the dominant electron-phonon relaxation process over a wide range of temperatures and carrier densities [32, 95]. Evidence for conventional momentum-conserving cooling (which is linear with temperature) has been observed only at low temperatures in high-quality graphene [33]. In experimental measurements, the cooling process is inferred

from how the photoresponse depends on temperature, power, or time for either pulsed or continuous-wave illumination. Time-domain methods that are used to study thermal relaxation dynamics typically employ intense optical pulses, which significantly disturb the electron temperature, and can in some cases excite higher energy optical phonons in addition to acoustic phonons [32, 85, 92, 96]. Moreover, as we show here, the factors that govern the power dependence of the photothermal response can be different from those that determine the cooling rate. It has been shown that, uniquely in graphene, the relative strength of the two competing cooling channels can be controlled by the carrier concentration [31, 33, 37].

Here we employ a new nonlinear photomixing method to simultaneously quantify the nonlinearity in the photoresponse and the carrier-density dependence of electron cooling in graphene. This method easily distinguishes between sub-linear and super-linear power dependence, which indicate supercollision cooling and conventional cooling, respectively. Our measurements show that while supercollision dominates the nonlinear response near the charge neutral point, at higher carrier densities, conventional cooling channel is the dominant process. Furthermore, we show that when two detuned near-IR lasers co-illuminate the graphene, the resulting DC photovoltage depends upon their heterodyne difference frequency. This enables direct measurement of the electron cooling rate in the frequency domain with orders of magnitude weaker optical excitation (smaller temperature rise) than traditional time-domain methods, by simply tuning the wavelength of one of the continuous-wave lasers [97].

4.2 Photomixing Experimental Setup

Fig. 4.1a depicts the heterodyne photomixing setup used here to characterize the photothermal response of graphene. Two fiber-coupled continuous-wave near-IR lasers, one wavelength-tunable ($\lambda_1 = 1540$–1565 nm) and one fixed-wavelength ($\lambda_2 = 1545$ nm), were amplified, spatially combined, polarized, and focused using an aspheric lens to a 3 μm spot on the graphene channel. The position of focused beam was chosen to maximize the photovoltage, which occurs when the beam is focused close to one of the contacts [98, 99]. The combined optical power illuminating the first (second) device was about 6 mW (2.1 mW), from which we estimate the total absorbed intensity to be $I = 850$ W/cm² ($I = 300$ W/cm²). The graphene photodetector device was held in a liquid helium cryostat with short working distance optical access to controllably vary the lattice temperature T_L between 10 K and room temperature. The two lasers were mechanically chopped using a twin-slot (5/7) chopping wheel at frequencies $f_1 = 500$ Hz and $f_2 = 700$ Hz. The photovoltage was synchronously detected at both f_1 and the difference $f_2 - f_1$, using a dual-reference digital lock-in amplifier (Signal Recovery 7270), which simultaneously records the photovoltages V_1 and V_Δ. The phases of the two lock-in detection channels were calibrated to produce the correct sign, relative to one another. Measurements were performed as a function of gate voltage V_G, and the optical difference frequency $\Delta\nu = \Omega/2\pi$, which was swept from -0.6 THz to $+2.5$ THz by tuning laser 1.
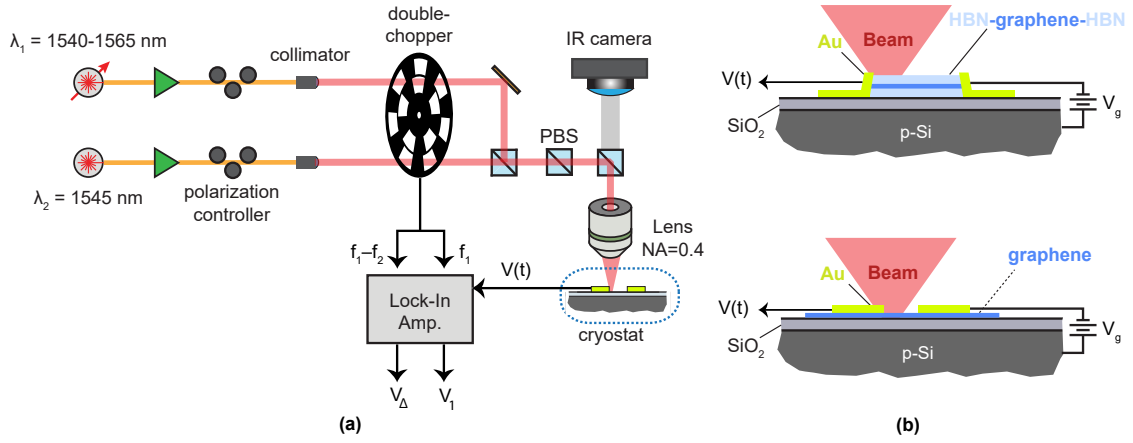
Figure 4.1: (a) Two near-IR continuous-wave beams, one with tunable wavelength, are modulated at two different frequencies f_1 and f_2, then overlapped and focused down to the graphene photodetector. The photovoltages produced by laser 1 (V_1) and the mixing of two beams (V_Δ) are detected at the modulation frequencies f_1 and $f_1 - f_2$ respectively. (b) Diagram of the HBN-encapsulated graphene (top) and exfoliated graphene (bottom) photodetector devices. The optical beams are illuminated close to one of the metal contacts, and carrier density of graphene is altered by applying an electrostatic voltage (V_g) between doped silicon substrate and graphene.

4.3 Device Fabrication and DC Electrical Characterization

To better elucidate the role of disorder, we considered two different graphene detectors shown in Fig. 4.1b: one using an edge-contacted hexagonal boron nitride encapsulated graphene channel [94, 100], and a second fabricated from an unencapsulated exfoliated flake [13].

Both devices considered here employed a doped silicon substrate ($\rho_{\text{Si}} = 100$ $\Omega\cdot$cm), with 300 nm of thermally grown SiO_2 as a gate dielectric. The substrate served as a large-area gate contact for adjusting the carrier concentration.

The HBN-encapsulated device [100] was fabricated per the method described in [94]. A piece of polypropylene carbonate (PPC) coated polydimethylsiloxane (PDMS) was first used to pick up HBN, monolayer graphene and another piece of HBN, in that order. The resulting heterostructure was then transferred to the aforementioned SiO_2 substrate, where electron beam lithography (EBL) was used to define a hydrogen silsesquioxane (HSQ) hard mask on poly(methy methacrylate) (PMMA). The surrounding areas were then etched in CHF_3 plasma to shape the device channel and expose the graphene edge. Afterwards, HSQ was lifted off and EBL was used again to define the contact leads and pads using PMMA, and 1.5 nm/20 nm/50 nm Cr/Pd/Au was e-beam evaporated and lifted off for edge contact. The HBN-encapsulated graphene channel length was 7 μm and width 0.7 μm .

For the second device, a single layer of graphene was mechanically exfoliated from bulk graphite and transferred directly to the SiO_2/Si substrate. The exfoliated graphene exhibits a mobility about $\mu = 5,000$ cm^{2}V^{-1}s^{-1}, which was inferred
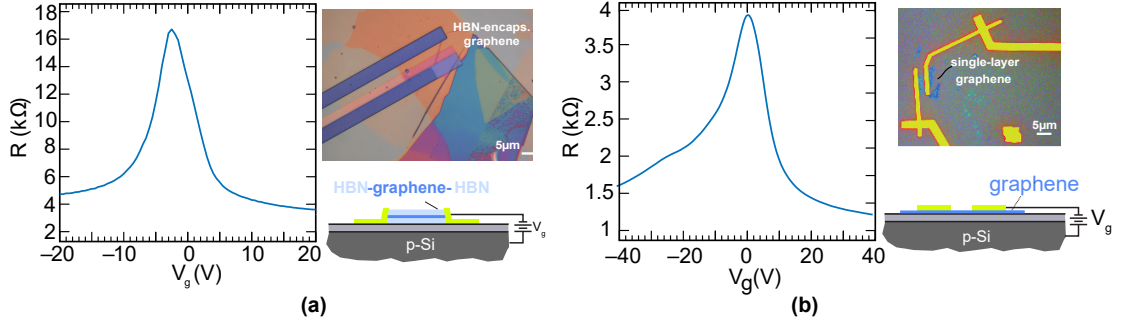
Figure 4.2: The DC resistance R as a function of the applied gate voltage V_g and the optical micrograph for (a) the HBN-encapsulated graphene device and (b) the exfoliated graphene on SiO_2 device.

from DC transport measurements. Electron-beam lithography was used to pattern a bi-layer resist comprised of methyl methacrylate (MMA) and polymethy methacrylate (PMMA). The contacts were deposited using successive angled evaporations of chromium (15 nm) and gold (30 nm), thereby providing dissimilar contacts to the opposing edges of the graphene channel. Dissimilar electrical contacts are not necessary when the optical beams are focused onto one contact, as for the measurements reported here, but this configuration also provides the thermal asymmetry needed for detection of spatially homogeneous or longer wavelength illumination. The graphene channel length was 2.5 μm and width 7 μm.

To quantify the electrical characteristics and gating behavior, we conducted unilluminated measurements of the DC resistance as a function of the gate voltage, for both the HBN-encapsulated device and the non-encapsulated device. Fig. 4.2 shows the DC measurements, along with optical micrographs showing the graphene active region, contact geometry, and cross-sectional diagram.

4.4 Nonlinear Thermal Photomixing Model

The electron temperature T in the graphene evolves according to the nonlinear differential equation [31, 34, 86]

$$\alpha T \frac{dT}{dt} + \beta_1(T - T_L) + \beta_3(T^3 - T_L^3) = I(t) \tag{4.1}$$

where T_L is the lattice temperature, αT is the specific heat of graphene carriers, the coefficients β_1 and β_3 are the rate coefficients for conventional and supercollision cooling mechanisms, respectively, and $I(t)$ is the absorbed near-infrared optical intensity.

It is assumed that the electrons are in the degenerate regime ($E_F \gg k_B T$), and that electron-electron collisions are fast enough to allow the temperature of the electron gas to be well defined [5, 34]. The hot-electron diffusion length is $\xi = (\kappa/\gamma\alpha T)^{1/2} = v_F(\gamma\Gamma)^{-1/2}$, where κ is the electronic thermal conductivity, Γ is the carrier scattering rate, and the Wiedemann-Franz law was used in the second equality. Even for the encapsulated device considered here, by estimating Γ from DC measurements in Fig. S3, we estimate that 500 nm $< \xi < 1.5$ μm which is smaller than the optical beam size employed. We therefore ignore spatial inhomogeneity in $I(t)$ and thermal diffusion of hot carriers out of the laser beam.

The three model parameters α, β_1 and β_3 appearing in (4.1) depend implicitly on the Fermi level E_F (determined by gating) and disorder mean-free path l (related to the quality of the graphene) as $\alpha = 2\pi k_B^2 E_F/(3\hbar^2 v_F^2)$, $\beta_1 = V_D^2 E_F^4 k_B/(2\pi\rho\hbar^5 v_F^6)$, $\beta_3 = \zeta(3)V_D^2 E_F k_B^3/(\pi^2\rho\hbar^4 v_F^3 s^2 l)$, where v_F is the Fermi velocity, ρ is the areal mass

density, s is the speed of sound in graphene, $\zeta(3) \simeq 1.202$ is the Riemann zeta function, and V_D is the acoustic deformation potential. We note that the substrate surface polar phonons may also play a role in hot electron cooling in graphene [101,102], and their effect on the photoresponse can be regarded as a linear cooling term in (4.1) [103]. Therefore, the coefficient β_1 might also have some contribution from the substrate phonons. At temperatures far below the Bloch-Grüneisen temperature (4.1) must be modified to include a cooling term proportional to T^4 [86]. We estimate that even at the lowest temperatures and carrier concentrations experimentally considered here ($T = 25$ K, $E_F \sim 60$ meV), the Bloch-Grüneisen temperature matches or exceeds the measurement temperature.

For the two-laser illumination shown in Fig. 4.1a, the absorbed intensity is $I(t) = I_1 + I_2 + 2\sqrt{I_1 I_2} \cos \Omega t$, where I_1 and I_2 represent the absorbed intensities of lasers 1 and 2 respectively and $\Omega \equiv 2\pi c(\lambda_2^{-1} - \lambda_1^{-1})$ is their heterodyne difference frequency. The resulting photothermoelectric voltage V produced by the Seebeck effect is then related to the electron temperature by $V = rT(T - T_L)$, where rT is the Seebeck coefficient of graphene [28, 104]. This nonlinear relationship between temperature and photovoltage could be generalized to include a nonlinearity in the Seebeck coefficient [105], but the temperature- and power-dependence of the observed nonlinearity indicate that this effect is small in comparison to the nonlinearity in cooling. Although other photoresponse mechanisms, such as photoelectric effect [106], might also contribute to the graphene photoresponse, a photo-thermo-electric model can adequately describe the photoresponse at the graphene-metal interface [13, 38, 107].

Equation (4.1) can be solved using a power series expansion (Supplementary Material), and resulting DC photovoltage is found to be

$$V(I_1, I_2) = a_1(I_1 + I_2) + a_2(I_1^2 + I_2^2) - a_3(I_1^3 + I_2^3) \quad \ldots$$

$$+ 2a_2 I_1 I_2 \left[1 + \frac{\gamma^2}{\Omega^2 + \gamma^2} \right] - 3a_3 I_1 I_2 (I_1 + I_2) \left[1 + \frac{2\gamma^2}{\Omega^2 + \gamma^2} \right] \tag{4.2}$$

where $\gamma \equiv (\beta_1 + 3\beta_3 T_L^2)/\alpha T_L$ is the linearized cooling rate from both mechanisms. The coefficients a_1, a_2 and a_3 are given by

$$a_1 \equiv \frac{r}{\alpha\gamma}, \quad a_2 \equiv \frac{r\beta_1}{(\alpha\gamma T_L)^3}, \quad a_3 \equiv \frac{3r\beta_3^2}{T_L^2 \alpha^5 \gamma^5} \tag{4.3}$$

The final two terms in (4.2) which contain the factor $I_1 I_2$, represent a nonlinear interaction of the two beams, which occurs only when both beams are present. In order to sensitively detect only these mixing products, we employ a double-modulation configuration in which laser 1 is mechanically chopped at a frequency f_1, laser 2 is chopped at f_2, and the photovoltage V is synchronously detected using a lock-in amplifier at the chopping difference frequency $\Delta f \equiv f_1 - f_2$ (not to be confused with the heterodyne difference frequency). The resulting photovoltage $V_\Delta \equiv V(I_1, I_2) - V(I_1, 0) - V(0, I_2)$ can be positive or negative, depending on the nonlinearity in the photothermal response. We also simultaneously measure the Fourier component at f_1, denoted $V_1 \equiv V(I_1, 0)$, which gives the photovoltage produced by laser 1 alone.

By simply comparing the magnitude of the two terms that compose the linearized cooling rate γ, one can determine a condition for which process makes the largest contribution to the cooling rate. For nearly all of the experimental cases considered here and reported elsewhere, the cooling rate is largely limited by the

supercollision term. (4.3) reveals that despite this, the photoresponse can be either super-linear or sub-linear in intensity, depending on the carrier density and graphene quality. As explained below, neither cooling effect can be ignored when analyzing the nonlinearity of the response.

When the heterodyne frequency exceeds the cooling rate ($\Omega \gg \gamma$), (4.2) simplifies to $V(I) = a_1 I + a_2 I^2 - a_3 I^3$, where $I \equiv I_1 + I_2$ is the total absorbed optical intensity. The quadratic and cubic terms have opposite sign, and therefore describe super-linear or sub-linear dependence on the optical intensity. From (4.3), one sees that the super-linear coefficient is proportional to β_1, which we associate with momentum-conserving cooling, while the sub-linear coefficient is proportional to β_3, which arises from supercollision cooling.

4.5 Measurement Results

4.5.1 Nonlinear Signal vs Carrier Density

Fig. 4.2a plots V_1 (black) and V_Δ (green) as a function of the gate voltage for the HBN-encapsulated device. These measurements were performed with $\Omega/2\pi = 2.5$ THz, which is much faster than the expected cooling rate at room-temperature. The sign of the photothermal voltage V_1 depends on the gate voltage, as expected from the photothermoelectric effect [13,28,29]. For carrier densities near the charge-neutral point (CNP), V_1 and V_Δ have opposite sign (as indicated by the blue shading), revealing a sub-linear power dependence, characteristic of supercollision cooling [32,38]. In this regime the Fermi surface is small, and the allowed phonon energy

space for momentum-conserving collision is strongly constrained, thereby suppressing conventional electron-phonon cooling [31, 37]. At higher carrier densities, the behavior changes to super-linear (red shading), indicating that conventional cooling becomes dominant. Fig. 4.2b plots the single-beam photovoltage as a function of the incident optical power, confirming the sub- and super-linear behavior, respectively. Fig. 4.2c illustrates the two cooling mechanisms schematically in k-space, along with the predicted sublinear and superlinear power dependence. The transitions outside of the Dirac cone represent supercollision cooling, in which the spatial disorder in the graphene compensates for the electron-phonon momentum mismatch.

The threshold between these two nonlinear regimes can be approximated by equating the opposing terms in V_Δ, which gives,

$$2a_2 \gtrless 3a_3 I \tag{4.4}$$

where the upper and lower inequalities describe the conditions under which conventional cooling or supercollision cooling prevails in the nonlinear response, respectively. The relative importance of the two competing cooling channels depends on temperature, intensity, the carrier concentration (Fermi level), and indirectly on the material quality, which is related to the disorder mean-free-path l. Even though the linearized cooling rate γ is limited by supercollision cooling, both effects are evident in the nonlinear response reported here.

Fig. 4.4 present results of similar measurement performed on lower-mobility exfoliated graphene on SiO_2. In this device, the diffusion length is estimated to be only 500 nm, which is about one order of magnitude smaller than for the encapsu-

Figure 4.3: (a) Single-laser photovoltage (V_1), and nonlinear photomixing signal (V_Δ) measured vs. the applied gate voltage V_g. V_{CNP} denotes the charge neutral point. Red ($V_1 V_\Delta > 0$) and blue ($V_1 V_\Delta < 0$) regions indicate the conditions where super- and sub-linear power dependence is observed. (b) Measured photovoltage V_1 of a single laser vs. incident optical power at two different gate voltages, showing sublinear and superlinear behavior. (c) Calculated photothermoelectric voltage (in arbitrary units) vs. input optical power for the case of $\beta_1 = 0$ (blue) and $\beta_3 = 0$ (red), illustrating the sublinear and superlinear behavior, respectively. Inset: energy diagram illustrating the two different cooling mechanisms.

lated device. Because of this difference, the majority of the photoresponse in this device originates from the Fermi-level pinned region near the contact, where the carrier concentration is not as easily controlled by the applied gate voltage. For positive gate voltages, Fermi level pinning produces a pn junction and charge-neutral region near the contact [74, 108], which contributes to the observed sub-linear response. Otherwise, the response is qualitatively similar to that of the HBN-encapsulated device, and we observe a similar expected transition from supercollision cooling to conventional cooling under negative gate bias.

From the data in Fig. 4.4, the sublinear-superlinear transition occurs at $V_g = -6$ V where the estimated Fermi level is $E_F = 80$ meV. Assuming a disorder mean-free-path of $l = 40$ nm (which was independently determined from DC electrical measurements), we can use (4.4) to determine the ratio of the two rate coefficients, $\beta_1/\beta_3 = 5300$ K^2. At room temperature, the supercollision contribution to the cooling rate γ is nearly 50$\times$ larger than the contribution from conventional cooling. Despite this, both effects have non-negligible role in the nonlinearity of the photoresponse, and their relative significance depends on the carrier density.

4.5.2   Nonlinear Signal vs Difference Frequency

When the heterodyne difference frequency Ω is comparable to or smaller than the cooling rate γ, the electron temperature can follow the interferometric beating of the two lasers, which produces a larger photothermal voltage than when the lasers are widely detuned. The final two terms in (4.2) reveal that the nonlinear mixing
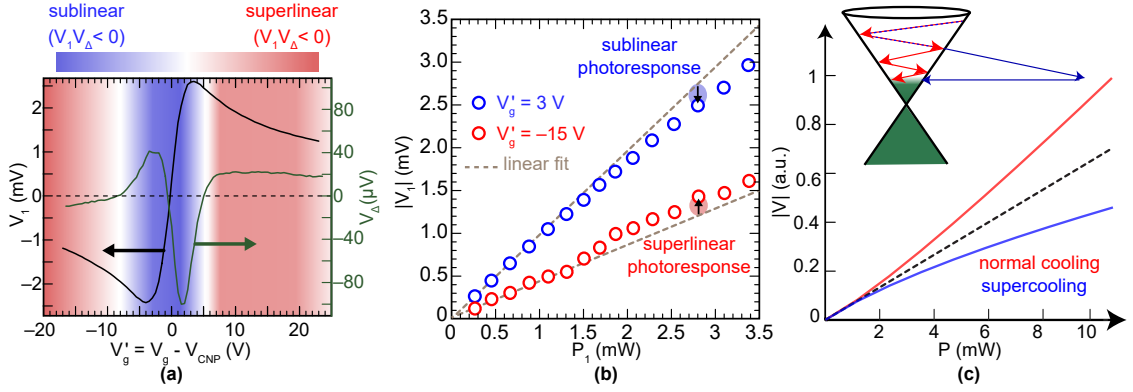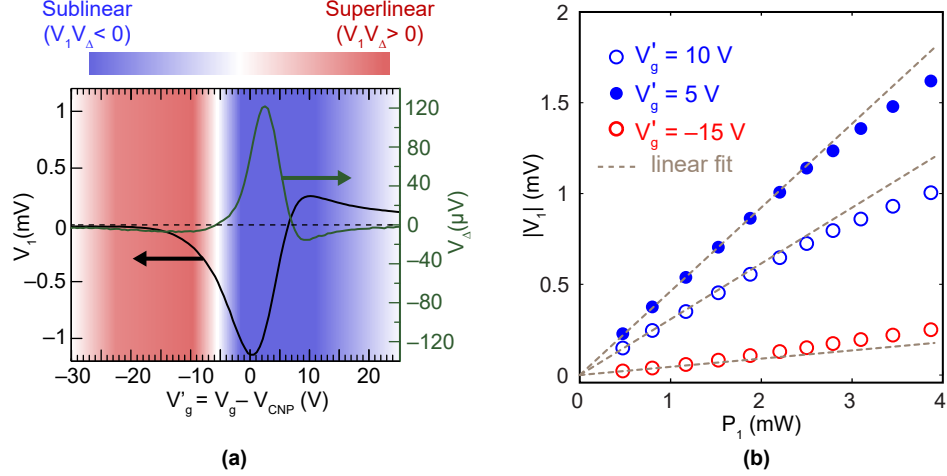
Figure 4.4: (a) Single-laser photovoltage (V_1), and nonlinear photomixing signal (V_Δ) measured vs. the gate voltage V_g, for the exfoliated graphene on SiO_2. (b) Measured photovoltage $|V_1|$ vs. optical input power, showing clearly the sub-linear and super-linear behaviors.

signal V_Δ exhibits a Lorentzian dependence on the heterodyne difference frequency Ω, with a spectral width that is proportional to the cooling rate γ. As before, the double-chopping configuration allows for sensitive detection of this heterodyne photomixing signal.

Fig. 4.5a plots the measured photovoltage V_Δ as a function of the gate voltage and heterodyne difference frequency, for the non-encapsulated graphene detector. In addition to the expected gate-voltage dependence discussed previously, the photoresponse exhibits distinct spectral peak around $\Omega = 0$. Fig. 4.5b shows the photomixing spectrum at a fixed gate voltage, along with the best-fit Lorentzian curve. From the linewidth, we estimate a cooling time of $\gamma^{-1} = 1.42$ ps, which is consistent with the time-domain pulse coincidence measurements [13, 109] reported for similar
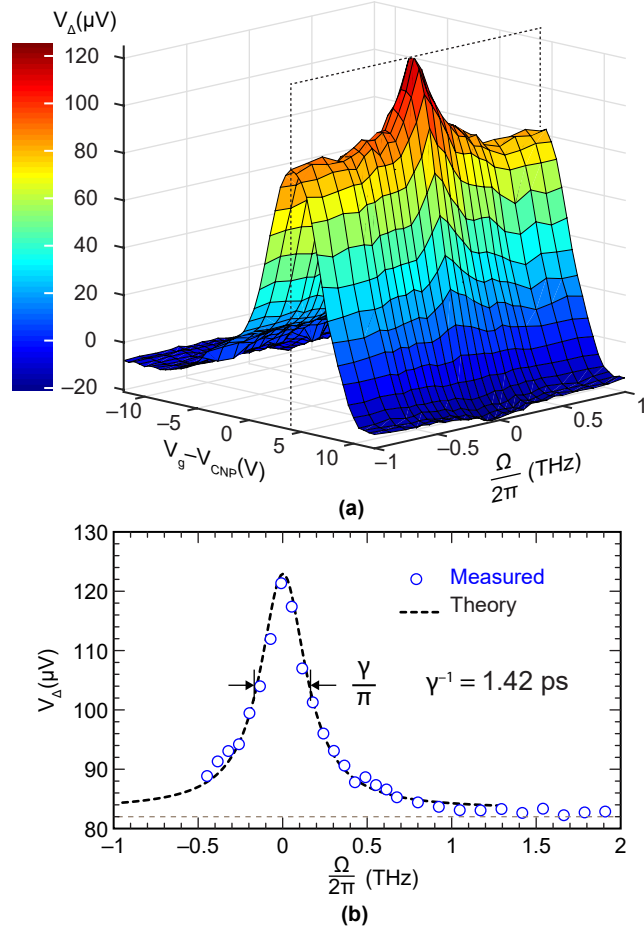
Figure 4.5: (a) The nonlinear photomixing signal (V_Δ) as a function of their difference frequency (Ω) and gate voltage (V_g). At each gate voltage, V_Δ exhibits a Lorentzian-shaped dependence on the heterodyne difference frequency Ω. (b) V_Δ vs Ω for $V_g = 4$ V. The dashed curve is the theoretical calculation of the photomixing voltage based on a photothermoelectric effect. From the Lorentzian fit, the hot electron cooling time is estimated to be $\gamma^{-1} = 1.42$ ps.

devices.

4.5.3 Temperature Dependence Measurements

In order to confirm the thermal model for the photomixing, we repeated the heterodyne spectral measurements at temperatures from room temperature down to 25 K for the exfoliated sample on SiO_2 near the charge neutral point. As shown in Fig. 4.6a, in all cases the photomixing signal exhibits a Lorentzian spectral dependence, but with a spectral width that decreases with temperature, as expected. The solid blue curve in Fig. 4.6b shows a fit to the linearized cooling rate, based on the model presented here.

For the data points above $T_L = 80K$, and for conditions at the charge neutral point, the assumption of $E_F \gg k_B T$ (degenerate regime) is no longer valid, which requires a modification of the cooling rate. We therefore excluded these points when fitting the blue curve. However, when the parameters from the low-temperature fit were incorporated into the modified thermal model, it correctly predicts the observed high-temperature asymptotic behavior, indicated by the red curve, with no additional free parameters. Below we briefly explain the theory fit in Fig. 4.6.

4.5.3.1 Linear Cooling Rate close to the Dirac Point

The thermal model presented in the manuscript ignores the fact that when the graphene is gated at the charge neutral point, the carriers are no longer degenerate, and under these conditions, the specific heat (αT) and conventional cooling
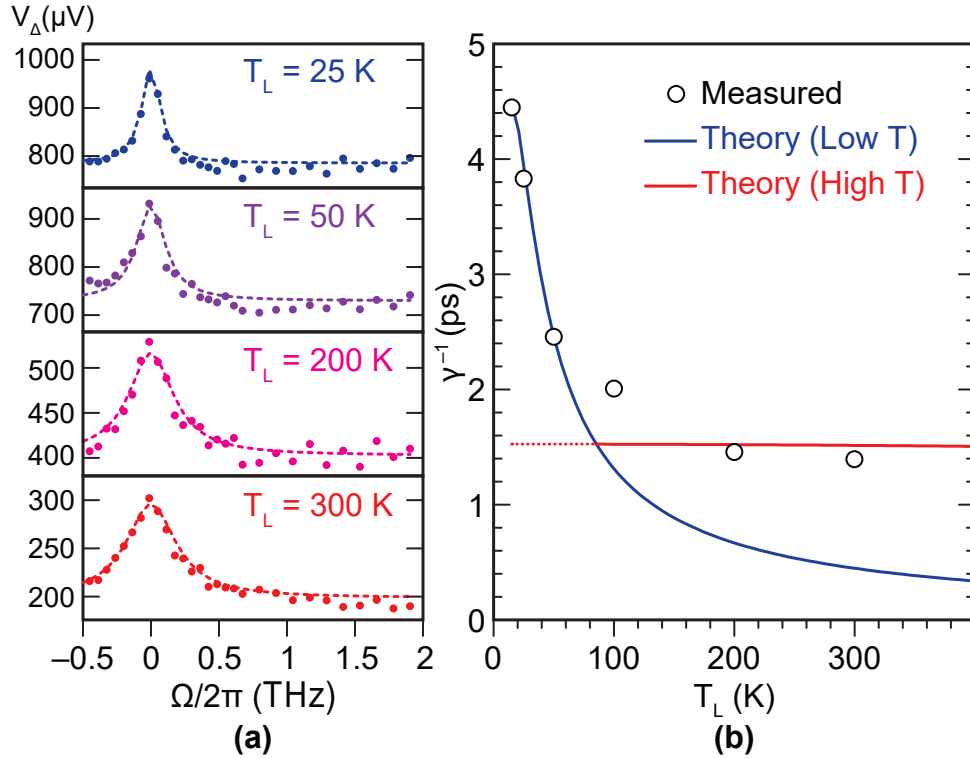
Figure 4.6: **Temperature dependence of cooling rate.** (a) The two-beam mixing signal as a function of difference frequency measured close to the charge neutral point (sub-linear power dependence regime) at different temperatures for the exfoliated sample on SiO_2. The dashed curves are Lorentzian fits. (b) Black circles are the extracted hot electron cooling time constant $\tau \equiv \gamma^{-1}$ from Lorentzian fits in part (a). The blue/red curve is the theory fit for low/high temperatures.

coefficient (β_1) must be modified to [39, 86, 110]:

$$\alpha T \rightarrow \alpha_2 T^2, \quad \text{where} \quad \alpha_2 \equiv 18\zeta(3)k_B^3/\pi\hbar^2 V_F^2 \tag{4.5}$$

$$\beta_1 \rightarrow \beta_5 T^4, \quad \text{where} \quad \beta_5 \equiv 7\pi^3 k_B^5 V_D^2/30\rho\hbar^5 v_F^6 \tag{4.6}$$

and the nonlinear thermal equation under these conditions becomes

$$\alpha_2 T^2 \frac{dT}{dt} + \beta_5 T^4(T - T_L) + \beta_3(T^3 - T_L^3) = I(t) \tag{4.7}$$

If (4.7) is linearized about the lattice temperature, one obtains

$$\alpha_2 T_L^2 \frac{dx}{dt} + (\beta_5 T_L^4 + \beta_3 T_L^2)x = I(t) \tag{4.8}$$

where $x = T - T_L$ is the photoinduced change in electron temperature relative to the lattice. The linearized cooling rate is then

$$\gamma' = \frac{\beta_5 T_L^2 + 3\beta_3}{\alpha_2} \tag{4.9}$$

which is shown by the red curve in Fig. 4.6.

We expect that at low temperatures, $k_b T$ will be much smaller than E_F^*, the charge-puddle-limited Fermi level, in which case the cooling can instead be accurately described by γ. The boundary between the two regimes can be estimated by equating γ and γ' (4.9), which, for the parameters considered in Fig. 4.6 indicates that γ should only be applicable for $T_L < 80$ K. This condition is represented by the intersection between the blue and red curves in Fig. 4.6.

When the parameters determined from the low-temperature fit to the cooling rate γ are used in (4.9), with no additional free parameters, we correctly predict the observed cooling rate above 80 K, which further supports the model.

4.6   Discussions

This nonlinear heterodyne photovoltage spectroscopy method has two important advantages over the traditional time-domain measurement using pulse coincidence [13, 32, 109]: (i) The frequency range and resolution is limited only by the tuning range and resolution of the laser, while in time-domain measurements the response is limited by the optical pulsewidth and repetition period. (ii) Continuous-wave illumination produces a far smaller thermal stimulus to the graphene electrons than intense ultrafast pulses, thereby allowing measurement of the temporal dynamics and nonlinearity of photodetection under low photothermal excitation for which the electron temperature is near the lattice temperature.

The model and measurements described here show that there are two competing cooling channels for hot electrons in graphene, and (4.4) describes the relative importance of each in the nonlinear response. In time-domain experiments reported elsewhere, the instantaneous absorbed intensity is orders of magnitude higher that the continuous-wave illumination considered here, in which case (4.4) predicts that supercollision cooling is the dominant contribution to the nonlinearity at all practically attainable doping concentrations. Moreover non-encapsulated graphene samples have a much smaller disorder mean-free-path l, which further contributes to the relative importance of supercollision cooling over conventional momentum-conserving cooling. In these cases, the photothermal response is often adequately described by supercollision cooling alone, for a wide range of carrier densities and temperatures [38, 84, 95]. For continuous-wave measurements on encapsu-

lated devices, (4.4) also predicts that at sufficiently low temperatures, conventional cooling will prevail, consistent with temperature-dependent measurements reported recently [33].

4.7   Conclusion

We show that nonlinearity in the photothermoelectric effect causes photomixing when graphene is illuminated by near-infrared beams, and we describe a new heterodyne spectroscopy method that accurately measures this nonlinearity in the frequency domain. Exceedingly small nonlinearities in the photoresponse can be probed using continuous-wave illumination, which accurately elucidates the physical mechanisms behind the nonlinearity and cooling. In particular, the measurements reveal the role that disorder plays in the cooling of hot electrons, and the interplay of different cooling channels at different carrier concentrations. The method permits direct measurement of the cooling rate in graphene using swept laser spectroscopy, which offers several advantages over pump-probe or pulse-coincidence measurements. The work also implies that nonlinear photomixing in graphene is very promising for the development of new optical/THz photomixing devices.

Chapter 5:   Time-resolved Optical Study of Carrier Dynamics in the Weyl Semimetal TaAs

5.1   Overview

Tantalum arsenide (TaAs) is the first Weyl semimetal discovered, and it can be regarded as the three-dimensional version of graphene that has a crystal structure without inversion symmetry. Owing to the nontrivial topology of electronic wave functions, Weyl semimetals shows new physical properties related to the Berry curvature associated with the Weyl nodes [42–44, 111]. Unlike many other Weyl semimetals, the Fermi energy of TaAs lies in an energy regime where two topologically nontrivial pockets with opposite chirality exist at Fermi surface [112, 113]. Therefore, many electronic and optical properties that are sensitive to dynamics of electrons at the Fermi surface can exhibit topological behavior [45–47, 112, 114]. This makes TaAs a very attractive material to investigate for various optical/optoelectronic applications. For this purpose, it is essential to know how carriers interact with each other and lose their energy to lattice in TaAs. To date, there has been no time-resolved study of carriers dynamics and related relaxation time constants in Weyl semimetals.

Here we present the first ultrafast optical study of carriers dynamics in a Weyl semimetal. We employ optical reflectance pump-probe measurements at variety of temperatures to study carriers dynamics of the broken-inversion-symmetry Weyl semimetal Tantalum arsenide (TaAs). Our measurements reveal different time constants that describe relaxation of hot carriers to TaAs lattice. We attribute the fast time constant ($\approx$ 2 ps at 10 K) to relaxation of hot electrons to optical phonons, and the slower one ($\approx$ 200 ps at 10 K) to acoustic phonons. Our temperature dependence measurements reveal that both relaxation processes become slower at higher temperatures. We also present a qualitative thermodynamic model based on thermalized carriers to explain the observed reflectance pump-probe results.

5.2 Optical Conductivity of a 3D Dirac Semimetal

We first present semi-classical formulas of conductivity for a three-dimensional semimetal with a Dirac cone energy dispersion [43, 115, 116].

5.2.1 Interband Conductivity

The inertband optical conductivity of a semimetal with a single Dirac cone and chemical potential μ_0 at zero temperature can be approximated as

$$\sigma_{inter}(\omega; T = 0) = \frac{e^2}{24\pi\hbar v_F}\omega\, \mathrm{H}(\omega - 2|\mu_c|/\hbar) \tag{5.1}$$

where $H(x)$ is Heaviside step function, and v_F is the Fermi velocity. At finite temperature T, (5.1) is modified to [116]

$$\sigma_{inter}(\omega) = \frac{e^2}{24\pi\hbar^2 v_F}\omega\frac{\sinh(\hbar\omega/2k_B T)}{\cosh(\mu_c(T)/k_B T) + \cosh(\hbar\omega/2k_B T)} \tag{5.2}$$

where $\mu_c(T)$ is the chemical potential at temperature T. In high temperature limit where $k_B T \gg \mu_c(T)$, (5.2) can be simplified to

$$\sigma_{inter}(\omega) = \frac{e^2}{24\pi\hbar v_F}\omega \tanh(\frac{\hbar\omega}{2k_B T})$$

(5.3)

which is a result similar to the 2D Dirac case [53, 117].

5.2.2   Intraband Conductivity

The intraband optical conductivity at zero temperature is approximated by a Drude formula

$$\sigma_{intra}(\omega; T = 0) = \frac{e^2}{3\pi^2\hbar^3 v_F}\frac{\mu_0^2}{\Gamma - i\omega}$$

(5.4)

where Γ is the scattering rate of carriers. At finite temperature T, we can approximate the intraband conductivity by a temperature-dependent Drude model,

$$\sigma_{intra}(\omega; T) = \frac{e^2}{3\pi^2\hbar^3 v_F}\frac{\mu_c^2(T) + (\pi^2 k_B^2/3)T^2}{\Gamma(T) - i\omega}$$

(5.5)

Assuming conservation of particle number, the chemical potential at temperature T is calculated as [116]

$$\mu_c(T) \approx \mu_0 - \frac{\pi^2 k_B^2}{3\mu_0}T^2 \qquad\qquad k_B T \ll \mu_0$$

(5.6)

$$\mu_c(T) \approx \frac{\mu_0^3}{\pi^2 k_B^2}\frac{1}{T^2} \qquad\qquad k_B T \gg \mu_0$$

(5.7)

The temperature dependence of the scattering rate $\Gamma(T)$ depends on the physical mechanism behind carrier scattering, which can be through phonons, short- and

90

long-range Coulomb disorders [115]. The relative importance and strength of these processes depend on the material type and quality.

We calculate Drude weight ($\equiv D(T)$) from (5.5)-(5.7) as

$$D(T) \approx \frac{e^2}{3\pi\hbar^3 v_F}[\mu_0^2 - (\pi^2 k_B^2/3)T^2] \qquad k_B T \ll \mu_0 \qquad (5.8)$$

$$D(T) \approx \frac{e^2}{3\pi\hbar^3 v_F}(\pi^2 k_B^2/3)T^2 \qquad k_B T \gg \mu_0 \qquad (5.9)$$

5.2.3 Comparison to a 2D Dirac semimetal

We now compare the conductivity formulas presented in previous section to graphene conductivity discussed in chapter 2. There are two clear differences between conductivity of 3D and 2D Dirac systems:

(I) The interband conductivity of a 3D Dirac semimetal is linearly proportional to frequency (5.1), whereas in 2D materials, it is frequency independent.

(II) The temperature dependence of Drude weight at high temperatures is quadratic in T (5.9), while in 2D, it is linear.

Linear optical reflection spectroscopy of 3D Dirac/Weyl semimetals have confirmed these effects [118–120].

5.2.4 Conductivity of Multiple Dirac/Weyl bands

Finally, we explain briefly how the semi-classical equations for the conductivity of a semimetal with single Dirac cone presented previously can be modified to the case of a semimetal with N Dirac/Weyl cones. The optical conductivity is the

summation of contributions from each band [116].

In time-reversal-broken Weyl semimetals, in the absence of an applied magnetic field, the chemical potential of all Weyl bands are equal. Therefore, the total optical conductivity is simply N times the contribution from a single Weyl band.

In case of inversion-symmetry-broken Weyl systems, there can be an energy offset between different Weyl pairs [44, 116], and as a result, the effective Fermi level of carriers in each Weyl band (energy difference between Fermi level and the Weyl node) can be different. This has to be taken into account when adding up contributions of Weyl bands to the total conductivity.

5.3   Introduction to the Weyl Semimetal TaAs

5.3.1   Crystal Properties and Band Structure

As depicted in Fig. 5.1a, Tantalum arsenide (TaAs) possesses a non-centrosymmetric tetragonal lattice structure. In the right panel of Fig. 5.1a, we show the calculated bulk band structure of TaAs in the absence of spin-orbit coupling, adopted from [48]. The blue rectangle marks four crossings of spin-degenerate valence and conduction bands in the Brillouin zone (BZ). By including spin-orbit coupling in the calculations, each of the four points breaks into three pairs of linearly dispersive Weyl nodes, where each pair consists of two nodes with opposite single chiral charges of ± 1 . Four pairs of these Weyl nodes (W1) are located in the $k_z = 0$ plane, while other eight pairs (W2) are at $k_z = \pm \pi/c$, adding up to 24 Weyl nodes in total for the first BZ [48–50, 111, 121].
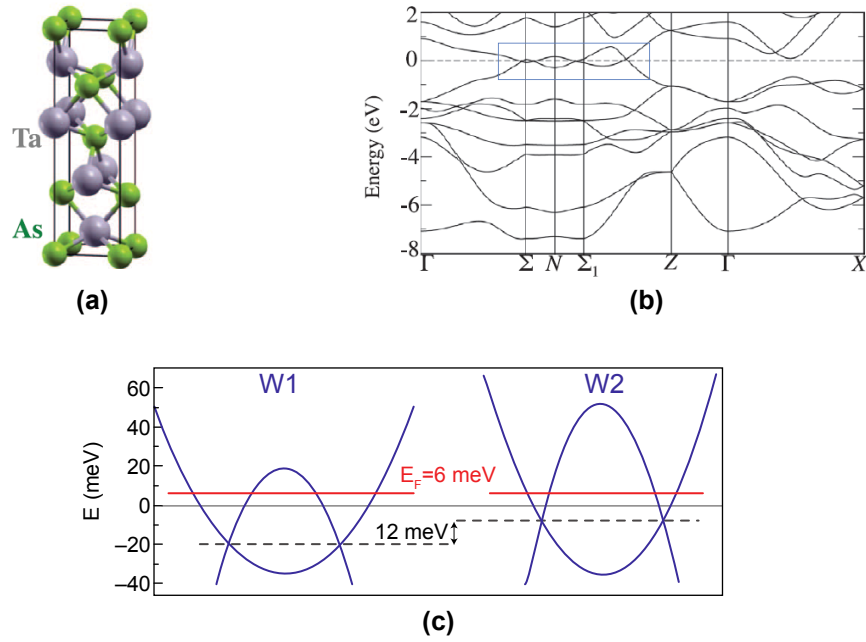
Figure 5.1: (a)Tetragonal crystal structure of TaAs, consisted of Ta and As stacks. The lattice of TaAs is non-centrosymmetric. (b) Electronic band structure of TaAs without spin-orbit coupling. The blue box marks the band-touching point. Figures were adapted from [48]. (c) Two kinds of Weyl pairs (W1 and W2) with 12 meV energy offset exist in TaAs. Gray line shows the charge neutrality, and red dashed line shows the Fermi level E_F [112].

Fig. 5.1b depicts the position of two types of Weyl pairs (W1 and W2) in TaAs with respect to each other and the Fermi energy level (red dashed line). The energy level offset between two Weyl pairs, caused by broken inversion symmetry, is $\approx$ 12 meV [112]. Due to this energy offset, there are always free carriers in the system regardless of the Fermi energy level. The W1 and W2 Weyl pairs exhbit two different carrier concentrations: As illustrated in Fig. 5.1b, the Fermi level E_F is about 26 meV/14meV above the W1/W2 Weyl pair, confirmed by quantum oscillation measurements [112]. Thus, both Weyl pairs form electron-like pockets at the Fermi surface [112, 113].

As illustrated in Fig. 5.1b, for both W1 and W2 Weyl pairs, Fermi energy is below the saddle point of Lifshiftz gap energy ($\approx$ 20 meV/50 meV for W1/W2 Weyl pairs). This leads to two topological electron pockets with opposite chirality, which is a distinctive property of TaAs compared to other discovered Weyl semimetals [112]. We note that full band structure calculations show that, in addition to the Weyl bands, there are topologically trivial bands crossing the Fermi level in TaAs, including a low energy one that forms a hole pocket at the Fermi surface [112, 113, 121].

5.3.2 Optical Properties

In this section, we discuss linear optical response of TaAs. In Fig. 5.2, we plot reflection spectrum of the (001) face of a TaAs crystal measured using standard FTIR technique. The measured reflection spectrum exhibits high values at low

frequency mainly due to the intraband absorption of free carriers in TaAs. Based on the position of the Weyl points and Fermi energy illustrated in Fig. 5.1b, for frequencies above 6.8 THz (28 meV photon energy), the interband absorption of carriers in the W2 Weyl band is expected to play a role in the optical response. For frequencies above 12.6 THz (52 meV photon energy), the interband absorption can occur in both Weyl bands of W1 and W2.

The effect of interband and intraband absorption of electrons in Weyl bands on the conductivity of TaAs can be estimated using the equations presented in section 5.2. In [118], the optical response of TaAs and its temperature dependence was measured in a wide range of frequency. In this study, authors found some unique optical properties of 3D Dirac/Weyl systems in TaAs, such as linear frequency dependence of interband conductivity and quadratic temperature dependence of Drude weight [118].

As discussed earlier, the Fermi energy, in addition to Weyl bands, crosses other (trivial) bands in TaAs [112, 121]. Xu *et al* noticed that for frequencies over ≈ 7 THz, interband transition of carriers in trivial bands contribute noticeably to TaAs optical response.

5.4   Ultrafast Pump-probe Measurements

We experimentally study carriers dynamics in TaAs using optical pump-probe techniques. The picture of TaAs crystal studied here is depicted in Fig. 5.3a. The optical measurements were done on the crystal facet with (001) orientation.
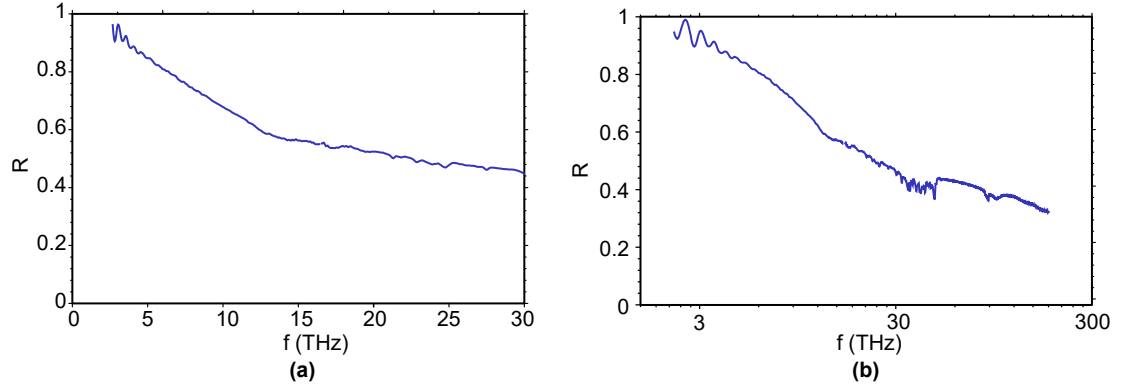
Figure 5.2: Measured reflection spectrum of (001) face of a TaAs crystal in (a) linear, (b) semi-logarithmic plot.
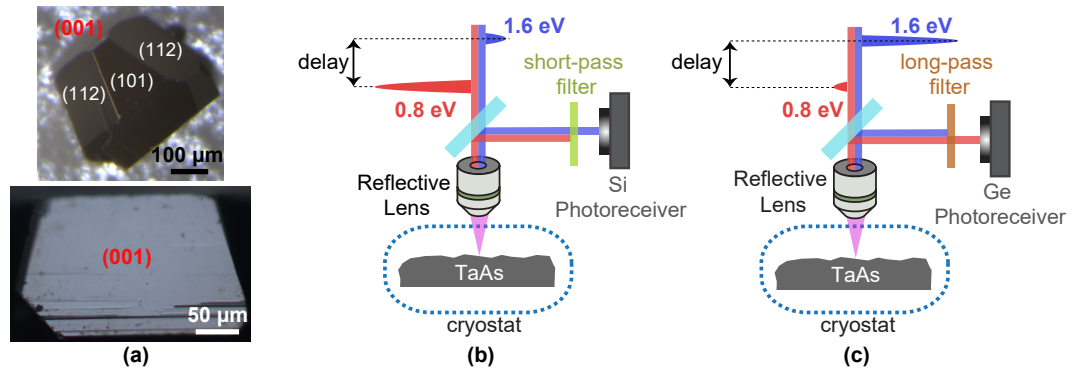

Figure 5.3: (a) TaAs crystal considered here. The crystal orientation is marked on each facet. The measurements were done on the (001) facet marked with red. An enlarged image of the crystal facet considered here is shown at the bottom. (b) 0.8-1.6 eV reflection pump-probe setup. (c) 1.6/0.8 eV reflection pump/probe setup.

The pump-probe measurements were carried out using two fiber lasers (Menlo Systems). The lasers produce approximately 100 fs wide pulses at a repetition rate of 100MHz and center wavelengths of 780 nm (1.6 eV) and 1560 nm (0.8 eV). The two lasers were electronically synchronized with a small difference in the repetition rate, allowing for large pump-probe delays (up to 10 ns) to be achieved without the use of a mechanical delay line. The two pulses were spatially overlapped and focused onto the 001 facet of the TaAs crystal using a reflective objective (WD=2.5 cm, NA=0.28), rather than a usual refractive lens, to insure that the two beams with different wavelengths focus to the same spot on the TaAs sample. The spot size of both beams at the focus are measured as FWHM≈7 μm. We employ two different pump-probe schemes to study carriers dynamics of the TaAs crystal pictured in Fig 5.3a:

(i) 0.8-1.6 eV pump-probe (Fig. 5.3b): In this configuration, the change in reflection of the 780 nm pulse induced by a strong 1560 nm pulse is measured as a function of the time delay between two pulses. The 1560 nm (0.8 eV) pump pulse is mechanically chopped at 435 Hz and has much higher fluence than the 780 nm (1.6 eV) probe. The reflected beams off of the TaAs sample are passed through a short-pass filter to block/pass pump(0.8 eV)/probe(1.6 eV). The 1.6 eV probe pulse passes the filter and is being collected at a silicon photoreceiver. The detector is connected to a lock-in amplifier that monitors the modulated pump-induced change in reflection of the 1.6 eV probe.

(ii) 1.6-0.8 eV pump-probe (Fig. 5.3c): In this scheme, we swap the pump and probe pulse: 1.6 eV pulse is the strong pump (chopped at 435 Hz) and 0.8 eV

pulse is the probe. The measurement setup similar to the ones in (i) except: a) a long-pass filter (AR-coated silicon at 1560 nm) is used to pass through the 0.8 eV probe and block the 1.6 eV pump. (b) a Silicon photoreceiver is replaced by a germanium detector that is sensitive at 1560 nm.

The photon energy of both pulses are much higher than the Fermi energy and the Lifshitz gap energy. Therefore, we don't expect to induce or probe chirality in the described pump-probe measurements. In the following, we present measurement results of the two pump-probe setups described above and discuss what information each provides about the carrier dynamics and ultrafast nonlinear optical effects in TaAs.

5.4.1   Pump(0.8 eV)-Probe(1.6 eV)

Fig. 5.4a shows the relative change in reflection of the 1.6 eV probe pulse $\Delta R/R$ as a function of time delay for a variety of 0.8 eV pump pulse peak intensities. A small instantaneous decrease in reflectivity is observed at zero pump-probe time delay followed by a change in sign and a strong positive peak in $\Delta R/R$. Both the negative minimum and positive maximum increase monotonically with the pump intensity. The pump intensity dependence of maximum and minimum are plotted in Fig. 5.7 and will be discussed further.

Unlike the ultrafast initial negative pump-probe signal, the transient increase in reflection and subsequent decay are characterized by finite time constants. In order to investigate time constants of these processes, we fit the pump-probe data
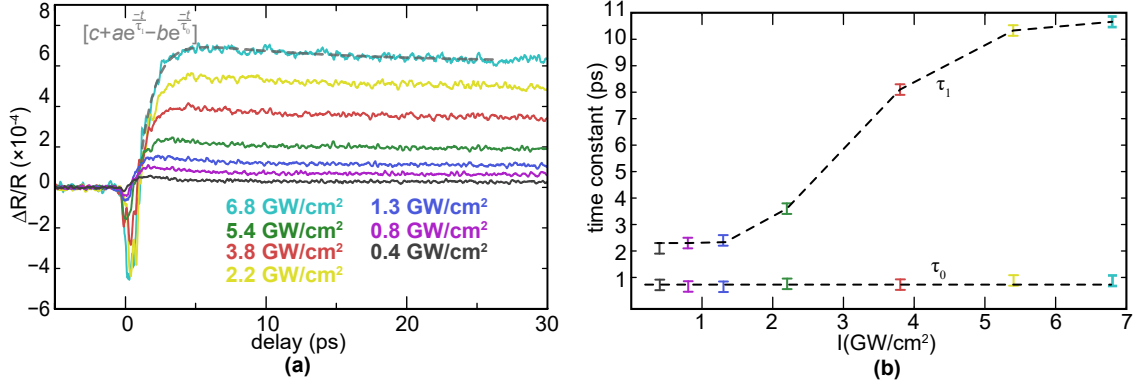
Figure 5.4: (a) Relative change in reflection $\Delta R/R$ (0.8-1.6 eV nm pump-probe) for a variety of pump peak intensities as a function of pump-probe time delay. The dashed grey curve is an example (for $I = 6.8$ GW/cm^2) of bi-exponential fit used here. (b) Extracted time-constants from bi-exponential fit to pump-probe data shown in part (a). The shorter time constant τ_0 is temperature independent within the error of measurements.

at small positive time delays with a bi-exponential function with two different time constants of τ_0 and τ_1, of the form $a\exp(-t/\tau_1) - b\exp(-t/\tau_0) + c$. An example (for $I = 6.8$ GW/cm^2) of the bi-exponential fit employed here is shown by a dashed grey curve in Fig. 5.4a. In Fig. 5.4b, we plot extracted time constants as a function of pump peak intensity I from bi-exponential fits to data in Fig. 5.4a. As shown in Fig. 5.4b, while the shorter time constant τ_0 appears to be independent of pump intensity within the error of measurements, τ_1 significantly increases from 2 ps to 10.5 ps by raising the pump intensity.

The relative change in reflection $\Delta R/R$ continues to decrease back to zero with a much slower time constant than those observed in Fig. 5.4, i.e. τ_0 and τ_1. To investigate the slow relaxation, we measure $\Delta R/R$ in a much longer range of
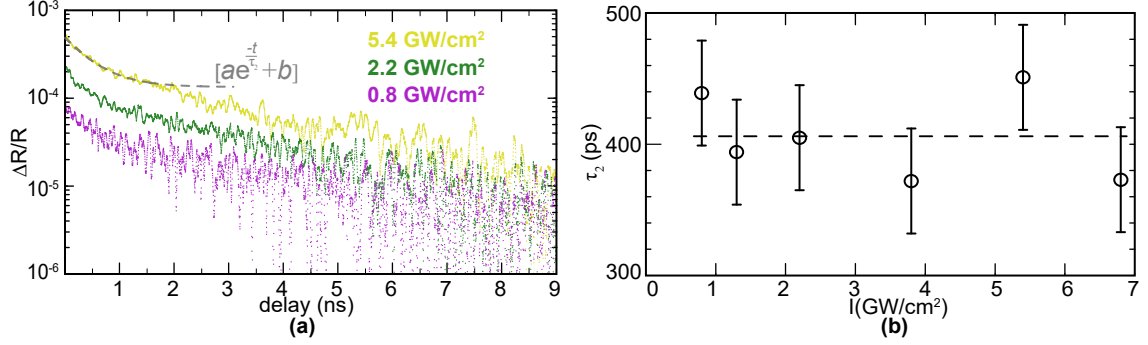
Figure 5.5: (a) Relative change in reflection $\Delta R/R$ (0.8-1.6 eV pump-probe) shown for large positive time delays ($\gtrsim 10$ ps). The dashed grey curve is an example (for $I = 5.4\,\mathrm{GW/cm^2}$) of exponential fit to the first 1 ns of data used here.(b) Extracted time constants from exponential fits to data in part (a). The time constant τ_2 is independent of pump intensity I within the error of measurements.

time delays up to 9 ns. These results are plotted in Fig. 5.5a for three different pump powers. We fit the first 1 ns time delay of $\Delta R/R$ pump-probe data with an exponential to extract the slow time constant τ_2. Fig. 5.5b plots the extracted time constant τ_2 as a function of the peak pump intensity I is constant within the error of our measurements. In addition to time delay dynamics associated with τ_2, we note that the data presented in Fig. 5.5a exhibit a much slower (few nanoseconds) evolution with time delay, that stretches the relaxation of $\Delta R/R$ to long time delays.

5.4.1.1 Discussion

Now we present a qualitative description of physical mechanisms behind the observed pump-induced change in reflection signal and various relaxation times observed in our measurements. The picture described here is based on thermalized

distribution of pump-induced hot electrons. We note that a similar model was employed to explain graphene pump-probe data [117].

The pump pulse excites electrons to a high energy state. These electrons start to thermalize through electron-electron scattering processes and develop an electronic temperature T_e that is much larger than the initial (lattice) temperature. This process occurs in a fast timescale (¡100 fs) that is beyond the resolution of our pump-probe data (pulsewidth limited). The elevation of electron temperature causes two competing processes that can change the probe pulse reflection:

(I) pump-induced Pauli blocking (interband): Hot electrons populate a wide range of energy states in the conduction band with an energy bandwidth proportional to $k_B T_e$. The tail of thermally populated states can extend to probe energy, and decrease the interband absorption of the probe pulse due to Pauli blocking.

(II) pump-induced change in Drude weight (intraband): When the electron temperature increases, Drude weight and probe reflection increase, as explained in (5.9).

The first process can be modeled by a temperature-dependent interband conductivity, similar to (5.3), and second one with a temperature-dependent Drude weight (5.9). In both cases, number of Weyl bands and their different chemical potentials need to be taken into account, according to explanations in 5.2.4.

As described above, while the first process causes a fast decrease in reflection, the second one increases the probe reflection. Pauli blocking is expected to dominate the pump-probe response at high electron temperature rise as the interband conductivity decreases approximately exponentially in T_e (equation (5.3)).

We now employ the thermal picture described above to explain the observed pump-probe signals: At zero time delay, pump pulse increases the electron temperature to a point that process (I) dominates and causes a a small reduction of probe reflection. Thus, a pump-induced modification of the probe interband absorption (Pauli blocking) can explain the observed initial ultrafast negative $\Delta R/R$. After thermalization and rise of T_e, hot electrons start to relax back to low energy levels through emitting phonons. This process is accompanied by reduction of the initially-elevated electron temperature. As T_e decreases, process (I) becomes weaker and (II) starts to dominate the change in reflection. This leads to a zero-crossing in $\Delta R/R$ where the effect of (I) and (II) processes are balanced, and subsequently a positive $\Delta R/R$. At a specific electron temperature, mechanism (II) completely dominates over (I), that leads to a maximum positive $\Delta R/R$. As T_e continues to decrease via hot electron-phonon relaxation, Drude weight decreases, and the positive $\Delta R/R$ slowly returns to zero.

Based on the above explanations, we attribute τ_0, τ_1, and τ_2 to electron-phonon relaxation times. We note that the values of τ_0 and τ_1 are within reasonable range for relaxation of hot carriers to optical phonons in a Dirac/Weyl system, whereas τ_2 is relaxation through acoustic phonons [122]. Compared to graphene, the relaxation of hot electrons to optical phonons are much slower, since the frequency/energy of optical phonon ($\approx$ 7 THz) in TaAs is much lower than that in graphene ($\approx$ 50 THz) [123, 124].

As shown in the last section of this chapter, temperature dependence of τ_1 is very similar to its pump intensity dependence presented in Fig. 5.4b. This observa-
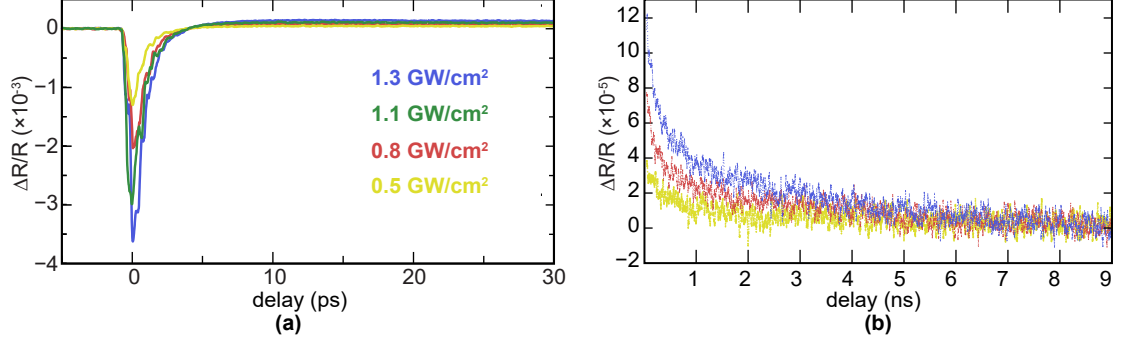
Figure 5.6: Relative change in reflection $\Delta R/R$ (1.6-0.8 eV pump-probe) for a variety of pump peak intensities shown in pump-probe time delays (a)around zero, and (b)larger than ≈ 5 ps where small positive change in reflection is observed.

tion suggests that the effect of pump intensity is primarily to increase the electron temperature, which is consistent with the thermodynamic picture for pump-probe signal described above.

In the time scale of τ_2 (hundreds of picosecond), electron temperature has significantly dropped from its value at zero time delay, and is already close to the lattice temperature. Therefore, τ_2 is not expected to depend strongly on intensity of pump pulse, which is consistent with data presented in Fig. 5.5.

5.4.2 Pump(1.6 eV)-Probe(0.8 eV)

Now we present measurement results for the 1.6 eV pump-0.8 eV probe configuration depicted in Fig. 5.3c. In Fig. 5.6, we show the measured $\Delta R/R$ for time delays around zero (a) and for long positive time delays (b).

All results, including the three extracted time constants (τ_0,τ_1,τ_2), are similar to those measured in 0.8 eV-1.6 eV pump-probe scheme, except that the initial

ultrafast negative change in reflection is much stronger. As described in the previous section, the ultrafast dip is caused by pump-induced transient Pauli blocking that causes an ultrafast reduction of probe pulse absorption/reflection. The Pauli blocking in 1.6 eV-0.8 eV pump-probe scheme is stronger for two reasons:

(i) Based on thermalized distribution of carriers: For the same temperature rise, a lower energy probe experiences an exponentially stronger reduction of phase space due from the distribution of thermalized carriers because it is closer to the Fermi surface. This behavior is expected from the interband conductivity formula (5.3). (ii) In the process of thermalization (non-equilibrium thermodynamics): when pump energy is higher than probe, as the pump-induced hot carriers thermalize and relax to low energies, they can limit the available phase space for probe-induced interband electronic transitions at the probe wavelength.

In Fig. 5.7, we plot positive maximum and negative minimum of $\Delta R/R$ as a function of pump peak intensity I for the two pump-probe schemes (data extracted from Fig. 5.4a and Fig. 5.6a). For the same pump peak intensity, which causes approximately same electron temperature rise, maximum of $\Delta R/R$ is similar for the two pump-probe schemes. This is expected from the thermodynamics picture described in the previous section, as the change in Drude weight is similar in both cases. However, for same pump intensities, negative minima are much larger for 1.6 eV-0.8 eV pump-probe measurements, since Pauli blocking is much stronger for a lower energy probe case. We also note that all data in Fig. 5.7 exhibit linear dependence on pump intensity, except minimum of 0.8 eV-1.6 eV pump-probe measurements.
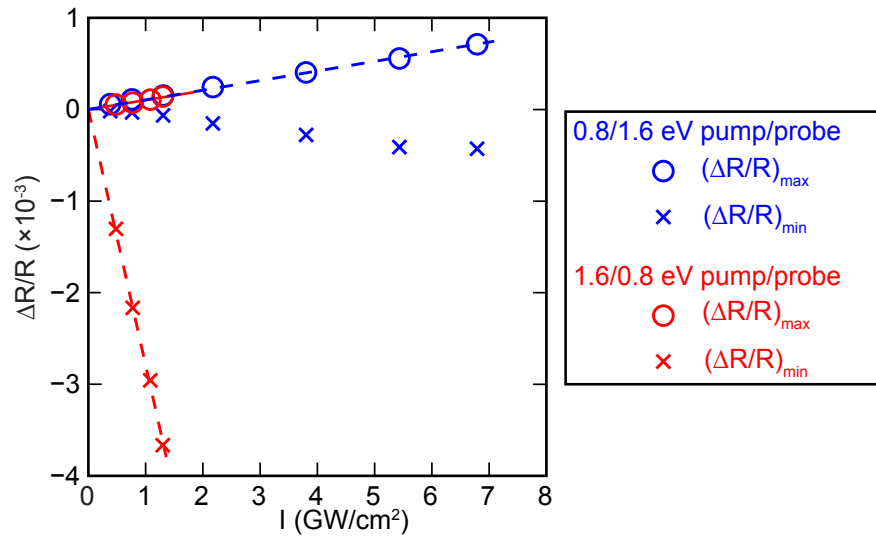
Figure 5.7: Maximum and minimum change in reflection vs time delay as a function of pump peak intensity for the two different pump-probe schemes. All data exhibit linear dependence on pump intensity (dashed lines) except the minimum of change in reflection for 0.8-1.6 eV pump-probe case.

5.5   Temperature Dependence Measurements

In this section, we investigate how the measured pump-probe signals and relaxation times depend of the lattice temperature. Fig. 5.8a shows the 0.8 eV pump-induced relative change in reflection of 1.6 eV probe at different measured temperatures in arbitrary units. Two clear effects are observed as we decrease the temperature of sample in cryostat: (i) The initial ultrafast negative Pauli blocking transient diminishes gradually and disappears at low temperatures. This is due to the fact that energy distribution of thermalized carriers becomes narrower at low temperatures, which results in weaker pump-induced Pauli blocking.

(ii) The relaxation of hot electrons (to optical phonons) become faster at low temperatures. In Fig. 5.8b, we plot extracted time constants τ_0 and τ_1 from bi-exponential fits to data in Fig. 5.8a as a function of temperature. We notice that the temperature-dependence of the two time constants is very similar to pump intensity-dependence presented in Fig. 5.4b. From this result, we infer that effect of pump intensity on τ_1 relaxation times is primarily thermal (related to the elevation of carriers/lattice temperature). This is consistent with an electron-phonon relaxation picture for τ_1 time constant: As temperature increases, either through increasing pump intensity or sample temperature, thermal relaxation becomes slower.

We now investigate the temperature dependence of slow carrier relaxation process with time constant τ_2 discussed in Fig. 5.5. In Fig. 5.9a, we show the relative change in reflection (normalized to the maximum value at small time delays) for different sample temperatures in a long range of pump-probe time delays up to
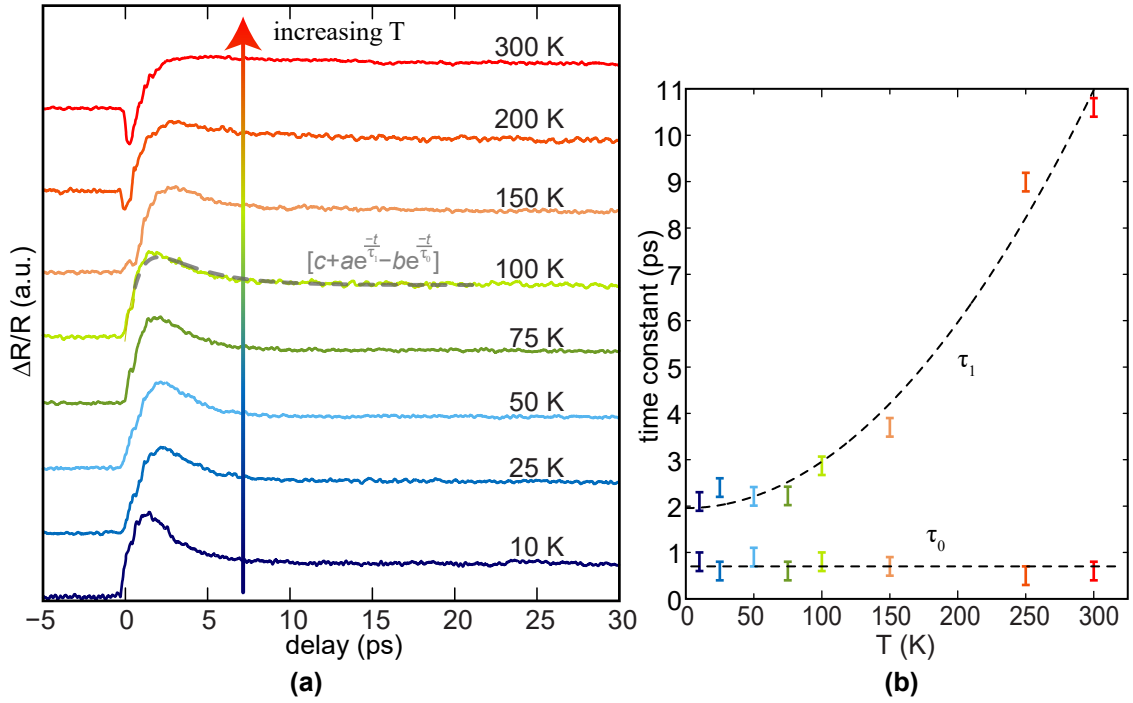
Figure 5.8: (a) Relative pump-induced change in reflection at variety of temperatures for 0.8-1.6 eV pump-probe case. The dashed grey curve is an example (for $T = 1005$ K) of bi-exponential fit used here. (b) Extracted time constant vs temperature from bi-exponential fits to data in part (a). The longer time constant τ_1 exhibits a quadratic dependence on temperature (dashed curve), while the shorter one τ_0 is temperature independent within the error of measurements.

5 ns. The relaxation time clearly becomes longer at higher temperatures, and to investigate this, we employ same type of exponential fitting as in Fig 5.5 to find the relaxation time τ_2 as a function of temperature. This result is presented in Fig. 5.9b which shows an increase of relaxation time τ_2 with temperature.

5.5.1 Temperature Dependence of Time Constants

The thermal relaxation time is $\tau = C/G$ where C and G are electronic specific heat and thermal conductivity to phonons respectively. The increase of both τ_1 and τ_2 with temperature is consistent with superlinear temperature dependence (T^3) of the specific heat C in 3D Dirac/Weyl system [122]. This suggests a weak dependence of thermal conductivity on temperature for hot electrons relaxation through optical and acoustic phonons in TaAs.

The increase of thermal relaxation time with temperature in TaAs is similar but much larger than what observed in conventional metals [125–127]. This is due to strong cubic dependence of specific heat on temperature in 3D Dirac systems [122].

We note that, while at low temperature the exponential curve fits the data accurately up to long time delays, at high temperatures $\Delta R/R$ deviates from a simple exponential dependence. We observed the same behavior for $\Delta R/R$ when we varied the pump intensity from low to high values (Fig. 5.5). We associate the non-exponential behavior that stretches the pump-probe signal at long time delays is due to the generation of hot phonons (lattice heating) in TaAs, and the associated time constant (few nanoseconds at room temperature) can be the speed of phonon-
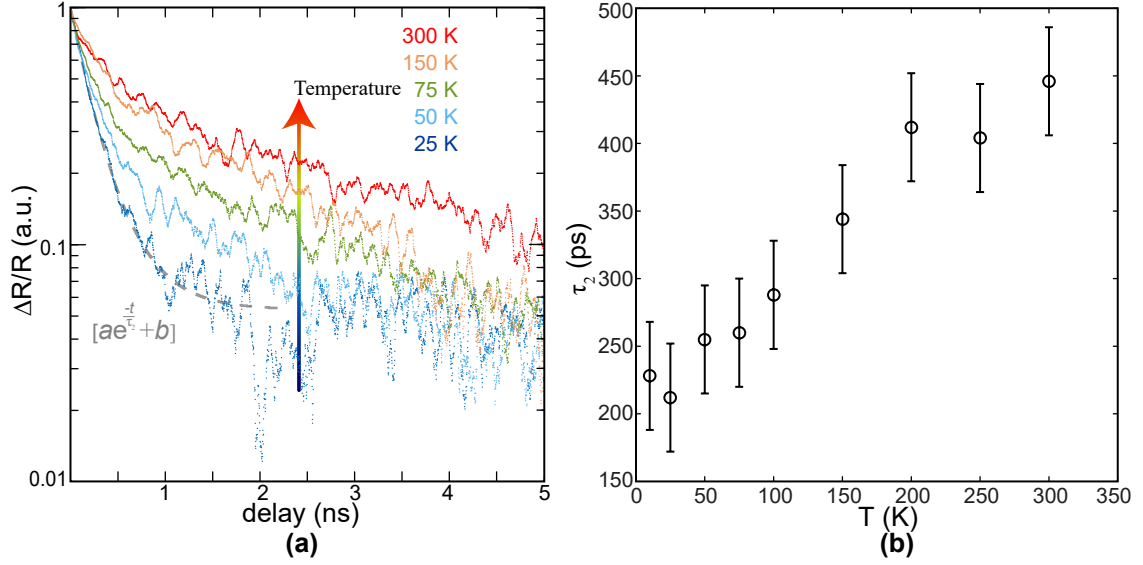
Figure 5.9: (a) Normalized pump-induced change in reflection (0.8-1.6 eV pump-probe) at variety of temperatures shown for large positive time delays ($\gtrsim 10$ ps). The dashed grey curve is an example (for $T = 25$ K) of exponential fit to the first 1 ns of data used here. (b) Extracted time constant τ_2 vs temperature from exponential fits to data in part (a).

phonon interaction in TaAs [128–130].

Finally, we should mention that the recombination of excited carriers can also decrease the Drude weight and explains the decay of $\Delta R/R$ back to zero. In that case, τ_1 and/or τ_2 can be regarded as carriers recombination times in TaAs. However, the observed increase of τ_1 and τ_2 with temperature is not expected from carrier recombination processes.

5.6 Conclusion

We use time-resolved optical pump-probe techniques to study the dynamics and relaxation of carriers in TaAs. Based on our qualitative thermodynamic model, observed change in reflection of probe is a result of two competing processes of pump-induced Pauli blocking and change in the Drude weight. Our measurements revealed that the relaxation of hot electrons through optical/acoustic phonons occur in ≈ 2 ps/200 ps at 10 K and becomes slower at elevated temperatures.

Chapter 6:   Future Directions

In this chapter, we briefly describe some potential future directions for each of the projects discussed in last four chapters.

6.1   Tunable Terahertz Optoelectronics using Metal-Graphene Plasmons

As discussed in Chapter 2, the hybrid metal-graphene plasmonic scheme can provide maximal absorption in graphene at a THz frequency that is tunable. This property is very attractive for realizing various tunable THz optoelectrnic devices such as detectors, absorbers, and emitters. Furthermore, using high mobility (low loss) graphene, these plasmonic structure would allow 100% transmission at a tunable frequency.   This can enable tunable THz bandpass filters and modulators. The key element for realizing practical THz applications of hybrid metal-graphene plasmons is to have access to high quality graphene (such as HBN-encapsulated graphene) in large areas. This is still a challenge, but is expected to be resolved in the near future.

6.2   Non-thermal Optical Nonlinearities in Graphene Plasmons

In chapter 3, we extensively studied nonlinear optical response of plasmonic resonances in graphene ribbons, and we concluded that a non-instantaneous thermal process dominates the nonlinear response. On the other hand, it has been theoretically suggested that graphene plasmons exhibit very strong non-thermal (instantaneous) nonlinearities, such as Kerr effect. Exploring these ultrafast nonlinearites are of great fundamental and practical interests. Two promising approaches could be to try: (1) using high mobility HBN-encapsulated graphene ribbons, (2) other resonance geometries instead of ribbons.

6.3   Terahertz Heterodyne Detection via 3-wave Mixing in Graphene

In chapter 4, we showed that mixing of two near-IR continuous waves (with frequencies f_1 and f_2) in graphene photo-thermo-electric devices produces a DC voltage that is a Lorentzian function of the difference frequency centered at $f_1 - f_2 = 0$.

Because of graphene's broadband optical absorption, the photo-thermo-electric mixing scheme is expected to be operable in other frequency regimes including THz. Furthermore, based on our theory, the nonlinear mixing can work for more than two waves. These two generalizations of photo-thermo-electric wave mixing in graphene can enable THz heterodyne detection. In the following, we describe a 3-wave mixing scheme in graphene for THz detection, along with a preliminary measurement result.

We use the same HBN-encapsulated graphene device shwon in Fig. 4.2. The experimental scheme is similar to the one depicted in Fig. 4.1 with two differences: (1) the two NIR beams are not mechanically chopped, and (2) in addition to two NIR beams, a third THz continuous-wave beam (mechanically-chopped) at $f_{THz} = 2.54$ THz is also focused on the graphene sample. In the absence of two NIR beams, the lock-in amplifier measures a DC photovoltage produced by the mechanically-modulated THz beam. When two NIR beams are present on the graphene sample, they mix with the THz wave though photo-thermo-electric nonlinearity and can change the measured DC photovoltage. In Fig. 6.1, we show the measured photovoltage as a function of difference frequency of the two NIR waves. A similar Lorentzian as in Fig. 4.5 is observed, but, rather than zero frequency, it is centered at $f_{THz} = 2.54$ THz.

The peak of the Lorentzian function in Fig. 6.1 is proportional to the product of the NIR beam intensities. We expect that, using intense NIR waves, the Lorentizan signal will be observable even if the intensity of THz beam is exceedingly small. Therefore, the 3-wave mixing scheme described above can enable heterodyne measurement of the intensity and frequency of an exceedingly small incoming THz wave using two strong NIR waves as "local oscillators".

6.4 Time-resolved Optical Study of Weyl Semimetals

The optical pump-probe study on TaAs presented in chapter 5 is the only time-resolved optical study that has been done on a Weyl semimetal. There are many
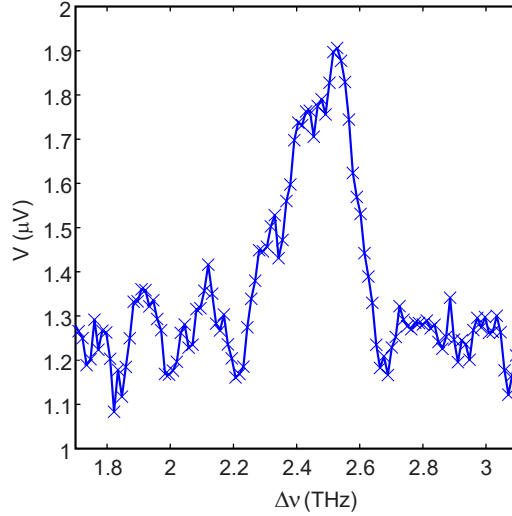
Figure 6.1: Measured photovoltage as a function of difference frequency of the two NIR waves.

other possible time-resolved optical studies on Weyl semimetals, including various pump-probe experiments at different photon energies from THz to visible, that can be used to fully determine heating/cooling rates and recombination dynamics of the carriers. There are also novel optical effects to experimentally explore in Weyl semimetals such as Berry curvature induced optical gyrotropy [46], anomalous Hall effect in inversion-broken-symmetry systems [47], topological nonlinear optical effects [131], and circular photogalvanic effects.

6.4.1 Measurement of SPP Dispersion in Weyl Semimetals

Among the new phenomena predicted by the Berry phase in Weyl semimetals is surface plasmon polaritons (SPPs) with new magneto-plasmon-features in the absence of an applied magnetic field. Berry curvature associated with the Weyl nodes produce effective magnetic monopoles in momentum space and drastically modify

the surface plasmon dispersion. The plasmon diepsersion relations can be obtained experimentally using a THz-TDS technique which, in addition to the amplitude, can measure the phase of a THz wave as it poropagates [132, 132, 133]. One attractive measurement is to pattern gratings on a Weyl semimetal crystal using a focused-ion-beam tool to couple the incident terahertz radiation to SPPs, and then use a THz-TDS technique to measure the dispersion relation of SPPs propagating on the crystal surface.

Appendix A: Derivations–Graphene Nonlinear Photomixing Model

The electron temperature in the graphene may be modeled by the following nonlinear differential equation:

$$\alpha T \frac{dT}{dt} + \beta_1(T - T_L) + \beta_3(T^3 - T_L^3) = I(t) \tag{A.1}$$

where T represents the graphene electron temperature, T_L is the lattice temperature, and $I(t)$ is the absorbed optical power per unit area. αT is the specific heat in the graphene and the terms proportional to β_1 and β_3 describe momentum-conserving cooling and disorder-assisted supercollision cooling, respectively.

We re-write these equations in terms of $x \equiv T - T_L$, the deviation from the lattice temperature:

$$\alpha(T_L + x)\frac{dx}{dt} + \beta_1 x + \beta_3 \left[(T_L + x)^3 - T_L^3\right] = I(t) \tag{A.2}$$

We next assume that $x \ll T_L$, i.e., the photoinduced change in electron temperature is small in comparison to the equilibrium (lattice) temperature. With this assumption, $x(t)$ may be expanded in a power series in the intensity I,

$$x(t) = x^{(1)}(t) + x^{(2)}(t) + x^{(3)}(t) + \ldots \tag{A.3}$$

Where $x^{(n)} \propto I^n$, and we are retaining terms up to third order. Substituting this

expansion into (A.2) gives

$$\alpha(T_L + x^{(1)} + x^{(2)} + x^{(3)})\frac{d}{dt}(x^{(1)} + x^{(2)} + x^{(3)}) + \beta_1(x^{(1)} + x^{(2)} + x^{(3)}) +$$

$$\beta_3\left[(T_L + x^{(1)} + x^{(2)} + x^{(3)})^3 - T_L^3\right] = I(t) \quad \text{(A.4)}$$

Next, we expand (A.4) and separately equate the orders to obtain the following inhomogeneous linear differential equations for $x^{(1)}$, $x^{(2)}$ and $x^{(3)}$,

$$\alpha T_L\frac{dx^{(1)}}{dt} + (\beta_1 + 3\beta_3 T_L^2)x^{(1)} = I(t) \tag{A.5}$$

$$\alpha T_L\frac{dx^{(2)}}{dt} + (\beta_1 + 3\beta_3 T_L^2)x^{(2)} = -\alpha x^{(1)}\frac{dx^{(1)}}{dt} - 3\beta_3 T_L\left[x^{(1)}\right]^2 \tag{A.6}$$

$$\alpha T_L\frac{dx^{(3)}}{dt} + (\beta_1 + 3\beta_3 T_L^2)x^{(3)} = -\alpha x^{(1)}\frac{dx^{(2)}}{dt} - \alpha x^{(2)}\frac{dx^{(1)}}{dt} - 6\beta_3 T_L x^{(1)}x^{(2)} - \beta_3\left[x^{(1)}\right]^3$$

$$\tag{A.7}$$

which can be re-written as:

$$\frac{dx^{(1)}}{dt} + \gamma x^{(1)} = \frac{I(t)}{\alpha T_L} \tag{A.8}$$

$$\frac{dx^{(2)}}{dt} + \gamma x^{(2)} = -\frac{1}{T_L}x^{(1)}\frac{dx^{(1)}}{dt} - \frac{3\beta_3}{\alpha}\left[x^{(1)}\right]^2 \tag{A.9}$$

$$\frac{dx^{(3)}}{dt} + \gamma x^{(3)} = -\frac{1}{T_L}x^{(1)}\frac{dx^{(2)}}{dt} - \frac{1}{T_L}x^{(2)}\frac{dx^{(1)}}{dt} - \frac{6\beta_3}{\alpha}x^{(1)}x^{(2)} - \frac{\beta_3}{\alpha T_L}\left[x^{(1)}\right]^3 \tag{A.10}$$

where

$$\gamma \equiv \frac{\beta_1 + 3\beta_3 T_L^2}{\alpha T_L} \tag{A.11}$$

represents the equivalent (linearized) cooling rate, taking into account both cooling mechanisms.

For the two-laser illumination considered here, the optical intensity absorbed in the graphene is given by

$$I(t) = I_1 + I_2 + 2\sqrt{I_1 I_2}\cos\Omega t \tag{A.12}$$

where I_1 is the absorbed intensity of laser 1, I_2 is the absorbed intensity of laser 2, and $\Omega \equiv \omega_1 - \omega_2$ is the heterodyne beat frequency between the two lasers.

Substituting this expression into (A.8), one can find a solution for $x^{(1)}(t)$, which is used in turn to find $x^{(2)}(t)$ from (A.9), and $x^{(3)}(t)$ from (A.10).

The photovoltage produced through the Seebeck effect can be expressed as

$$V(t) = rT(T - T_L) = rx(x + T_L) \tag{A.13}$$

where rT is the Seebeck coefficient of graphene. Substituting $x = x^{(1)} + x^{(2)} + x^{(3)} + \ldots$ into (A.13), evaluating only the DC component of $V(t)$, and retaining only terms up to the third order in I, one finds, after simplification:

$$V(I_1, I_2) = r \left\{ \frac{I_1 + I_2}{\alpha\gamma} + \beta_1 \frac{(I_1 + I_2)^2}{(\alpha\gamma T_L)^3} - (3\beta_3^2 T_L^4 + 7T_L^2 \beta_1 \beta_3) \frac{(I_1 + I_2)^3}{T_L^6 \alpha^5 \gamma^5} \right. \quad \cdots \tag{A.14}$$

$$+ 2I_1 I_2 \left[\frac{\beta_1}{(\alpha\gamma T_L)^3} - (9T_L^4 \beta_3^2 + 15T_L^2 \beta_1 \beta_3 + 2\beta_1^2) \frac{(I_1 + I_2)}{T_L^6 \alpha^5 \gamma^5} \right] \frac{\gamma^2}{\Omega^2 + \gamma^2} \quad \cdots$$

$$\tag{A.15}$$

$$\left. - 2I_1 I_2 \left[(6T_L^2 \beta_1 \beta_3 - 2\beta_1^2) \frac{(I_1 + I_2)}{T_L^6 \alpha^5 \gamma^5} \right] \left(\frac{\gamma^2}{\Omega^2 + \gamma^2} \right)^2 \right\} \tag{A.16}$$

For the room-temperature conditions reported here ($T_L = 300$ K), we may make the additional approximation that $\beta_1 \ll \beta_3 T_L^2$. In this regime, the linearized cooling rate (γ) is determined primarily by supercollision cooling, even though both cooling processes contribute to the measured nonlinearity in the response. With this assumption, (A.14)-(A.16) simplify to:

$$V(I_1, I_2) = r \left\{ \frac{I_1 + I_2}{\alpha\gamma} + \beta_1 \frac{(I_1 + I_2)^2}{(\alpha\gamma T_L)^3} - 3\beta_3^2 \frac{(I_1 + I_2)^3}{T_L^2 \alpha^5 \gamma^5} \right. \quad \cdots \tag{A.17}$$

$$\left. + 2I_1 I_2 \left[\frac{\beta_1}{(\alpha\gamma T_L)^3} - 9\beta_3^2 \frac{(I_1 + I_2)}{T_L^2 \alpha^5 \gamma^5} \right] \frac{\gamma^2}{\Omega^2 + \gamma^2} \right\} \tag{A.18}$$

The photoinduced voltage can be rewritten as

$$V(I_1, I_2) = a_1(I_1 + I_2) + a_2(I_1^2 + I_2^2) - a_3(I_1^3 + I_2^3) \quad \ldots \tag{A.19}$$

$$+ 2a_2 I_1 I_2 \left[1 + \frac{\gamma^2}{\Omega^2 + \gamma^2} \right] - 3a_3 I_1 I_2 (I_1 + I_2) \left[1 + \frac{2\gamma^2}{\Omega^2 + \gamma^2} \right] \tag{A.20}$$

where the coefficients a_1, a_2 and a_3 are given by

$$a_1 \equiv \frac{r}{\alpha\gamma}, \quad a_2 \equiv \frac{\beta_1}{(\alpha\gamma T_L)^3}, \quad a_3 \equiv \frac{3\beta_3^2}{T_L^2 \alpha^5 \gamma^5} \tag{A.21}$$

When the two beams I_1 and I_2 are double-chopped and synchronously detected at the chopper difference frequency, the lock-in amplifier produces a signal proportional to (A.20):

$$V_\Delta = V(I_1, I_2) - V(I_1, 0) - V(0, I_2) + V(0, 0) \tag{A.22}$$

$$= 2a_2 I_1 I_2 \left[1 + \frac{\gamma^2}{\Omega^2 + \gamma^2} \right] - 3a_3 I_1 I_2 (I_1 + I_2) \left[1 + \frac{2\gamma^2}{\Omega^2 + \gamma^2} \right] \tag{A.23}$$

The DC photovoltage therefore has a Lorentzian dependence on the heterodyne difference frequency $\Omega \equiv \omega_1 - \omega_2$, with a spectral width that is proportional to the carrier cooling rate γ, as shown schematically in Fig. A.1
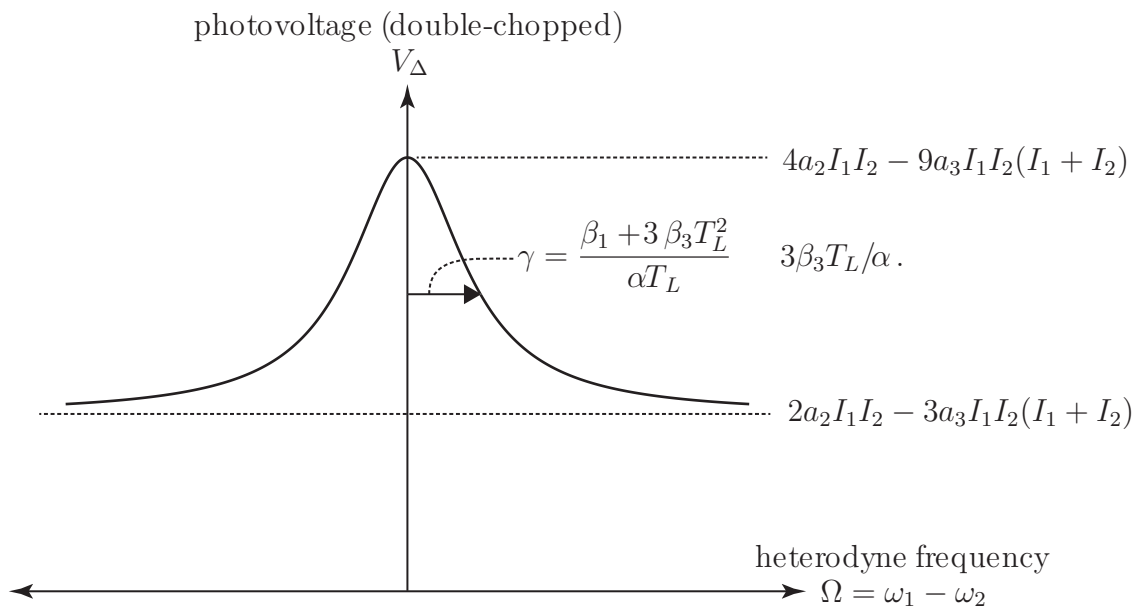
Figure A.1: DC photovoltage V_Δ as a function of the heterodyne difference frequency $\Omega = \omega_1 - \omega_2$.

Bibliography

[1] K.S. Novoselov, A.K. Geim, S.V. Morozov, D. Jiang, Y. Zhang, S.V. Dubonos, I.V. Grigorieva, and A.A. Firsov. Graphene plasmonics for terahertz to mid-infrared applications. *Science*, 306(5696):666–669, 2004.

[2] K.S. Novoselov, D. Jiang, F. Schedin, T.J. Booth, V.V. Khotkevich, S.V. Morozov, and A.K. Geim. Two-dimensional atomic crystals. *Proc. Natl. Acad. Sci.*, 102(30):10451–10453, 2005.

[3] K.S.A. Novoselov, A.K. Geim, S. Morozov, D. Jiang, M. Katsnelson, I. Grigorieva, S. Dubonos, and A. Firsov. Two-dimensional gas of massless Dirac fermions in graphene. *Nature*, 438(7065):197–200, 2005.

[4] A. H. Castro Neto, F. Guinea, N. M. R. Peres, K. S. Novoselov, and A. K. Geim. The electronic properties of graphene. *Rev. Mod. Phys*, 81(1):109, 2009.

[5] S. Das Sarma, S. Adam, E. H. Hwang, and E. Rossi. Electronic transport in two-dimensional graphene. *Rev. Mod. Phys.*, 83:407–470, May 2011.

[6] Z. Fei, A. S. Rodin, G. O. Andreev, W. Bao, A. S. McLeod, M. Wagner, L. M. Zhang, Z. Zhao, M. Thiemens, G. Dominguez, M. M. Fogler, A. H. Castro Neto, C. N. Lau, F. Keilmann, and D. N. Basov. Gate-tuning of graphene plasmons revealed by infrared nano-imaging. *Nature*, 487:82–85, 2012.

[7] J. Chen, M. Badioli, P. Alonso-Gonzlez, S. Thongrattanasiri, F. Huth, J. Osmond, M. Spasenovi, A. Centeno, A. Pesquera, P. Godignon, A. Z. Elorza, N. Camara, F. J. Garca de Abajo, R. Hillenbrand, and F. H. L. Koppens. Optical nano-imaging of gate-tunable graphene plasmons. *Nature*, 487:77–81, 2012.

[8] L. Ju, B. Geng, J. Horng, C. Girit, M. Martin, Z. Hao, H. A. Bechtel, X. Liang, A. Zettl, Y. R. Shen, and F. Wang. Graphene plasmonics for tunable terahertz metamaterials. *Nature Nanotech.*, 6:630–634, 2011.

[9] H. Yan, X. Li, B. Chandra, G. Tulevski, Y. Wu, M. Freitag, W. Zhu, P. Avouris, and F. Xia. Tunable infrared plasmonic devices using graphene/insulator stacks. *Nature Nanotech.*, 7:330–334, 2012.

[10] T. Low and P. Avouris. Graphene plasmonics for terahertz to mid-infrared applications. *ACS Nano*, 8(2):1086–1101, 2014.

[11] R. R. Hartmann, J. Kono, and M. E. Portnoi. Terahertz science and technology of carbon nanomaterials. *Nanotechnology*, 25:322001, 2014.

[12] L. Vicarelli, M. S. Vitiello, D. Coquillat, A. Lombardo, A. C. Ferrari, W. Knap, M. Polini, V. Pellegrini, and A. Tredicucci. Graphene field-effect transistors as room-temperature terahertz detectors. *Nature Mater.*, 11:865–871, 2012.

[13] X. Cai, A. B. Sushkov, R. J. Suess, M. M. Jadidi, G. S. Jenkins, L. O. Nyakiti, R. L. Myers-Ward, S. Li, J. Yan, D. K. Gaskill, T. E. Murphy, H. D. Drew, and M. S. Fuhrer. Sensitive room-temperature terahertz detection via the photothermoelectric effect in graphene. *Nat. Nanotechnol.*, 9(10):814–819, 2014.

[14] B. Sensale-Rodriguez, R. Yan, M. M. Kelly, T. Fang, K. Tahy, W. S. Hwang, D. Jena, L. Liu, and H. G. Xing. Broadband graphene terahertz modulators enabled by intraband transitions. *Nat. Commun.*, 3:780, 2012.

[15] S. H. Lee, M. Choi, T.-T. Kim, S. Lee, M. Liu, X. Yin, H. K. Choi, S. S. Lee, C.-G. Choi, S.-Y. Choi, X. Zhang, and B. Min. Switching terahertz waves with gate-controlled active graphene metamaterials. *Nature Mater.*, 11:936–941, 2012.

[16] S.-F. Shi, B. Zeng, H.-L. Han, X. Hong, H.-Z. Tsai, H. S. Jung, A. Zettl, M. F. Crommie, and F. Wang. Optimizing Broadband Terahertz Modulation with Hybrid Graphene/Metasurface Structures. *Nano Lett.*, 15:372–377, 2014.

[17] S.A. Mikhailov and K. Ziegler. Nonlinear electromagnetic response of graphene: frequency multiplication and the self-consistent-field effects. *J. Phys. Condens. Matter.*, 20(38), 2008.

[18] E. Hendry, P. J. Hale, J. Moger, A. K. Savchenko, and S. A. Mikhailov. Coherent Nonlinear Optical Response of Graphene. *Phys. Rev. Lett.*, 105(097401), 2010.

[19] H. Zhang, D. Y. Tang, L. M. Zhao, Q. L. Bao, and K. P. Loh. Large energy mode locking of an erbium-doped fiber laser with atomic layer graphene. *Opt. Express*, 17(17630-17635), 2009.

[20] S.-Y. Hong, J. I. Dadap, N. Petrone, P. Yeh, J. Hone, and R. M. Osgood. Optical Third-Harmonic Generation in Graphene. *Phys. Rev. X*, 3(021014), 2013.

[21] H. Zhang, S. Virally, Q. Bao, L. K. Ping, S. Massar, N. Godbout, and P. Kockaert. Z-scan measurement of the nonlinear refractive index of graphene. *Opt. Lett.*, 37, 2012.

[22] G. Jnawali, Y. Rao, H. Yan, and T. F. Heinz. Observation of a Transient Decrease in Terahertz Conductivity of Single-Layer Graphene Induced by Ultrafast Optical Excitation. *Nano Lett.*, 13(2):524–530, 2013.

[23] S.-F. Shi, T.-T. Tang, B. Zeng, L. Ju, Q. Zhou, A. Zettl, and F. Wang. Controlling Graphene Ultrafast Hot Carrier Response from Metal-like to Semiconductor-like by Electrostatic Gating. *Nano Lett.*, 14(3):1578–1582, 2014.

[24] H. Y. Hwang, N. C. Brandt, H. Farhat, A. L. Hsu, J. Kong, and K. A. Nelson. Nonlinear THz Conductivity Dynamics in P-Type CVD-Grown Graphene. *J. Phys. Chem. B*, 117(49):15819–15824, 2013.

[25] F. Kadi, T. Winzer, E. Malic, A. Knorr, F. Göttfert, M. Mittendorff, S. Winnerl, and M. Helm. Microscopic Description of Intraband Absorption in Graphene: The Occurrence of Transient Negative Differential Transmission. *Phys. Rev. Lett.*, 113:035502, Jul 2014.

[26] Z. Mics, K.-J. Tielrooij, K. Parvez, S. A. Jensen, I. Ivanov, X. Feng, K. Müllen, M. Bonn, and D. Turchinovich. Thermodynamic picture of ultrafast charge transport in graphene. *Nat. Commun.*, 6:7655, 2015.

[27] Y.M. Zuev, W. Chang, and P. Kim. Thermoelectric and magnetothermoelectric transport measurements of graphene. *Phys. Rev. Lett.*, 102(9):096807, 2009.

[28] X. Xu, N.M. Gabor, J.S. Alden, A.M. van der Zande, and P.L. McEuen. Photo-Thermoelectric Effect at a Graphene Interface Junction. *Nano Lett.*, 10(2):562–566, 2009.

[29] N.M. Gabor, J.C. Song, Q. Ma, N.L. Nair, T. Taychatanapat, K. Watanabe, T. Taniguchi, L.S. Levitov, and P. Jarillo-Herrero. Hot carrier-assisted intrinsic photoresponse in graphene. *Science*, 334(6065):648–652, 2011.

[30] F.H.L. Koppens, T. Mueller, P. Avouris, A.C. Ferrari, M.S. Vitiello, and M. Polini. Photodetectors based on graphene, other two-dimensional materials and hybrid systems. *Nat. Nanotechnol.*, 9(10):780–793, 2014.

[31] J. C. W. Song, M. Y. Reizer, and L. S. Levitov. Disorder-Assisted Electron-Phonon Scattering and Cooling Pathways in Graphene. *Phys. Rev. Lett.*, 109:106602, Sep 2012.

[32] M.W. Graham, S.F. Shi, D.C. Ralph, J. Park, and P.L. McEuen. Photocurrent measurements of supercollision cooling in graphene. *Nat. Phys.*, 9(2):103–108, 2013.

[33] Q. Ma, N.M. Gabor, T.I. Andersen, N.L. Nair, K. Watanabe, T. Taniguchi, and P. Jarillo-Herrero. Competing channels for hot-electron cooling in graphene. *Phys. Rev. Lett.*, 112(24):247401, 2014.

[34] R. Bistritzer and A. H. MacDonald. Electronic Cooling in Graphene. *Phys. Rev. Lett.*, 102:206410, May 2009.

[35] W.-K. Tse and S. Das Sarma. Energy relaxation of hot Dirac fermions in graphene. *Phys. Rev. B*, 79:235406, Jun 2009.

[36] A. C. Betz, F. Vialla, D. Brunel, C. Voisin, M. Picher, A. Cavanna, A. Madouri, G. Fève, J.-M. Berroir, B. Plaçais, and E. Pallecchi. Hot Electron Cooling by Acoustic Phonons in Graphene. *Phys. Rev. Lett.*, 109:056805, Aug 2012.

[37] A. C. Betz, F. Vialla, D. Brunel, C. Voisin, M. Picher, A. Cavanna, A. Madouri, G. Fève, J.-M. Berroir, B. Plaçais, and E. Pallecchi. Super-collision cooling in undoped graphene. *Nat. Phys.*, 9:109–112, 2013.

[38] R.J. Shiue, Y. Gao, Y. Wang, C. Peng, A.D. Robertson, D.K. Efetov, S. Assefa, F.H. Koppens, J. Hone, and D. Englund. High-Responsivity GrapheneBoron Nitride Photodetector and Autocorrelator in a Silicon Photonic Integrated Circuit. *Nano Lett.*, 15(11):7288–7293, 2015.

[39] C. B. McKitterick, D. E. Prober, and M. J. Rooks. Electron-phonon cooling in large monolayer graphene devices. *Phys. Rev. B*, 93:075410, Feb 2016.

[40] M. Neupane1, S.-Y. Xu, R. Sankar, N. Alidoust, G. Bian, C. Liu, Ilya Belopolski, T.-R. Chang, H.-T. Jeng, H. Lin, A. Bansil, F. Chou, and M. Z. Hasan. Observation of a three-dimensional topological Dirac semimetal phase in high-mobility Cd$_3$As$_2$. *Nat. Commun.*, 5:3786, 2014.

[41] Z. K. Liu, B. Zhou, Y. Zhang, Z. J. Wang, H. M. Weng, D. Prabhakaran, S.-K. Mo, Z. X. Shen, Z. Fang, X. Dai, Z. Hussain, and Y. L. Chen. Discovery of a Three-Dimensional Topological Dirac Semimetal, Na$_3$Bi. *Science*, 343(6173):864–867, 2014.

[42] A. A. Burkov and L. Balents. Weyl Semimetal in a Topological Insulator Multilayer. *Phys. Rev. Lett.*, 107(4):127205, 2011.

[43] P. Hosur, S. A. Parameswaran, and A. Vishwanath. Charge Transport inWeyl Semimetals. *Phys. Rev. Lett.*, 108(5):046602, 2012.

[44] A. Bansil, H. Lin, and T. Das. Colloquium: Topological band theory. *Rev. Mod. Phys.*, 88:021004, 2016.

[45] P. Hosur and X.-L. Qi. Tunable circular dichroism due to the chiral anomaly in Weyl semimetals. *Phys. Rev. B*, 91(8):081106, 2015.

[46] S. Zhong, J. Orenstein, and J. E. Moore. Optical Gyrotropy from Axion Electrodynamics in Momentum Space. *Phys. Rev. Lett.*, 115(11):117403, 2015.

[47] C-K Chan, P. A. Lee, K. S. Burch, J. H. Han, and Y. Ran. When Chiral Photons Meet Chiral Fermions:Photoinduced Anomalous Hall Effects in Weyl Semimetals. *Phys. Rev. Lett.*, 116(2):026805, 2016.

[48] S.-Y. Xu et al. Discovery of a Weyl fermion semimetal and topological Fermi arcs. *Science*, 349(6248):613–617, 2015.

[49] B. Q. Lv, H. M. Weng, B. B. Fu, X. P. Wang, H. Miao, J. Ma, P. Richard, X. C. Huang, L. X. Zhao, G. F. Chen, Z. Fang, X. Dai, T. Qian, and H. Ding. Experimental Discovery of Weyl Semimetal TaAs. *Phys. Rev. X*, 5(3):03113, 2015.

[50] L. X. Yang, Z. K. Liu, Y. Sun, H. Peng, H. F. Yang, T. Zhang, B. Zhou, Y. Zhang, Y. F. Guo, M. Rahn, D. Prabhakaran, Z. Hussain, S.-K. Mo, C. Felser, B. Yan, and Y. L. Chen. Weyl semimetal phase in the non-centrosymmetric compound TaAs. *Nat. Phys.*, 11(9):728–732, 2015.

[51] M. M. Jadidi, A. B. Sushkov, R. L. Myers-Ward, A. K. Boyd, K. M. Daniels, D. K. Gaskill, M. S. Fuhrer, H. D. Drew, and T. E. Murphy. Tunable Terahertz Hybrid Metal-Graphene Plasmons. *Nano Lett.*, 15(10):7099–7104, 2015.

[52] V. P. Gusynin, S. G. Sharapov, and J. P. Carbotte. Unusual Microwave Response of Dirac Quasiparticles in Graphene. *Phys. Rev. Lett.*, 96(25):256802, 2006.

[53] L. A. Falkovsky. Optical properties of graphene. *J. Phys.: Conference Series*, 129:012004, 2008.

[54] K. F. Mak, M. Y. Sfeir, Y. Wu, C. H. Lui, J. A. Misewich, and T. F. Heinz. Measurement of the Optical Conductivity of Graphene. *Phys. Rev. Lett.*, 101(4):196405, 2008.

[55] Y. Yao, M. A. Kats, P. Genevet, N. Yu, Y. Song, J. Kong, and F. Capasso. Broad Electrical Tuning of Graphene-Loaded Plasmonic Antennas. *Nano Lett.*, 13:1257–1264, 2013.

[56] E. H. Hwang and S. Das Sarma. Dielectric function, screening, and plasmons in two-dimensional graphene. *Phys. Rev. B*, 75(20):205418, 2007.

[57] F. H. L. Koppens, D. E. Chang, and F. J. García de Abajo. Graphene Plasmonics: A Platform for Strong Light–Matter Interactions. *Nano Lett.*, 11:3370–3377, 2011.

[58] Y. V. Bludov, A. Ferreira, N. M. R. Peres, and M. I. Vasilevskiy. A primer on surface plasmon-polaritons in graphene. *Int. J. Mod. Phys. B*, 27(10):1341001, 2013.

[59] A. Yu. Nikitin, T. Low, and L. Martin-Moreno. Anomalous reflection phase of graphene plasmons and its influence on resonators. *Phys. Rev. B*, 90:041407, 2014.

[60] K. A. Velizhanin. Geometric universality of plasmon modes in graphene nanoribbon arrays. *Phys. Rev. B*, 91:125429, 2015.

[61] X. Cai, A. B. Sushkov, M. M. Jadidi, L. O Nyakiti, R. L. Myers-Ward, D. K. Gaskill, T. E. Murphy, M. S. Fuhrer, and H. D. Drew. Plasmon-enhanced Terahertz Photodetection in Graphene. *Nano Lett.*, 15(7):4295–4302, 2015.

[62] P. Nene, J. H. Strait, W.-M. Chan, C. Manolatou, S. Tiwari, P. L. McEuen, and F. Rana. Coupling of plasmon modes in graphene microstructures. *Appl. Phys. Lett.*, 105(14):143108, 2014.

[63] L. B. Whitbourn and R. C. Compton. Equivalent-circuit formulas for metal grid reflectors at a dielectric boundary. *Appl. Optics*, 24(2):217–220, 1985.

[64] P.-Y. Chen and A. Alù. Terahertz Metamaterial Devices Based on Graphene Nanostructures. *IEEE Trans. THz Sci. Technol.*, 3(6):748–756, 2013.

[65] S. A. Mikhailov and N. A. Savostianova. Influence of contacts on the microwave response of a two-dimensional electron stripe. *Phys. Rev. B*, 74:045325, 2006.

[66] C. Hilsum. Infrared Absorption of Thin Metal Films. *J. Opt. Soc. Am.*, 44:187–191, 1954.

[67] M. S. Jang, V. W. Brar, M. C. Sherrott, J. J. Lopez, L. Kim, S. Kim, M. Choi, and H. A. Atwater. Tunable large resonant absorption in a mid-infrared graphene Salisbury screen. *Phys. Rev. B*, 90:165409, 2014.

[68] R. Ulrich. Far-infrared properties of metallic mesh and its complementary structure. *Infrared Phys.*, 7(1):37–55, 1967.

[69] C. A. Balanis. *Antenna theory analysis and design.* John Wiley, 3rd edition, 2012.

[70] A. Alù and N. Engheta. Input Impedance, Nanocircuit Loading, and Radiation Tuning of Optical Nanoantennas. *Phys. Rev. Lett.*, 101:043901, 2008.

[71] A. Alù and N. Engheta. Theory, Modeling and Features of Optical Nanoantennas. *IEEE Trans. Antennas Propag.*, 61(4):1508–1517, 2013.

[72] F. W. Carter, D. F. Santavicca, and D. E. Prober. A plasmonic antenna-coupled superconducting near-IR photon detector. *Opt. Express*, 22(18):22062–22071, 2014.

[73] L.O. Nyakiti, V.D. Wheeler, N.Y. Garcesa, R.L. Myers-Ward, C.R. Eddy Jr., and D.K. Gaskill. Enabling graphene-based technologies: Toward wafer-scale production of epitaxial graphene. *MRS Bull.*, 37:1149–1157, 2012.

[74] P.A. Khomyakov, A.A. Starikov, G. Brocks, and P.J. Kelly. Nonlinear screening of charges induced in graphene by metal contacts. *Phys. Rev. B*, 82(11):115437, 2010.

[75] S. H. Mousavi, I. Kholmanov, K. B. Alici, D. Purtseladze, N. Arju, K. Tatar, D. Y. Fozdar, J. W. Suk, Y. Hao, A. B. Khanikaev, R. S.Ruoff, and G. Shvets. Inductive Tuning of Fano-Resonant Metasurfaces Using Plasmonic Response of Graphene in the Mid-Infrared. *Nano Lett.*, 13:1111–1117, 2013.

[76] A. Ferreira and N. M. R. Peres. Complete light absorption in graphene-metamaterial corrugated structures. *Phys. Rev. B*, 86:205401, 2012.

[77] M. Kauranen and A. V. Zayats. Nonlinear plasmonics. *Nature Photon.*, 6:737–748, 2012.

[78] V. W. Brar, M. S. Jang, M. Sherrott, J. J. Lopez, and H. A. Atwater. Highly Confined Tunable Mid-Infrared Plasmonics in Graphene Nanoresonators. *Nano Lett.*, 13:2541–2547, 2013.

[79] H. Yan, T. Low, W. Zhu, Y. Wu, M. Freitag, X. Li, F. Guinea, P. Avouris, and F. Xia. Damping pathways of mid-infrared plasmons in graphene nanostructures. *Nature Photon.*, 7:394–399, 2013.

[80] A. Manjavacas, P. Nordlander, and F. J. García de Abajo. Plasmon Blockade in Nanostructured Graphene. *ACS Nano*, 6:1724–1731, 2012.

[81] Gullans, M. and Chang, D.E. and Koppens, F. H. L. and García de Abajo, F. J. and Lukin, M. D. Single-photon nonlinear optics with graphene plasmons. *Phys. Rev. Lett.*, 111:247401, 2013.

[82] X. Yao, M. Tokman, and A. Belyanin. Efficient Nonlinear Generation of THz Plasmons in Graphene and Topological Insulators. *Phys. Rev. Lett.*, 112(055501), 2014.

[83] M. Jablan and D. E. Chang. Multiplasmon Absorption in Graphene. *Phys. Rev. Lett.*, 114:236801, Jun 2015.

[84] M. M. Jadidi, J. C. Konig-Otto, A. B. Sushkov, S. Winnerl, H. D. Drew, T. E. Murphy, and M. Mittendorff. Nonlinear Terahertz Absorption of Graphene Plasmons. *Nano Lett.*, 16(4), 2016.

[85] S. Winnerl, M. Orlita, P. Plochocka, P. Kossacki, M. Potemski, T. Winzer, E. Malic, A. Knorr, M. Sprinkle, C. Berger, W. A. de Heer, H. Schneider, and M. Helm. Carrier Relaxation in Epitaxial Graphene Photoexcited Near the Dirac Point. *Phys. Rev. Lett.*, 107:237401, Nov 2011.

[86] J. K. Viljas and T. T. Heikkilä. Electron-phonon heat transfer in monolayer and bilayer graphene. *Phys. Rev. B*, 81:245404, Jun 2010.

[87] S. Kar, D. R. Mohapatra, E. Freysz, and A. K. Sood. Tuning photoinduced terahertz conductivity in monolayer graphene: Optical-pump terahertz-probe spectroscopy. *Phys. Rev. B*, 90:165420, Oct 2014.

[88] A. J. Frenzel, C. H. Lui, Y. C. Shin, J. Kong, and N. Gedik. Semiconducting-to-Metallic Photoconductivity Crossover and Temperature-Dependent Drude Weight in Graphene. *Phys. Rev. Lett.*, 113:056602, Jul 2014.

[89] J.-H. Chen, C. Jang, S. Xiao, M. Ishigami, and M. S. Fuhrer. Intrinsic and extrinsic performance limits of graphene devices on SiO_2. *Nature Nanotech.*, 3:206–209, 2008.

[90] J. D. Cox and F. J. García de Abajo. Electrically tunable nonlinear plasmonics in graphene nanoislands. *Nat. Commun.*, 5, 2014.

[91] M. T. Manzoni, I. Silveiro, F. J. García de Abajo, and D. E. Chang. Second-order quantum nonlinear optical processes in single graphene nanostructures and arrays. *New J. Phys.*, 17, 2015.

[92] H. Wang, J. H. Strait, P. A. George, S. Shivaraman, V. B. Shields, M. Chandrashekhar, J. Hwang, F. Rana, Spencer M. G., C. S. Ruiz-Vargas, and J. Park. Ultrafast relaxation dynamics of hot optical phonons in graphene. *Appl. Phys. Lett.*, 105:081917, 2010.

[93] C. B. McKitterick, M. J. Rooks, and D. E. Prober. Electron-phonon cooling in large monolayer graphene devices. *Phys. Rev. B*, 93:075410, Feb 2016.

[94] L. Wang, I. Meric, P. Y. Huang, Q. Gao, Y. Gao, H. Tran, T. Taniguchi, K. Watanabe, L. M. Campos, D. A. Muller, J. Guo, P. Kim, J. Hone, K. L. Shepard, and C. R. Dean. One-Dimensional Electrical Contact to a Two-Dimensional Material. *Science*, 342(6158):614–617, 2013.

[95] M.W. Graham, S.F. Shi, Z. Wang, D.C. Ralph, J. Park, and P.L. McEuen. Transient absorption and photocurrent microscopy show that hot electron supercollisions describe the rate-limiting relaxation step in graphene. *Nano Lett.*, 13(11):5497–5502, 2013.

[96] K. J. Tielrooij, J. C. W. Song, S. A. Jensen, A. Centeno, A. Pesquera, A. Zurutuza Elorza, M. Bonn, L. S. Levitov, and F. H. L. Koppens. Photoexcitation cascade and multiple hot-carrier generation in graphene. *Nat. Phys.*, 9:248–252, 2013.

[97] M. M. Jadidi, R. J. Suess, C. Tan, X. Cai, K. Watanabe, T. Taniguchi, A. B. Sushkov, M. Mittendorff, J. Hone, H. D. Drew, M. S. Fuhrer, and T. E. Murphy. Infrared Nonlinear Photomixing Spectroscopy of Graphene Thermal Relaxation. *arXiv:1607.02181*, 2016.

[98] E.J. Lee, K. Balasubramanian, R.T. Weitz, M. Burghard, and K. Kern. Contact and edge effects in graphene devices. *Nat. Nanotechnol.*, 3(8):486–490, 2008.

[99] F. Xia, T. Mueller, R. Golizadeh-Mojarad, M. Freitag, Y.M. Lin, J. Tsang, V. Perebeinos, and P. Avouris. Photocurrent imaging and efficient photon detection in a graphene transistor. *Nano Lett.*, 9(3):1039–1044, 2009.

[100] C. R. Dean, A. F. Young, I. Meric, C. Lee, L. Wang, S. Sorgenfrei, K. Watanabe, T. Taniguchi, P. Kim, K. L. Shepard, and J. Hone. Boron nitride substrates for high-quality graphene electronics. *Nat. Nanotechnol.*, 5:722–726, 2010.

[101] T. Low, V. Perebeinos, R. Kim, M. Freitag, and P. Avouris. Cooling of photoexcited carriers in graphene by internal and substrate phonons. *Phys. Rev. B*, 86:045413, Jul 2012.

[102] E. H. Hwang and S. Das Sarma. Surface polar optical phonon interaction induced many-body effects and hot-electron relaxation in graphene. *Phys. Rev. B*, 87:115432, Mar 2013.

[103] M. Freitag, T. Low, and P. Avouris. Increased Responsivity of Suspended Graphene Photodetectors. *Nano Lett.*, 13(4):1644–1648, 2013. PMID: 23452264.

[104] J.C. Song, M.S. Rudner, C.M. Marcus, and L.S. Levitov. Hot carrier transport and photocurrent response in graphene. *Nano Lett.*, 11(11):4688–4692, 2011.

[105] E. H. Hwang, E. Rossi, and S. Das Sarma. Theory of thermopower in two-dimensional graphene. *Phys. Rev. B*, 80:235415, Dec 2009.

[106] T. J. Echtermeyer, P. S. Nene, M. Trushin, R. V. Gorbachev, A. L. Eiden, S. Milana, Z. Sun, J. Schliemann, E. Lidorikis, K. S. Novoselov, and A. C. Ferrari. Photothermoelectric and Photoelectric Contributions to Light Detection in MetalGrapheneMetal Photodetectors. *Nano Lett.*, 14(7):3733–3742, 2014.

[107] K.J. Tielrooij, M. Massicotte, L. Piatkowski, A. Woessner, Q. Ma, P. Jarillo-Herrero, N.F. van Hulst, and F.H.L. Koppens. Hot-carrier photocurrent effects at graphenemetal interfaces. . *J. Phys. Condens. Matter*, 27(16):164207, 2015.

[108] T. Mueller, F. Xia, M. Freitag, J. Tsang, and P. Avouris. Role of contacts in graphene transistors: A scanning photocurrent study. *Phys. Rev. B*, 79(24):245430, 2009.

[109] D. Sun, G. Aivazian, A.M. Jones, J.S. Ross, W. Yao, D. Cobden, and X. Xu. Ultrafast hot-carrier-dominated photocurrent in graphene. *Nat. Nanotechnol.*, 7(2):114–118, 2012.

[110] C. H. Lui, K. F. Mak, J. Shan, and T. F. Heinz. Ultrafast Photoluminescence from Graphene. *Phys. Rev. Lett.*, 105:127404, 2010.

[111] S-M Huang, S-Y Xu, I. Belopolski, C-C Lee, B. Wang G. Chang, N. Alidoust, G. Bian, M. Neupane, C. Zhang, S. Jia, A. Bansil, H. Lin, and M. Z. Hasan. A Weyl Fermion semimetal with surface Fermi arcs in the transition metal monopnictide TaAs class. *Nat. Commun.*, 6:7373, 2015.

[112] F. Arnold, M. Naumann, S.-C. Wu, Y. Sun, M. Schmidt, H. Borrmann, C. Felser, B. Yan, and E. Hassinger. Chiral Weyl Pockets and Fermi Surface Topology of the Weyl Semimetal TaAs. *Phys. Rev. Lett.*, 117(14):146401, 2016.

[113] C.-L. Zhang et al. Signatures of the AdlerBellJackiw chiral anomaly in a Weyl fermion semimetal. *Nat. Commun.*, 7:10375, 2016.

[114] M. Kargarian, M. Randeria, and N. Trivedi. Theory of Kerr and Faraday rotations and linear dichroism in Topological Weyl Semimetals. *Sci. Rep.*, 5:12683, 2015.

[115] S. Das Sarma, E. H. Hwang, and H. Min. Carrier screening, transport, and relaxation in three-dimensional Dirac semimetals. *Phys. Rev. B*, 91(11):035201, 2015.

[116] C. J. Tabert, J. P. Carbotte, and E. J. Nicol. Optical and transport properties in three-dimensional Dirac andWeyl semimetals. *Phys. Rev. B*, 93(18):085426, 2016.

[117] L. M. Malard, K. F. Mak, A. H. Castro Neto, N. M. R. Peres, and T. F. Heinz. Observation of intra- and inter-band transitions in the transient optical response of graphene. *New Journ. Phys.*, 15:015009, 2013.

[118] B. Xu, Y. M. Dai, L. X. Zhao, K. Wang, R. Yang, W. Zhang, J. Y. Liu, H. Xiao, G. F. Chen, A. J. Taylor, D. A. Yarotski, R. P. Prasankumar, and X. G. Qiu. Optical spectroscopy of the Weyl semimetal TaAs. *Phys. Rev. B*, 93(12):121110, 2016.

[119] A. B. Sushkov, J. B. Hofmann, G. S. Jenkins, J. Ishikawa, S. Nakatsuji, S. D. Sarma, and H. D. Drew. Optical evidence for a Weyl semimetal state in pyrochlore $Eu_2 Ir_2O_7$. *Phys. Rev. B*, 92(24):241108, 2015.

[120] G. S. Jenkins, C. Lane, B. Barbiellini, A. B. Sushkov, R. L. Carey, Fengguang Liu, J. W. Krizan, S. K. Kushwaha, Q. Gibson, Tay-Rong Chang, Horng-Tay Jeng, Hsin Lin, R. J. Cava, A. Bansil, and H. D. Drew. Three-dimensional Dirac cone carrier dynamics in Na_3Bi and Cd_3As_2. *Phys. Rev. B*, 94(8):085121, 2016.

[121] C-C Lee, S-Y Xu, S-M Huang, D. S. Sanchez I. Belopolski, G. Chang, G. Bian, H. Zheng N. Alidoust, M. Neupane, B. Wang, A. Bansil, M. Z. Hasan, and H. Lin. Fermi surface interconnectivity and topology in Weyl fermion semimetals TaAs, TaP, NbAs, and NbP. *Phys. Rev. B*, 92(10):235104, 2015.

[122] R. Lundgren and G. A. Fiete. Electronic cooling in Weyl and Dirac semimetals. *Phys. Rev. B*, 92:125139, 2015.

[123] A. C. Ferrari, J. C. Meyer, V. Scardaci, C. Casiraghi, M. Lazzeri, F. Mauri, S. Piscanec, D. Jiang, K. S. Novoselov, S. Roth, and A. K. Geim. Raman Spectrum of Graphene and Graphene Layers. *Phys. Rev. Lett.*, 97(18):187401, 2006.

[124] H. W. Liu, P. Richard, Z. D. Song, L. X. Zhao, Z. Fang, G.-F. Chen, and H. Ding. Raman study of lattice dynamics in Weyl semimetal TaAs. *Phys. Rev. B*, 92:064302, 2015.

[125] H. E. Elsayed-Ali, T. B. Norris, M. A. Pessot, and G. A. Mourou. Time-Resolved Observation of Electron-Phonon Relaxation in Copper. *Phys. Rev. Lett.*, 58(12), 1987.

[126] R.H.M. Groeneveld, R. Sprik, and A. Lagendijk. Femtosecond spectroscopy of electron-electron and electron-phonon energy relaxation in Ag and Au. *Phys. Rev. B*, 51(17):11433, 1995.

[127] Z. Lin and L. V. Zhiglei. Electron-phonon coupling and electron heat capacity of metals under conditions of strong electron-phonon nonequilibrium. *Phys. Rev. B*, 77(7):075133, 2008.

[128] D. Sun, Z.-K. Wu, C. Divin, X. Li, C. Berger, W. A. de Heer, P. N. First, and T. B. Norris. Ultrafast Relaxation of Excited Dirac Fermions in Epitaxial Graphene Using Optical Differential Transmission Spectroscopy. *Phys. Rev. Lett.*, 101(15):157402, 2008.

[129] D. Chang, Y. Liu, F. Rao, F. Wang, Q. Sunac, and Y. Jia. Phonon and thermal expansion properties in Weyl semimetals MX (M = Nb, Ta; X = P, As): ab initio studies. *Phys. Chem. Chem. Phys.*, 18:14503–14508, 2016.

[130] T. Ouyang, H. Xiao, C. Tang, M. Hu, and J. Zhonga. Anisotropic thermal transport in Weyl semimetal TaAs: a first principles calculation. *Phys. Chem. Chem. Phys.*, 18:16709–16714, 2015.

[131] T. Morimoto and N. Nagaosa. Topological nature of nonlinear optical effects in solids. *Sci. Adv.*, 2(5):1501524, 2016.

[132] S. Li, M.M. Jadidi, T.E. Murphy, and G. Kumar. Terahertz surface plasmon polaritons on a semiconductor surface structured with periodic V-grooves. *Opt. express*, 21(6):7041–7049, 2013.

[133] G. Kumar, S. Li, M.M. Jadidi, and T.E. Murphy. Terahertz surface plasmon waveguide based on a one-dimensional array of silicon pillars. *New J. Phys.*, 15(8):085031, 2013.